Advanced Control Strategies for Partially Levitating Multi-Sector Permanent Magnet Synchronous Machines

Zhuang Wen

Thesis submitted to the University of Nottingham
for the degree of Doctor of Philosophy

July 2022

Abstract

The thesis presents solutions to improve the performance of a partially levitating bearingless permanent magnet synchronous machine with a multi-three-phase winding. A combined winding topology, which consists of three independent three-phase sub-windings, is installed in the stator where each phase contributes to both the suspension force and the motoring torque. This work focuses on control algorithms, including fault-tolerant controls, a current limitation technique, and a current-sharing technique.

Firstly, the thesis presents an analytical formulation of the force and torque generation in healthy operative conditions. Following, the three-phase and single-phase open-circuit fault conditions are also analysed. The analytical model of the machine is presented in a generic matrix form so that it can be applied to any machine with a multi-three-phase winding structure if the coupling among sectors is negligible. The fault-tolerant control algorithms address the issues of open-circuit faults of an entire three-phase sub-winding, of a single-phase in a three-phase sub-winding, or of two phases belonging to two different three-phase sub-windings. The theoretical analysis is verified with both Finite Elements Analysis and experimental tests.

Then, the thesis proposes a current limitation technique. The main challenges with the combined winding configuration consist of decoupling the suspension force and torque generation and designing a proper current limitation technique. The latter is required in order to maintain the machine in safe

operative conditions according to its current-voltage rating and its operative thermal limits. This thesis addresses the limitation technique based on the analytical models, considering both healthy and faulty conditions. In particular, the proposed current limitation technique allows prioritising the suspension force, which is considered a safety-critical output with respect to the torque in order to avoid the rotor touchdown. Numerical simulation results and experimental validation are provided to validate the algorithm.

Finally, the thesis proposes a modular approach for a current-sharing control of the machine. A thorough explanation of the methodology used is presented, as well as control algorithms to consider the torque and force control combined with the current-sharing management of the machine. Particular emphasis is also placed on validating the modelling hypotheses based on a finite element characterisation of the machine electro-mechanical behaviour. The proposed control strategy is also extended to cater to the possibility of one or more inverters failure, thus validating the intrinsic advantage of the redundancy obtained by the system's modularity. An extensive experimental test is finally carried out on a prototyped machine. The obtained results validate the current-sharing operation in either healthy or faulty scenarios, both at steady-state and under transient conditions. These outcomes show the potential of the proposed strategy to increase the versatility of fault-tolerant drives applied to this machine topology.

Acknowledgements

Upon the completion of this thesis, I would like to thank my respectable supervisors for their patient and constructive instruction during my PhD studies. They are Giorgio Valente, Andrea Formentini, Luca Papini, and Pericle Zanchetta.

I must thank my colleagues, PhD students, and researchers at the University of Nottingham Power Electronics, Machine and Control Group. I had the best time with them there.

Last but not least, I would like to thank my parents. Their support and encouragement give me the confidence to explore my future.

The thesis was completed under the shadow of COVID-19. Although disasters never stop humans from exploring, humans are insignificant in the face of nature.

Abbreviations

AMB	Active Magnetic Bearing
MS	Multi Sector
BM	Bearingless Machine
PMSM	Permanent Magnet Synchronous Machine
PM	Permanent Magnet
FE	Finite Element
FEA	Finite Element Analysis
TPOC	Three-Phase Open-Circuit
SPOC	Single-Phase Open-Circuit
DSP	Digital Signal Process
THD	Total Harmonic Distortion
DQZ	Direct-Quadrature-Zero
DQ	Direct-Quadrature

Nomenclature

s	the s^{th} sector, $s \in [1, 2, 3]$
n_s	the quantity of sectors, $n_s = 3$ in the thesis
t	time
$\mathrm{u_s}$	phase u of the s^{th} sector
$\mathrm{v_s}$	phase v of the s^{th} sector
$\mathrm{w_s}$	phase w of the s^{th} sector
${}^1\gamma$	angular position of the 1^{st} sector, with respect to the x-axis (rad)
${}^2\gamma$	angular position of the 2^{nd} sector, with respect to the magnetic axis of the sector 1, $\frac{2\pi}{3}$ in the thesis (rad)
${}^3\gamma$	angular position of the 3^{rd} sector, with respect to the magnetic axis of the sector 1, $\frac{4\pi}{3}$ in the thesis (rad)
$\overline{v}_{\mathrm{uvw}}$	9-phase voltage vector in the uvw reference frame
$\overline{i}_{\mathrm{uvw}}$	9-phase current vector in the uvw reference frame
$\overline{\lambda}_{\mathrm{uvw}}$	9-phase flux linkage vector in the uvw reference frame
$\overline{\lambda}_i$	9-phase flux linkage vector contributed by phase currents
$\overline{\lambda}_{PM}$	9-phase flux linkage vector provided by permanent magnet
$\mathbf{R}$	9-phase resistance matrix
r_{ph}	phase resistance (Ohm)
$\varkappa$	phase $\varkappa$ or $\varkappa$-axis, $\varkappa \in [\mathrm{u, v, w}, \alpha, \beta, \mathrm{d, q}]$
${}^s v_\varkappa$	voltage of the s^{th} sector, phase $\varkappa$ or $\varkappa$ axis (V)
${}^s i_\varkappa$	current of the s^{th} sector, phase $\varkappa$ or $\varkappa$ axis (A)
${}^s \lambda_\varkappa$	flux linkage of the s^{th} sector, phase $\varkappa$ or $\varkappa$ axis (Wb)
${}^s e_\varkappa$	back-EMF of the s^{th} sector, phase $\varkappa$ or $\varkappa$ axis (V)
$\mathbf{L}_{\mathrm{ph}}$	9-phase inductance matrix
$\mathbf{L}$	3-phase inductance matrix
$\mathbf{M}$	matrix of mutual inductances between sectors

L_{uu}	self-inductance of phase u (H)
L_{vv}	self-inductance of phase v (H)
L_{ww}	self-inductance of phase w (H)
M_{vu}	mutual inductance between phase u and v in one sector (H)
M_{wu}	mutual inductance between phase u and w in one sector (H)
M_{uv}	mutual inductance between phase v and u in one sector (H)
M_{wv}	mutual inductance between phase v and w in one sector (H)
M_{uw}	mutual inductance between phase w and u in one sector (H)
M_{vw}	mutual inductance between phase w and v in one sector (H)
M_c	mutual inductance between phases of different sectors (H)
p	rotor pole pair, 3 in the thesis
ϑ_{m}	rotor mechanical angular position with respect to the winding magnetic axis (rad)
ϑ_{e}	rotor electrical angular position, $\vartheta_{\mathrm{e}} = p\vartheta_m$ (rad)
F_x	electromagnetic mechanical force acting the x-axis of the rotor (N)
F_y	electromagnetic mechanical force acting the y-axis of the rotor (N)
T	motoring torque (Nm)
$\bar{W}$	wrench vector consisting of the suspension forces F_x, F_y, and the torque T
${}^sF_x$	the s^{th} sector contributed electromagnetic mechanical force acting the x-axis of the rotor (N)
${}^sF_y$	the s^{th} sector contributed electromagnetic mechanical force acting the y-axis of the rotor (N)
${}^sT$	the s^{th} sector contributed motoring torque (Nm)
${}^s\bar{W}$	the s^{th} sector contributed wrench vector consisting of the suspension forces ${}^sF_x$, ${}^sF_y$, and the torque ${}^sT$
$\bar{i}_{\alpha\beta}$	$\alpha - \beta$ axis current vector of the entire MS PMSM

${}^{s}\bar{i}_{\alpha\beta}$	$\alpha - \beta$ axis current vector of the s^{th} sector.
${}^{s}\mathbf{K}_{\alpha\beta}(\vartheta_{\mathrm{e}})$	wrench-current coefficient matrix of the s^{th} sector, the corresponding current vector written in a stationary $\alpha\beta$ reference frame.
$\mathbf{K}_{\alpha\beta}(\vartheta_{\mathrm{e}})$	wrench-current coefficient matrix of the entire machine including three sectors for the prototype machine, the corresponding current vector written in the stationary $\alpha\beta$ reference frame, $\mathbf{K}_{\alpha\beta}(\vartheta_{\mathrm{e}}) = [{}^{1}\mathbf{K}_{\alpha\beta}(\vartheta_{\mathrm{e}}) \;\; {}^{2}\mathbf{K}_{\alpha\beta}(\vartheta_{\mathrm{e}}) \;\; {}^{3}\mathbf{K}_{\alpha\beta}(\vartheta_{\mathrm{e}})]$
${}^{s}k_{\#\varkappa}(\vartheta_{\mathrm{e}})$	element involved in ${}^{s}\mathbf{K}_{\alpha\beta}(\vartheta_{\mathrm{e}})$, $\mathbf{K}_{\alpha\beta}(\vartheta_{\mathrm{e}})$, ${}^{s}\mathbf{K}_{\mathrm{uvw}}(\vartheta_{\mathrm{e}})$, $\mathbf{K}_{\mathrm{uvw}}(\vartheta_{\mathrm{e}})$, ${}^{s}\mathbf{K}_{\mathrm{dq}}(\vartheta_{\mathrm{e}})$, or $\mathbf{K}_{\mathrm{dq}}(\vartheta_{\mathrm{e}})$, $_{\#} \in [x, y, T]$, $_{\varkappa} \in [\mathrm{u}, \mathrm{v}, \mathrm{w}, \alpha, \beta, \mathrm{d}, \mathrm{q}]$
${}^{s}k_{\#\varkappa,n^{th}}$	magnitude of the n^{th} order harmonic of ${}^{s}k_{\#\varkappa}(\vartheta_{\mathrm{e}})$
${}^{s}\varphi_{\#\varkappa,n^{th}}$	phase angle of the n^{th} order harmonic of ${}^{s}k_{\#\varkappa}(\vartheta_{\mathrm{e}})$.
$\mathbf{K}^{+}_{\alpha\beta}(\vartheta_{\mathrm{e}})$	pseudo inverse of the wrench-current coefficient matrix $\mathbf{K}_{\alpha\beta}(\vartheta_{\mathrm{e}})$.
${}^{s}k^{+}_{\#\varkappa}(\vartheta_{\mathrm{e}})$	element involved in $\mathbf{K}^{+}_{\alpha\beta}(\vartheta_{\mathrm{e}})$, $\mathbf{K}^{+}_{\mathrm{uvw}}(\vartheta_{\mathrm{e}})$, or $\mathbf{K}^{+}_{\mathrm{dq}}(\vartheta_{\mathrm{e}})$, depending on the reference frame, $_{\#} \in [x, y, T]$, $_{\varkappa} \in [\mathrm{u}, \mathrm{v}, \mathrm{w}, \alpha, \beta, \mathrm{d}, \mathrm{q}]$.
$\mathbf{K}_{\alpha\beta,\mathrm{fs}}(\vartheta_{\mathrm{e}})$	wrench-current coefficient matrix of three sectors, with a three-phase open-circuit fault occurred in the s^{th} sector, the corresponding current vector written in a stationary $\alpha\beta$ reference frame, $s \in [1, 2, 3]$
$\bar{i}_{\alpha\beta,\mathrm{fs}}$	current vector in the stationary $\alpha\beta$ reference frame, with a three-phase open-circuit fault occurred in the s^{th} sector, $s \in [1, 2, 3]$
$\mathbf{K}_{\mathrm{uvw}}(\vartheta_{\mathrm{e}})$	wrench-current coefficient matrix of the entire machine, the corresponding current vector written in the uvw reference frame
${}^{s}\mathbf{K}_{\mathrm{uvw}}(\vartheta_{\mathrm{e}})$	wrench coefficient matrix of the s^{th} sector, the corresponding current vector written in the uvw reference frame, ${}^{s}\mathbf{K}_{\mathrm{uvw}}(\vartheta_{\mathrm{e}}) \in \mathbf{K}_{\mathrm{uvw}}(\vartheta_{\mathrm{e}})$

$\mathbf{T}_{C9}$	nine-phase amplitude invariant Clarke transformation matrix
$\mathbf{T}_c$	three-phase Clarke transformation
${}^s\mathbf{K}_{\mathrm{uvw,f}\varkappa}(\vartheta_{\mathrm{e}})$	wrench-current coefficient matrix of the s^{th} sector, with a single-phase open-circuit fault occurred in the phase $\varkappa$, the corresponding current vector written in the uvw reference frame, $s \in [1,2,3], \varkappa \in [\mathrm{u},\mathrm{v},\mathrm{w}]$
$\mathbf{K}_{\mathrm{uvw,fs}\varkappa}(\vartheta_{\mathrm{e}})$	wrench-current coefficient matrix of three sectors, with a single-phase open-circuit fault occurred in the phase $\varkappa$ of the sector s, the corresponding current vector written in the uvw reference frame, $s \in [1,2,3], \varkappa \in [\mathrm{u},\mathrm{v},\mathrm{w}]$
$\mathbf{T}_{\mathrm{Pk}}(\vartheta_{\mathrm{e}})$	Park transformation matrix
$\mathbf{K}_{\mathrm{dq}}(\vartheta_{\mathrm{e}})$	wrench-current coefficient matrix of three sectors, the corresponding current vector written in the direct-quadrature coordinate in a rotor rotational reference frame
${}^s\mathbf{K}_{\mathrm{dq}}(\vartheta_{\mathrm{e}})$	wrench coefficient matrix of the s^{th} sector, the corresponding current vector written in the direct-quadrature coordinate in a rotor rotational reference frame, ${}^s\mathbf{K}_{\mathrm{dq}}(\vartheta_{\mathrm{e}}) \in \mathbf{K}_{\mathrm{dq}}(\vartheta_{\mathrm{e}})$
$\mathbf{K}^{+}_{\mathrm{dq}}(\vartheta_{\mathrm{e}})$	pseudo inverse of $\mathbf{K}_{\mathrm{dq}}(\vartheta_{\mathrm{e}})$
$\overline{v}_{\mathrm{dq}}$	$d-q$ axis voltage vector of the entire MS PMSM
$\overline{i}_{\mathrm{dq}}$	$d-q$ axis current vector of the entire MS PMSM
k_p	proportional gain
k_i	integral gain
k_d	differential gain
ω_{m}	Rotor rotary speed
p_x	rotor x-axis radial position
p_y	rotor y-axis radial position
$\hat{F}_x$	the maximum x-axis achievable force
$\hat{F}_y$	the maximum y-axis achievable force
${}^{+}\hat{T}_s$ and ${}^{-}\hat{T}_s$	the maximum achievable torque of the s^{th} sector

$\widetilde{F}_x$	the limited x-axis suspension force
$\widetilde{F}_y$	the limited y-axis suspension force
$\widetilde{T}_x$	the limited motoring torque
Z_{sh}	current-sharing coefficient matrix
z_{sh}	current-sharing coefficient
$F_{x,\mathrm{q}}$ and $F_{y,\mathrm{q}}$	suspension force generated by q-axis current
$\bar{F}_\mathrm{q}$	suspension force vector generated by q-axis current, $\bar{F}_\mathrm{q} = [F_{x,\mathrm{q}} \;\; F_{y,\mathrm{q}}]'$
$F_{x,\mathrm{d}}$ and $F_{y,\mathrm{d}}$	suspension force generated by d-axis current
$\bar{F}_\mathrm{d}$	suspension force vector generated by d-axis current, $\bar{F}_\mathrm{d} = [F_{x,\mathrm{d}} \;\; F_{y,\mathrm{d}}]'$
$\bar{F}$	suspension force provided by both d-q axis currents, $\bar{F} = \bar{F}_\mathrm{d} + \bar{F}_\mathrm{q}$
$\mathbf{K}_\mathrm{d}(\vartheta_\mathrm{e})$	odd columns and the first rows of $\mathbf{K}_\mathrm{dq}(\vartheta_\mathrm{e})$
$\mathbf{K}_\mathrm{q}(\vartheta_\mathrm{e})$	even columns and the first rows of $\mathbf{K}_\mathrm{dq}(\vartheta_\mathrm{e})$

Contents

List of Tables

List of Figures

Chapter 1

Introduction

This chapter provides the background and definitions of bearingless machines (BMs). Meanwhile, the objective and motivation of the thesis are also presented. A summary of each chapter is listed in the end.

1.1 A brief introduction and definitions of bearingless machines

AC drive systems have been applied worldwide since the 1970s due to their outstanding features over DC machines, such as compactness, lower cost, and higher performance [1]. Developments in power electronic devices help AC machines operate at higher electrical frequencies, so higher rotational speeds. The higher rotational speed leads to reduced lifetime of mechanical bearings [2]. Furthermore, the bearings require lubrication and renewal, a task which is very difficult to implement in outer space or extreme environments with radiation or poisonous substances. Meanwhile, lubrication oil is unsuitable in extreme temperatures and perfectly sterile environments such as food, artificial hearts, and pharmacy processes [1, 3–8]. Hence, active magnetic suspension bearings are developed to overcome the disadvantages of conventional mechanical bearings.

Figure 1.1 shows a schematic diagram of a machine equipped with radial and

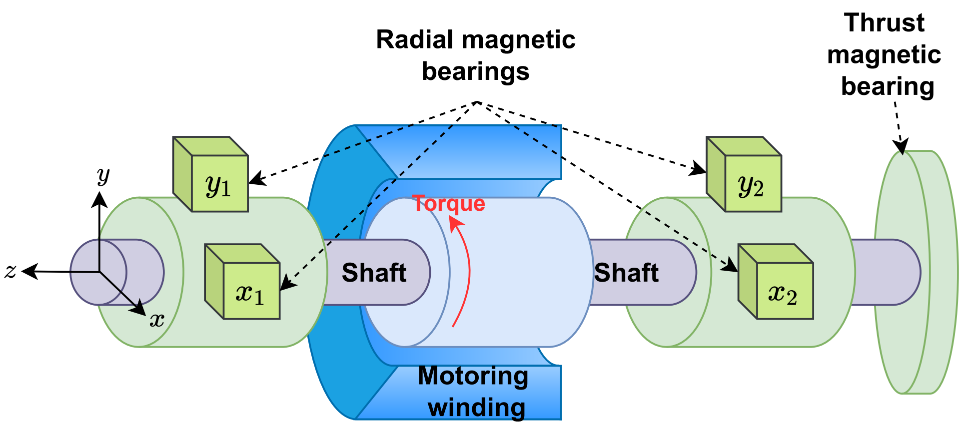

Figure 1.1: *Structure of the machine with radial and axial active magnetic bearings.*

axial active magnetic bearings (AMBs) [1]. The figure displays an example of the structure of AMBs, while the structure varies depending on the design and requirements. The motoring winding takes responsibility for the torque, while AMBs independently regulate radial and axial positions of the shaft on $x_1 - y_1$, $x_2 - y_2$, and z axes. In the figure, each radial AMB ($x_1 - y_1$ or $x_2 - y_2$) consists of four coils, with each axis (x_1, y_1, x_2 or y_2) equipped with two coils, one in the positive direction and the other in the negative direction. Each coil generates an attracting force, and the net force in the corresponding axis is the vector sum of the forces provided by two coils. The thrust AMB is composed of two coils. The contactless structure features reduced friction, reduced noise, and no mechanical losses. However, the overall length of machines with AMBs is longer than conventional machines. Hence, the concept of BMs is proposed to overcome the disadvantage that occurred in AMBs.

The concepts of BMs can be traced back to early 1970s [9]. However, an increased interest in the topic has started only from the 1990s [10, 11]. Till now, a lot of solutions have been proposed to realize the rotor levitation.

Figure 1.2 illustrates the structure of a BM. Bearingless units can generate suspension forces and torque simultaneously. Therefore, bearingless units allow the control of the shaft radial positions on $x_1 - y_1$ and $x_2 - y_2$ and provide the motoring torque. The rotor position in the z-axis is controlled by a thrust AMB. In some applications, one of the bearingless units can be replaced by an

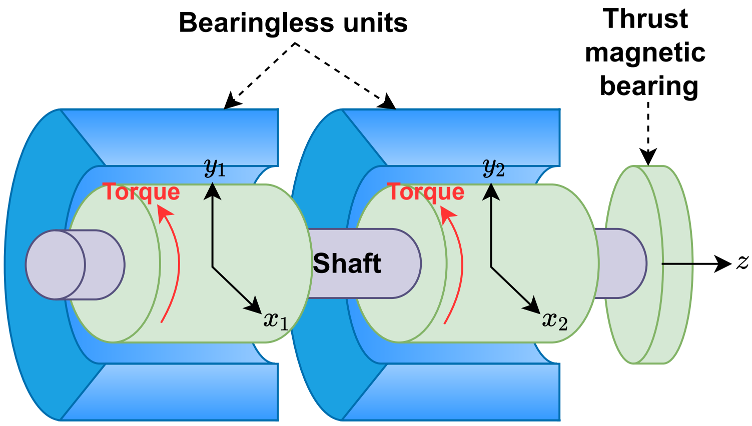

Figure 1.2: *Schematic diagram of BMs.*

AMB. It is possible to appreciate the definition of BMs from two perspectives [1]. The first describes the definition from an electrical machine perspective, a motor with a magnetically integrated bearing function. The second defines the principle from a mechanical prospective described as a magnetic bearing with a magnetically integrated motor function.

1.2 Objectives of the PhD project

The PhD project aims to explore the performance improvements of a bearingless multi-sector (MS) permanent magnet synchronous machine (PMSM), including three-phase open-circuit (TPOC) and single-phase open-circuit (SPOC) faults control (chapter 3), current limitation techniques (chapter 4), and control with faulty power sources (also known as current-sharing, chapter 5). In detail, the winding of the investigated BM consists of n_s sets of 3-phase windings (referred to as ”sector”). Each sector is supplied by a power electronic inverter, realizing the decoupled suspension force and torque control. The desired suspension force is the net vector sum of the suspension force vectors generated by all sectors. Since the principle of the healthy machine has been studied and presented in [12–15], the project will investigate the fault-tolerant control when a sector (a 3-phase sub-winding) open-circuit fault or a SPOC fault occurs in the BM. Moreover, the short-circuit fault-tolerant control approach will be investigated in future work. Another problem of the proposed BM is the current control algorithm cannot exploit the full power of the machine. Therefore, the project presents a current limitation technique to fulfil the potential power of the healthy and faulty machine. Furthermore, when faults occur in power electronic devices, an identical backup component may not be replaced on time. As a result, the machine has to be supplied by different power inverters or power sources with various power rating. Hence, it is necessary to develop a control algorithm applied under different power supplies, known as current-sharing techniques. In detail, the technique allows setting unequal q-axis current reference among sectors.

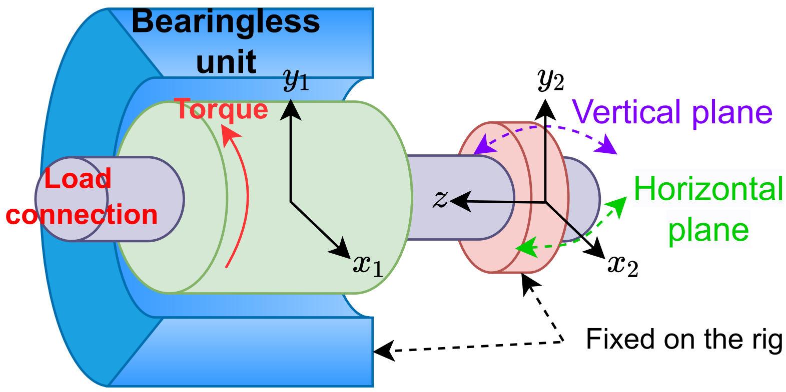

Figure 1.3: *The investigated BM in the PhD project.*

Figure 1.3 displays the investigated BM in the PhD project. The bearingless unit regulates the radial positions on the $x_1 - y_1$ axes. The other rotor side is suspended by a self-aligning ball bearing that allows rotor rotation on all axes but not translation in any directions. The displayed structure can verify the validity of the proposed principle that can generate the appropriate suspension force and torque. Once the algorithm is validated, with an AMB added, it is possible to extend the same methodologies to a fully levitating system.

The techniques have been studied and verified on a prototype machine within the Power Electronics, Machine & Control (PEMC) group at the University of Nottingham. This work focuses mainly on fault-tolerant control, current limitation techniques with healthy and faulty conditions, and current-sharing techniques. All proposed algorithms have been successfully tested on the experimental setup.

1.3 Motivation

The requirements of electrical machines vary depending on applications, but the general requirements are lower cost, lower acoustic noise, and lower maintenance [15–18]. The latter is strongly affected by mechanical bearings. Furthermore, in several industrial applications, especially chemical, pharmaceutical, and electronic components manufactures, the machines operate in perfectly sterile environments. Mechanical bearings, which often requires bearing lubricant to operate, would not be suitable as they contaminate the environment [3–7]. Bearingless machines, which can generate the suspension force and motoring torque in a single device [1, 19], would overcome the problems mentioned above thanks to their contact-free operations. They are also particularly suitable for high-speed drives such as compressors, flywheels, and spindles [20–25], where the mechanical bearing is often a limitation in terms of losses and potential failures. Although AMBs also feature suspension force control generation capability, BMs present an enhanced power density thanks to the integration of the levitating features in the power generation/motoring structure [1].
Several winding arrangements have been summarised and analysed in the literature review chapter. Chiba and Jia investigate BM solutions with two independent winding sets which separately produce suspension force and motoring torque [10, 25]. Two-winding solutions significantly reduce machines' power density, as typically $30 - 40\%$ of the slot area is filled with suspension winding conductors. However, the required suspension force is much smaller if the force disturbance is not significant during normal operations [1]. In other words, much less winding area is needed for suspension in normal conditions. In contrast, combined winding solutions, which consist of multiple phases (more than three), have the advantage of combining the force and the torque production

in a single winding set. Furthermore, multi-phase BMs possess a better fault-tolerant capability than standard three-phase ones [26]. In particular, modular multi-phase winding structures have more advantages, such as being easy to extend to larger machines with more modules. M. Ooshima presents the results of successful operations for a bearingless multi-phase machine with a multi-three-phase winding structure [27]. However, the suspension force and torque generation relies on the d$-$ and q$-$ axis currents of each sub-winding, respectively. The coupling effects of the force and torque production are neglected, leading to additional copper losses. Instead, the techniques implemented in [12–14, 28] includes the coupling effects, which leverages the pseudo-inverse matrix to compute the current reference values while minimizing the copper losses. Both solutions proposed in [29] and [12–14, 28] are developed to achieve fault-tolerant controls under a TPOC fault [29, 30]. However, they did not consider SPOC faults. When a SPOC fault occurs in a machine sector, the sector can still generate a suspension force. Compared to the solution of opening the circuit of the entire sector in order to reduce the undesired effects induced by the fault, SPOC fault operations can increase the machine's efficiency. Hence, it is necessary to explore the algorithm for the SPOC fault condition. Additionally, the control algorithms of healthy and faulty conditions are different. In general, control boards detect the fault within a period of time after a fault occurs. The control algorithm does not match the machine condition during the detection instant. In order to explore the effect caused by mismatched control algorithms, it is worth adding a fault detection method.

In a generic drive system, both machine and power electronic devices have an intrinsic current limit. If this limit is exceeded for an extended period, permanent damage can occur. A standard and simple method to avoid the problem is limiting the inverter current reference. The two-winding structure has different current ratings. Hence, it is straightforward to determine the maximum achievable force and torque once the current-to-force and current-to-torque relationships for the suspension force and torque windings, respectively, are known. However, in sectored multi-phase BMs, the relations among phase currents, torque, and forces are complex: saturating the phase currents could result in uncontrolled torque and forces, which, in turn, can lead to a rotor touchdown. An alternative approach is to limit force references and torque reference separately in order to fulfil the maximum current limit. This technique limits the system performance, as the maximum current capability is exploited only when rated torque and forces are simultaneously required. Furthermore, the machine can deliver the rated power in a healthy condition. In contrast, in the open-circuit faulty conditions, the system delivers reduced output power. Maximum torque and forces must be further reduced in faulty conditions, requiring a more advanced scheme to handle current saturation. Therefore, an appropriate current limitation technique is needed to guarantee the maximum output power (rated power in a healthy condition and reduced power under faulty conditions) of the machine.

An intrinsic feature of multi-three-phase machines is the possibility of independently managing the power flows among the different three-phase sub-windings, achieving the so-called current-sharing operation [31, 32]. The technique provides the possibility that three-phase sub-windings can be simultaneously supplied by diverse inverters, due to the structural layout of a drive that, for example, can present more independent power sources. Particularly, the current-sharing technique is important in applications requiring a high level of reliability [33]. Therefore, the project further explores current-sharing operations under healthy and faulty conditions.

1.4 Summary of each chapter

- Chapter 2 summarizes the literature on the topics of investigation during the PhD, such as structures of BMs, fault-tolerant control approaches, current-sharing techniques, analytical method of calculating the air-gap flux density, and fault detection techniques.

- Chapter 3 describes the structure and voltage equation of the machine studied in the project and presents fault-tolerant control algorithms of the proposed BM. The principle of the suspension force and torque generation in the healthy condition is introduced. Then, the fault-tolerant control algorithms, including the SPOC and TPOC faults conditions, are proposed. The Finite Element (FE) simulation and experiments verify the validity of the proposed approach. In the experimental section, the control strategy of the levitation system is described. The section also shows the experimental setup used to verify the algorithm, consisting of a BM, inverters, a load, a control board and proximity transducers. Finally, experimental results are presented and discussed.

- Chapter 4 explores the healthy and faulty operations with a current limitation algorithm which allows fully exploiting the machine capabilities. Firstly, the problem is explained, showing that the conventional methods cannot exploit the maximum capabilities of the proposed BM structure while ensuring the appropriate suspension force and the torque. Secondly, a current limitation technique that exploits the maximum power of the machine and prioritizes suspension force production at the expense of torque generation is detailed. Finally, the proposed method is compared with two conventional methods in Matlab Simulink environment and experimental tests. The results show how the proposed approach overcomes the disadvantages bought by conventional methods.

- Chapter 5 describes a current-sharing technique that allows active power flow among sectors. The current-sharing control approach is expressed at first. Then, the proposed algorithm is verified by FE simulation. Finally, the technique is validated in the experimental test.

- Chapter 6 summarizes the achievements of the PhD project and the future work.

Chapter 2

Literature Review

2.1 Introduction

In this chapter, a literature review regarding the studied subject is presented. At first, a brief introduction of bearingless machines' history is proposed. Then, several types of bearingless drives, fault-tolerant control methods, and current-sharing techniques are analysed. Next, the analytical method for calculating the air gap flux density and radial forces are indicated. Finally, the fault detection methods are explored.

2.2 Developments of bearingless machines

BMs' history can be traced back to the middle of the 1970s. P. K. Hermann proposed a primitive electromagnet with stator windings, embedding magnetic bearings in a motor [9, 34]. However, the lack of technologies about digital signal processors, inverters, and field-oriented control techniques limited the development of BMs [1]. In 1988, R. Bosch presented a disc type motor at an international conference in Pisa, Italy. The axial force of the machine was regulated by the exciting current [35]. According to [1], the first use of the word "Bearingless" is at that conference. In 1988, Chiba proposed a general concept of bearingless motors [36]. He found that most electrical motors can be turned into bearingless drives by applying an inverter fed suspension winding. M. A. Rahman provided strong support for the theoretical development of the bearingless concept [37]. Then, several types of machines have been developed for bearingless operations. Since the middle of the 1990s, bearingless motors have quickly developed in Switzerland, Austria, Germany, UK, France, Canada, USA, China, Korea, and other places. T. Higuchi and T. Fukao presented the switched reluctance bearingless motors in 1989 and 1997, respectively [38, 39]. N. Barletta from the Swiss Federal Institute of Technology in Zurich successfully developed a bearingless slice motor [40]. In 2002, a consequent-pole bearingless motor was designed by Chiba [41]. Due to the advantages of BMs in biomedical engineering, medical device manufacture, and semiconductor industries, BMs attract the attention of researchers from all over the world.

2.3 Bearingless machines and their structures

Several types of BMs have been developed, such as reluctance motors, induction motors, and PMSMs. These machines are composed of combined windings or separated windings. In a BM equipped with separated windings, the suspension force and torque are provided by suspension winding and motoring winding, respectively. On the other hand, combined windings generate suspension forces and torque with a single set of winding, for example, a single three-phase winding structure with a parallel path [11, 42–46], multiphase windings (more than three phases) [47–50], and multi-three-phase windings [12–15, 27, 51–53].

2.3.1 Bearingless switched reluctance motors

Chiba proposes a synchronous reluctance machine, and the principle of its suspension force production is illustrated in Figure 2.1 [10]. The rotor consists of four salient poles marked by the numbers 1, 2, 3, and 4 in the figure. The

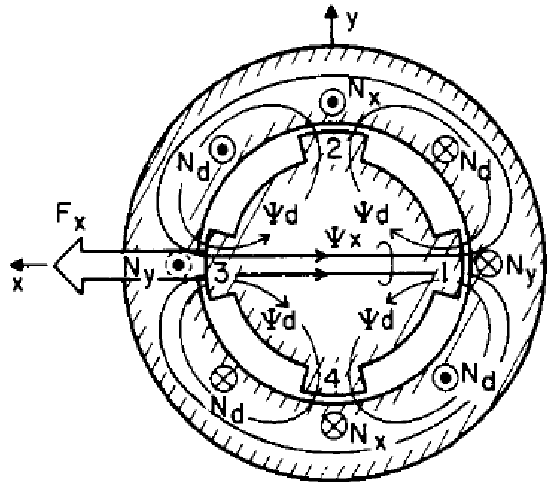

Figure 2.1: *The principle of the suspension force production [10].*

4-pole winding N_d stands for the equivalent windings in which the current represents the exciting current of the synchronous reluctance machine, while the 2-pole windings N_x and N_y stand for the transformed windings from stationary coordinates to the rotor rotational coordinate. By feeding a positive current in N_d winding, the flux Ψ_d is produced, as illustrated in Figure 2.1. If the currents in N_x and N_y are zero and the rotor is centred, the winding N_d produces balanced flux resulting in equal flux densities in 4 poles (1, 2, 3, and 4). When a positive current flows in N_x, the flux density in pole 1 will be decreased, while the flux density in pole 3 will be increased. A suspension force F_x is produced, as displayed in Figure 2.1. Since N_d, N_x, and N_y stand for equivalent windings synchronised with the rotor rotation, the machine can produce the desired suspension force at any rotor angular position. The transforms from stationary coordinates to rotor rotational reference frames (N_d, N_x, and N_y) are presented in detail in [10], and the transforms vary depending on the machine structure and control approach. The above shows a basic principle of the suspension force production, related with the unbalanced magnetic field produced by two sets of windings. Furthermore, [54–60] present several control strategies or winding structures of reluctance machines. Bearingless switched reluctance machines have the advantage of the manufacturing cost is lower than the permanent magnet machine because permanent magnet materials are not required. However, their noise and vibrations are higher than the PM machines.

2.3.2 Bearingless induction motors

Bearingless induction motors [61–63] feature a simple structure, high reliabilities and easy field weakness capabilities. The space vector control technique paves the way for developments of bearingless induction motors, allowing the machines to realize stable suspension under operating conditions which features external disturbance [62, 64]. The problem of understanding how the inaccuracy parameters caused by magnetic saturation influence the rotor levitation under overload conditions[65] has gained wide interest. Due to the lack of exciting windings, the magnetising current and the torque current are provided by a winding (can be called the torque winding). The torque and suspension force controls are coupled, resulting in a complex control strategy.

2.3.3 Bearingless permanent magnet synchronous machines

Bearingless PMSMs have advantages of high power density and efficiency. A six-phase bearingless PMSM with its fault-tolerant approach is presented in [50]. S. Kobayashi proposes a multiphase bearingless PMSM consisting of three sections [27], with its fault-tolerant control method developed in [29]. V. Giorgio proposes a sectored bearingless machine structure [12] similar to the one presented in [27], while the principle of the suspension force production is different. S. Kobayashi implements the suspension force and the torque by d-axis and q-axis currents, respectively [27]. The approach does not consider the coupling of the d-axis and q-axis current. Hence, compensation currents must be injected into the current reference to reduce the suspension force ripple. In contrast, V. Giorgio proposes a mathematical model that computes the current reference by sinusoidal functions of the electrical position [12]. The model is obtained by an analytical method and the results are verified by FEA. By applying the Moore–Penrose pseudo-inverse, the method minimizes the joule losses. In addition, V. Giorgio develops a suspension force and torque control approach which considers the rotor displacement [13]. The suspension force is applied to reduce the rotor vibrations or to realize rotor levitation [14, 15, 28]. Furthermore, the algorithm is extended to a single sector open-circuit fault operation [30].

2.4 Fault-tolerance control of bearingless machines

2.4.1 Fault-tolerant control in modular PMSMs

BMs equipped with multi-phase windings or multi-three-phase windings feature fault tolerance. A modular BM solution is proposed in [27], and then its fault-tolerant control approach under a section failure is developed in [29]. Figure 2.2 a) presents the cross-section of the modular permanent magnet synchronous bearingless machine proposed in [27, 29]. The winding consists of three three-phase windings, section-a, section-b, and section-c, fed by three inverters. The conventional $\mathrm{d} - \mathrm{q}$ axis current approach for the field-oriented control can be applied to this machine by applying standard three-phase inverters. Figure 2.2 b) indicates the suspension force generation principle, unbalanced flux density in the air gap. For example, if a suspension force along the $x-$axis is desired, section-a needs to implement field strengthening control, while section -b and -c must implement field-weakening control. The net force vector sum of three sections directs to the positive x-axis. Similarly, the suspension force can be generated to arbitrary radial direction by adjusting the electromagnetic forces provided by three sections.

The rotor radial position control approach presented in [27] decomposes the rotor radial position into a vector in two directions, represented by x and y

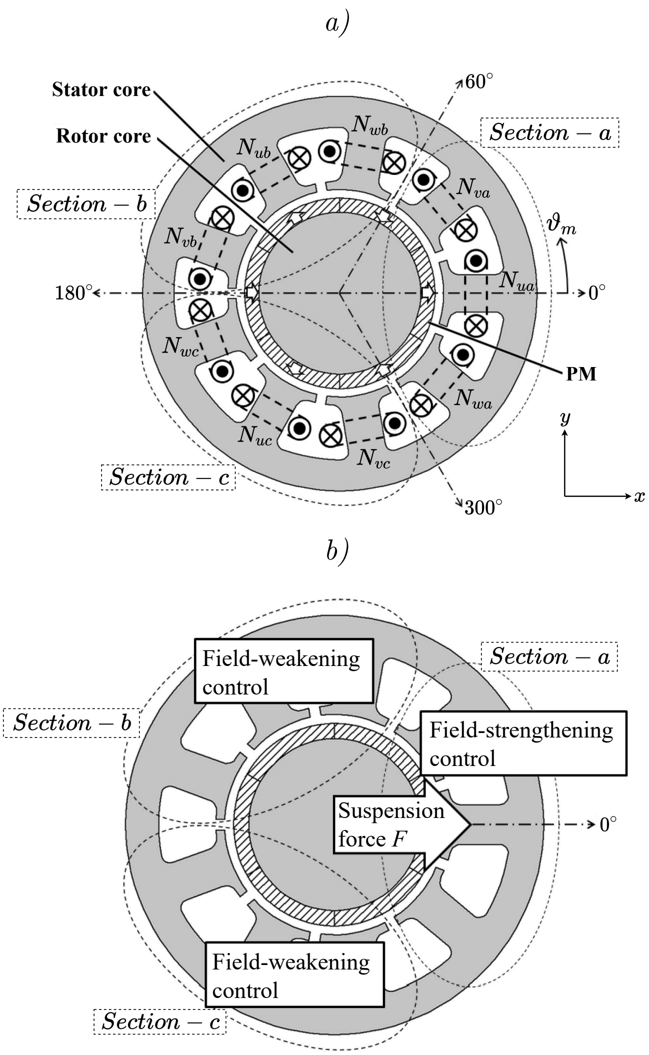

Figure 2.2: *a) Cross-section of the modular BM. b)Principle of the suspension force generation in a modular BM. [27]*

components in a stationary reference frame. Consequently, the suspension force is decomposed into a vector in two components, F_x and F_y, as shown in Figure 2.3. Since the suspension force F is the net force vector sum of electromagnetic forces provided by three sections, a coordinate transformation is needed to derive the relationship between the $x - y$ stationary coordinate and the *abc* stationary coordinate, shown in Figure 2.3 and expressed in (2.1).

$$\begin{bmatrix} F_a \\ F_b \\ F_c \end{bmatrix} = \frac{2}{3} \begin{bmatrix} 1 & 0 \\ -\frac{1}{2} & \frac{\sqrt{3}}{2} \\ -\frac{1}{2} & -\frac{\sqrt{3}}{2} \end{bmatrix} \begin{bmatrix} F_x \\ F_y \end{bmatrix} \tag{2.1}$$

F_a, F_b, and F_c represent the electromagnetic force generated by section-a,

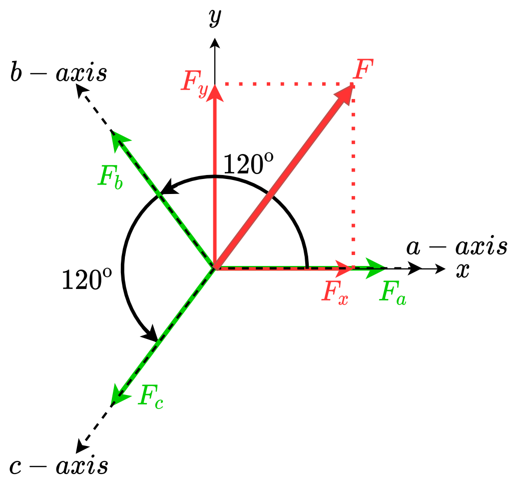

Figure 2.3: *a-, b-, c-, x-, and y- axis .*

-b, and -c, respectively, when the rotor angular position is 0. The $a-$axis corresponds to the $x-$axis. The directions of $b-$axis and $c-$axis are rotated by 120° and 240° in an anticlockwise direction, with respect to $a-$axis.

From the principle of suspension force generation as illustrated in Figure 2.2, the electromagnetic forces are generated along the $a-$, $b-$, and $c-$axes, respectively, when the rotor mechanical angular position ϑ_m is 0. In fact, Figure 2.3 displays such the scenario. According to [27], the magnitudes of forces are proportional to the stator d$-$axis currents in a linear region without magnetic saturation. Therefore, if sections are considered magnetically independent, it is reasonable to introduce the force coefficient k_n, expressed in (2.2)

$$
\begin{aligned}
F_{a(0)} &= k_n i_{\mathrm{da}} \\
F_{b(0)} &= k_n i_{\mathrm{db}} \\
F_{c(0)} &= k_n i_{\mathrm{dc}}
\end{aligned}
\tag{2.2}
$$

where i_{da}, $i_{\mathrm{d}b}$, and i_{dc} represent the stator d-axis currents transformed from three sections' three-phase currents by the standard Direct-Quadrature (DQ) transformation [66]. The d$-$axis current of each section is independently controlled and synchronised with rotor rotational reference frame. $F_{a(0)}$, $F_{b(0)}$, and $F_{c(0)}$ represent the electromagnetic forces generated by section $-a$, $-b$, and $-c$, respectively, when the rotor mechanical angular position is 0. k_n is constant in a linear region without magnetic saturation. Then, with the substitution of (2.2) into (2.1), the mathematical relationship between d−axis currents and the suspension force is obtained, expressed in (2.3).

$$\begin{bmatrix} i_{\mathrm{d}a} \\ i_{\mathrm{d}b} \\ i_{\mathrm{d}c} \end{bmatrix} = \frac{2}{3}\frac{1}{k_n} \begin{bmatrix} 1 & 0 \\ -\frac{1}{2} & \frac{\sqrt{3}}{2} \\ -\frac{1}{2} & -\frac{\sqrt{3}}{2} \end{bmatrix} \begin{bmatrix} F_x \\ F_y \end{bmatrix} \tag{2.3}$$

A FE simulation implemented in [27] validates that $i_{\mathrm{d}a}$, $i_{\mathrm{d}b}$, and $i_{\mathrm{d}c}$ obtained from (2.3) can generate the desired suspension force when the rotor angular position is 0. Meanwhile, the simulation verifies that the interactions among sections are negligible.

Then, let us analysis the the scenario when the rotor angular position is not 0. Directions of electromagnetic forces F_a, F_b, and F_c vary depending on the rotor angular position ϑ_m, as shown in Figure 2.4, and how the rotor angular position influences the directions of electromagnetic forces is presented in detail in [51]. At a varied rotor angular position, [27] applies the above

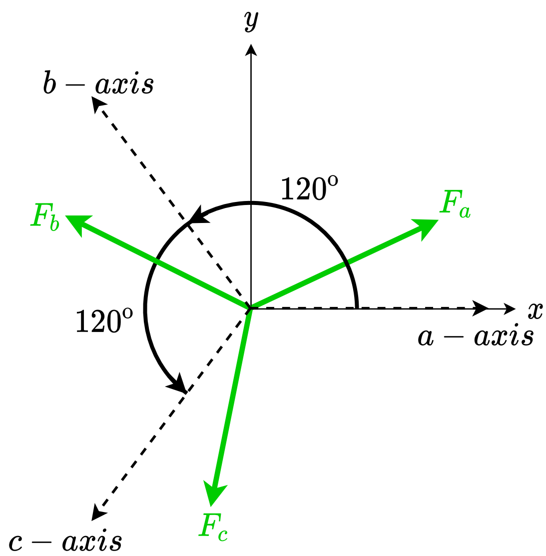

Figure 2.4: *a-, b-, c-, x-, and y- axis ($\vartheta_m \neq 0$).*

method (2.3) to calculate the current references with a constant force reference and implements a Finite Element verification by using the obtained currents. They find that the approach introduces a suspension force error between the force reference and the generated force, including the magnitude and direction errors. The magnitude error is due to the difference of the suspension winding Magnetomotive Force in each rotor angular position, and the direction error is caused by the variation of the d−axis in accordance with the rotor rotation[27]. Therefore, it is necessary to compensate for the force reference to obtain a desired suspension force.

When the rotor angular position is ϑ_m, the magnitude and direction of the net suspension force of three sections, obtained through FE simulation, are defined as $F_{(\vartheta_m)}$ and $\vartheta_{f(\vartheta_m)}$, respectively. In contrast, $F_{(0)}$ and $\vartheta_{f(0)}$ are the magnitude and direction of the net suspension force, respectively, when the rotor angular position is 0. The magnitude ratio of $F_{(0)}$ to $F_{(\vartheta_m)}$ is defined as compensation factor $k_{c(\vartheta_m)}$, expressed in (2.4).

$$k_{c(\vartheta_m)} = \frac{F_{(\vartheta_m)}}{F_{(0)}} \tag{2.4}$$

Additionally, the difference between $\vartheta_{f(0)}$ and $\vartheta_{f(\vartheta_m)}$ is defined as compensation angle $\vartheta_{c(\vartheta_m)}$, expressed as

$$\vartheta_{c(\vartheta_m)} = \vartheta_{f(\vartheta_m)} - \vartheta_{f(0)}. \tag{2.5}$$

Then, the compensated force reference $\bar{F}^*_{c(\vartheta_m)}$ is obtained, expressed in (2.6)

$$\begin{aligned} \bar{F}^*_{c(\vartheta_m)} &= \begin{bmatrix} F^*_{xc} \\ F^*_{yc} \end{bmatrix} \\ &= \frac{1}{k_{c(\vartheta_m)}} \boldsymbol{R}^{-1}_{(\vartheta_m)} \bar{F}^* = \frac{1}{k_{c(\vartheta_m)}} \begin{bmatrix} \cos \vartheta_{c(\vartheta_m)} & \sin \vartheta_{c(\vartheta_m)} \\ -\sin \vartheta_{c(\vartheta_m)} & \cos \vartheta_{c(\vartheta_m)} \end{bmatrix} \begin{bmatrix} F^*_x \\ F^*_y \end{bmatrix} \end{aligned} \tag{2.6}$$

where F^*_{xc} and F^*_{yc} are defined as the $x-$ and $y-$ axis components of the compensated force references, respectively. $k_{c(\vartheta_m)}$ and $\vartheta_{c(\vartheta_m)}$ are functions of the rotor angular position ϑ_m, and their waveforms can be found in [27]. $\boldsymbol{R}_{(\vartheta_m)}$

is a rotation matrix defined as

$$\boldsymbol{R}_{(\vartheta_m)} = \begin{bmatrix} \cos\vartheta_{c(\vartheta_m)} & -\sin\vartheta_{c(\vartheta_m)} \\ \sin\vartheta_{c(\vartheta_m)} & \cos\vartheta_{c(\vartheta_m)} \end{bmatrix}. \tag{2.7}$$

Figure 2.5 displays the compensation block diagram. F_x^* and F_y^* are the force references obtained from rotor radial position controllers. They are the actual forces that the machine requires to suspend the rotor. ${k_{c(\vartheta_m)}}^*$ and ${\vartheta_{c(\vartheta_m)}}^*$ are the input in accordance with rotor angular position. F_{xc}^* and F_{yc}^* are the compensation force references which are used to calculate the d−axis current references by (2.3).

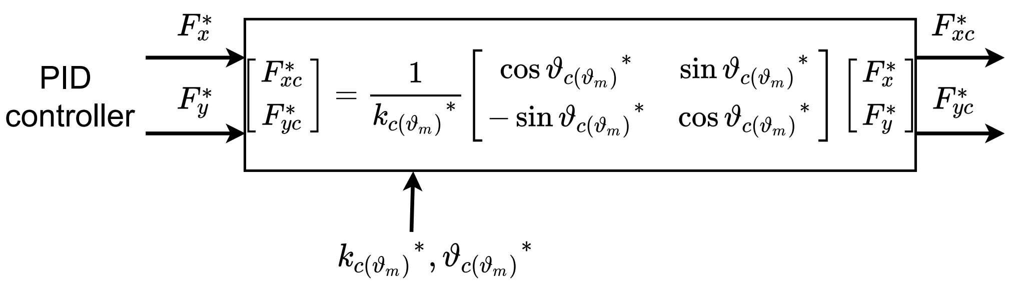

Figure 2.5: *Compensation block diagram [27].*

The approach presents the principle of the no-load condition. Furthermore, [51] develops the approach to stably operate the machine under a loaded condition. If the motoring torque is required, the magnetic field provided by the q−axis currents influences the generation of the suspension force, where q−axis currents are in the rotor rotation reference and transformed from the three-phase current by DQ transformation [66]. Therefore, the d−axis currents are used to compensate for the electromagnetic force generated by the q−axis currents, which causes additional copper losses.

Reference [29] realises the stabilised suspension control at the failure of a motor section. The coordinate transformation changes since only the remaining sections contribute to the suspension forces when a machine section is open-circuited. (2.8) and (2.9) present the new transformation when section-c is lost.

$$F_x = F_a + F_b \cos 120^\circ = F_a - \frac{1}{2} F_b \tag{2.8}$$

$$F_y = F_b \sin 120^\circ = \frac{\sqrt{3}}{2} F_b \tag{2.9}$$

Solving the equation (2.8) and (2.9) results in the expression of F_a and F_b.

$$F_a = F_x + \frac{\sqrt{3}}{3} F_y \tag{2.10}$$

$$F_b = \frac{2\sqrt{3}}{3} F_y \tag{2.11}$$

Then, the obtained force references F_a and F_b are applied to calculate the current references. Under the faulty conditions, the compensation method presented in (2.6) is still required.

The proposed algorithms decouple the d− and q− axis currents [27, 29, 51], not considering the minimum copper losses. A similar solution, considering the coupling between d− and q− axis currents, is presented in [12, 13, 28]. The articles propose a sectored BM equipped with three three-phase windings. A fault-tolerant control method of the proposed machine under one sector open-circuit fault is developed in [30].

Figure 2.6 displays the cross-section of the sectored machine proposed in [12, 13, 28, 30]. It is an 18-slot 6-pole surface-mounted PMSM. The red dashed lines divide the machine into three equal portions, respectively occupied by three-phase windings (named sector). Each three-phase winding is star-connected with a galvanically isolated neutral point and is supplied by a standard three-phase inverter. The suspension force is realised by controlling the currents of three sectors. A coefficient $\mathbf{K}_{\alpha\beta}(\vartheta_\mathrm{e})$ is applied to describe the relationships

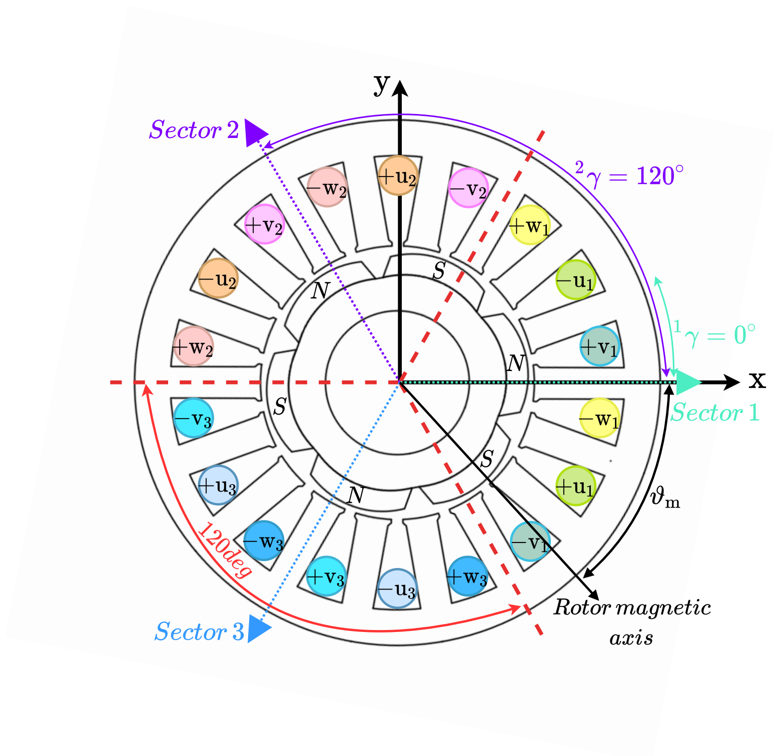

Figure 2.6: *Cross-section of the modular BM proposed in [12, 13, 28, 30]*

between the suspension force, torque and current, expressed in (2.12),

$$\begin{bmatrix} F_x \\ F_y \\ T \end{bmatrix} = \mathbf{K}_{\alpha\beta}(\vartheta_{\mathrm{e}})\bar{i}_{\alpha\beta} = \begin{bmatrix} {}^1\mathbf{K}_{\alpha\beta}\left(\vartheta_{\mathrm{e}}\right) & {}^2\mathbf{K}_{\alpha\beta}\left(\vartheta_{\mathrm{e}}\right) & {}^3\mathbf{K}_{\alpha\beta}\left(\vartheta_{\mathrm{e}}\right) \end{bmatrix} \begin{bmatrix} {}^1i_\alpha \\ {}^1i_\beta \\ {}^2i_\alpha \\ {}^2i_\beta \\ {}^3i_\alpha \\ {}^3i_\beta \end{bmatrix} \tag{2.12}$$

where F_x and F_y represent the suspension forces generated along $x-$ and $y-$axis, respectively, in a stationary $x-y$ coordinate. T stands for the motoring torque. $\bar{i}_{\alpha\beta}$ is a current vector containing three sectors' stator $\alpha-\beta$ axis currents transformed from three-phase currents by Clarke transformation. $\mathbf{K}_{\alpha\beta}(\vartheta_{\mathrm{e}})$ is composed of 3 sub-matrices ${}^s\mathbf{K}_{\alpha\beta}\left(\vartheta_{\mathrm{e}}\right)$ which describe the relation between $[F_x \;\; F_y \;\; T]'$ and the current of the s^{th} sector. The sub-matrix ${}^s\mathbf{K}_{\alpha\beta}(\vartheta_{\mathrm{e}})$

is a function of the rotor electrical position ϑ_e and is expressed in (2.13).

$$
{}^{s}\mathbf{K}_{\alpha\beta}(\vartheta_\mathrm{e}) = \begin{bmatrix} {}^{s}k_{x\alpha}(\vartheta_\mathrm{e}) & {}^{s}k_{x\beta}(\vartheta_\mathrm{e}) \\ {}^{s}k_{y\alpha}(\vartheta_\mathrm{e}) & {}^{s}k_{y\beta}(\vartheta_\mathrm{e}) \\ {}^{s}k_{T\alpha}(\vartheta_\mathrm{e}) & {}^{s}k_{T\beta}(\vartheta_\mathrm{e}) \end{bmatrix} \tag{2.13}
$$

The sub-matrix ${}^{1}\mathbf{K}_{\alpha\beta}(\vartheta_\mathrm{e})$ is obtained via the analytical method. Then, the analytical results are verified by FE simulations. The coefficient sub-matrices related to the generic s^{th} sector with $s \neq 1$ are obtained by a rotation matrix. The waveforms of the coefficients are presented in detail in [12].

In the bearingless control system, the suspension force references are generated by radial position controllers and are applied to compute the current reference. Therefore, the inverse of the coefficient matrix is required. However, the coefficient matrix, in general, is a rectangular matrix. Hence, the pseudo inverse, which guarantees the minimum copper losses, is applied to calculate the inverse of the coefficient matrix, expressed in (2.14) [12]

$$
\bar{i}^{*}_{\alpha\beta} = \mathbf{K}'_{\alpha\beta}(\vartheta_\mathrm{e})[\mathbf{K}_{\alpha\beta}(\vartheta_\mathrm{e})\mathbf{K}'_{\alpha\beta}(\vartheta_\mathrm{e})]^{-1} \begin{bmatrix} F^{*}_{x} \\ F^{*}_{y} \\ T^{*} \end{bmatrix} = \mathbf{K}^{+}_{\alpha\beta}(\vartheta_\mathrm{e}) \begin{bmatrix} F^{*}_{x} \\ F^{*}_{y} \\ T^{*} \end{bmatrix} \tag{2.14}
$$

where $\mathbf{K}^{+}_{\alpha\beta}(\vartheta_\mathrm{e})$ is the Moore-Penrose inverse of the matrix $\mathbf{K}_{\alpha\beta}(\vartheta_\mathrm{e})$.

When a three-phase sub-winding is in an open fault condition, for example, sector 1 open-circuit fault, the suspension forces and torque are provided by the remaining sectors, resulting in the following equation:

$$
\bar{i}^{*}_{\alpha\beta} = \begin{bmatrix} \mathbf{0}_{3\times 3} & {}^{2}\mathbf{K}_{\alpha\beta}(\vartheta_\mathrm{e}) & {}^{3}\mathbf{K}_{\alpha\beta}(\vartheta_\mathrm{e}) \end{bmatrix}^{+} \begin{bmatrix} F^{*}_{x} \\ F^{*}_{y} \\ T^{*} \end{bmatrix} \tag{2.15}
$$

It is noted that the sub-matrix ${}^{1}\mathbf{K}(\vartheta_\mathrm{e})$ is set to 0. Similarly, if the three-phase open-circuit fault is in the sector s, the corresponding sub-matrix ${}^{s}\mathbf{K}(\vartheta_\mathrm{e})$ will be set to 0.

2.5 Current-sharing techniques

The modular or sectored machines consist of n_s independent $m-$phase sub-windings supplied by n_s separate inverters. Therefore, the machines have an opportunity of connecting sub-windings to different inverters and power sources. The latter varies depending on the system configuration or budget. In fact, when $m = 3$, conventional three-phase converters can be employed to supply the multi three-phase windings [67]. An interesting feature of multi three-phase machines is the possibility of independently managing the power flows among the different three-phase sub-windings. This control possibility, also known as the current-sharing technique, is important in many highly redundancy-required applications and is analysed in recent researches [33, 53, 68, 69]. References [33, 68] present current-sharing techniques for induction machines, allowing setting unequal current reference among the converters. Reference [53] proposes a current-sharing technique for a multi-three-phase bearingless PMSM, realizing the power flowing among sectors. In [53], the proposed machine is composed of three three-phase windings supplied by three separate inverters that operate in different powers. For example, as shown in Figure 2.7, two sub-windings provide the torque, while the last one is a generator. The approach considers the machine as an entire system and

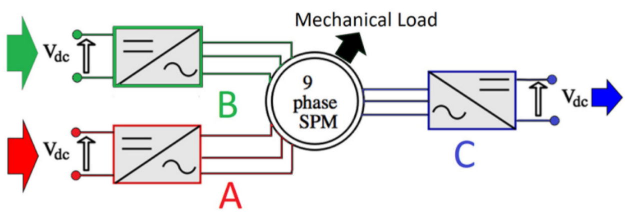

Figure 2.7: *Principle of the current-sharing technique [53].*

does not develop fault-tolerant control. However, the multi-sector machine has the potential of higher redundancy if compared to the conventional machines. Hence, it is worth developing a fault-tolerant control technique for the multi-three-phase bearingless machine.

2.6 Analytical method calculating the suspension force and torque

In the concept of BMs, the suspension force production is achieved by generating and controlling the amplitude and direction of unbalanced magnetic force. The latter can be predicted through the flux density that occurred in the air gap. The solution computing the air gap flux is needed to obtain an accurate mathematical model of the sectored machine. According to the Maxwell stress tensor, the radial τ and the tangential σ stresses in the air gap are derived in [70, 71] and expressed in (2.16)

$$\begin{aligned} \tau &= \frac{B_r^2 - B_t^2}{2\mu_0} \\ \sigma &= \frac{B_r B_t}{\mu_0} \end{aligned} \tag{2.16}$$

where B_r and B_t are the flux densities in the radial and the tangential directions, as shown in Figure 2.8, respectively. μ_0 is the vacuum permeability.

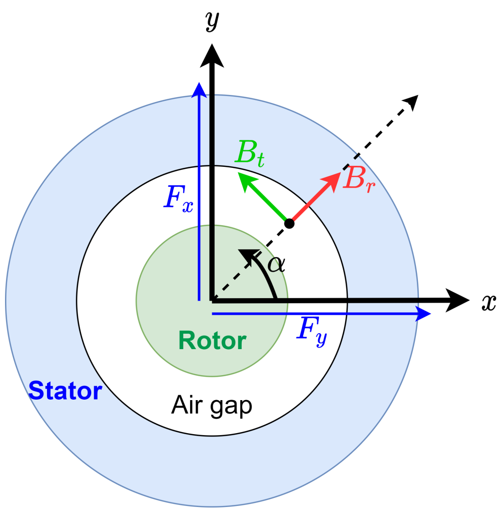

Figure 2.8: *The flux density of the air gap.*

The directions of τ and σ are along the directions of B_r and B_t, respectively. The electromagnetic forces along the x-axis (F_x) and the y-axis (F_y) can be separately calculated from the stresses.

$$F_{rx} = rl_a \int_0^{2\pi} \tau \cos(\alpha) d\alpha = \frac{rl_a}{2\mu_0} \int_0^{2\pi} (B_r^2 - B_t^2) \cos(\alpha) d\alpha \tag{2.17}$$

$$F_{ry} = rl_a \int_0^{2\pi} \tau \sin(\alpha) d\alpha = \frac{rl_a}{2\mu_0} \int_0^{2\pi} (B_r^2 - B_t^2) \sin(\alpha) d\alpha \tag{2.18}$$

$$F_{tx} = -rl_a \int_0^{2\pi} \sigma \sin(\alpha) d\alpha = -\frac{rl_a}{\mu_0} \int_0^{2\pi} (B_r B_t) \sin(\alpha) d\alpha \tag{2.19}$$

$$F_{ty} = rl_a \int_0^{2\pi} \sigma \cos(\alpha) d\alpha = \frac{rl_a}{\mu_0} \int_0^{2\pi} (B_r B_t) \cos(\alpha) d\alpha \tag{2.20}$$

$$F_x = F_{rx} + F_{tx} \tag{2.21}$$

$$F_y = F_{ry} + F_{ty} \tag{2.22}$$

In the above equations, r is the position where B_r and B_t are calculated and l_a is the active length. Finally, F_x and F_y are the electromagnetic forces acting on the rotor. For a PMSM, B_r and B_t account for both permanent magnet and armature contributions.

References [72, 73] present a method to compute the magnetic field distribution of permanent magnets under an assumption of the linear magnetic behaviour of the materials. In the air gap, the no-load magnetic field can be predicted by the following equations, (2.23) and (2.24).

$$B_{r,PM} = \sum_{n=1,3,5\cdots}^{\infty} K_B(n) \cdot f_{Br}(r) \cdot \cos(np\theta) \tag{2.23}$$

$$B_{t,PM} = \sum_{n=1,3,5\cdots}^{\infty} K_B(n) \cdot f_{Bt}(r) \cdot \sin(np\theta) \tag{2.24}$$

where p is the number of pole-pair while n means n^{th} harmonic order. θ stands for the mechanical angular position with respect to the axis of a pole, (i.e. the centre of a magnet), as shown in Figure 2.9. Then, when $np \neq 1$

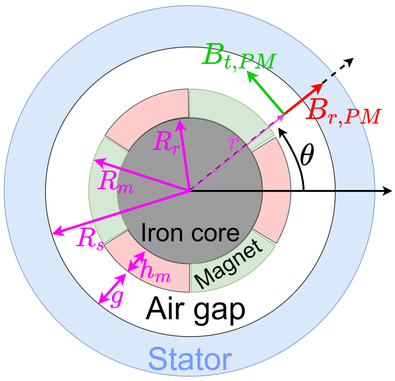

Figure 2.9: *$B_{r,PM}$ and $B_{t,PM}$ provided by the magnet.*

$$K_B(n) = \frac{\mu_0 M_n}{\mu_r} \cdot \frac{np}{(np)^2 - 1} \cdot \frac{(A_{3n} - 1) + 2\left(\frac{R_r}{R_m}\right)^{(np+1)} - (A_{3n} + 1)\left(\frac{R_r}{R_m}\right)^{2np}}{\frac{\mu_r+1}{\mu_r}\left[1 - \left(\frac{R_r}{R_s}\right)^{2np}\right] - \frac{\mu_r-1}{\mu_r}\left[\left(\frac{R_m}{R_s}\right)^{2np} - \left(\frac{R_r}{R_m}\right)^{2np}\right]} \tag{2.25}$$

$$f_{Br} = \left(\frac{r}{R_s}\right)^{(np-1)} \cdot \left(\frac{R_m}{R_s}\right)^{(np+1)} + \left(\frac{R_m}{r}\right)^{(np+1)} \tag{2.26}$$

$$f_{Bt} = -\left(\frac{r}{R_s}\right)^{(np-1)} \cdot \left(\frac{R_m}{R_s}\right)^{(np+1)} + \left(\frac{R_m}{r}\right)^{(np+1)} \tag{2.27}$$

where the dimensions R_s, R_m, and R_r, are illustrated in Figure 2.9, and μ_r is the relative recoil permeability. The air gap length is the actual length g in a slotted machine or the sum of both the air gap length g and the radial thickness of the windings in a slot-less stator. r is the radial position, the middle of the air gap where the flux densities are calculated. Additionally, in (2.25)-(2.27),

$$A_{3n} = np \tag{2.28}$$

$$M_n = M_{rn} + npM_{tn} \tag{2.29}$$

and

$$M_{rn} = 2\frac{B_{res}}{\mu_0}\alpha_p \frac{\sin\frac{n\pi\alpha_p}{2}}{\frac{n\pi\alpha_p}{2}} \tag{2.30}$$

$$M_{tn} = 0 \tag{2.31}$$

where B_{res} is the remanence, and α_p is the magnet pole-arc to pole-pitch ratio. The above analytical solution is only valid when the magnet is radially magnetised, as shown in Figure 2.10, while the calculation is different in the parallel magnetisation distribution magnet.

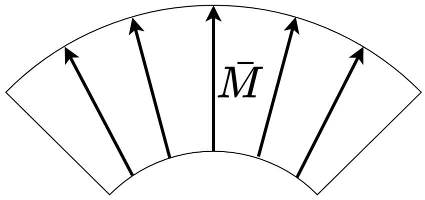

Figure 2.10: *The radial magnetisation distribution of the magnet.*

References [71, 74] present an approach that predicts the magnetic field produced by the winding currents. The method is only valid for a balanced three-phase symmetrical winding and in linear region of magnetic behaviour. The magnetic flux density can be decomposed into two components, the radial direction $B_{r,winding}$ and the tangential direction $B_{t,winding}$, and expressed in (2.32) and (2.33),

$$B_{r,winding}(\alpha, r, n) = \mu_0 \frac{2W}{\pi\delta} \sum_{n=1,2,3,...} \frac{1}{n} \cdot K_{son} \cdot K_{pn} \cdot F_{rn}(r) \cdot \left[i_{\mathrm{u}} \cdot \cos\left[n\left(\alpha\right)\right] + i_{\mathrm{v}} \cdot \cos\left[n\left(\alpha - \varphi\right)\right] + i_{\mathrm{w}} \cdot \cos\left[n\left(\alpha + \varphi\right)\right] \right] \tag{2.32}$$

$$B_{t,winding}(\alpha, r, n) = \mu_0 \frac{2W}{\pi\delta} \sum_{n=1,2,3,...} \frac{1}{n} \cdot K_{son} \cdot K_{pn} \cdot F_{tn}(r) \cdot \left[i_{\mathrm{u}} \cdot \sin\left[n\left(\alpha\right)\right] + i_{\mathrm{v}} \cdot \sin\left[n\left(\alpha - \varphi\right)\right] + i_{\mathrm{w}} \cdot \sin\left[n\left(\alpha + \varphi\right)\right] \right] \tag{2.33}$$

where W is the number of coil turns while α is the angular position with respect to the axis of a phase (i.e., the centre of the phase coil). $\delta = g + h_m$, is the effective air gap length. i_{u}, i_{v} and i_{w} are phase currents. φ is the mechanical angular position of the phase axis with respect to the axis of phase u. For example, Figure 2.11 shows the mechanical angle φ between phase u and phase v. K_{son} is the slot opening factor, expressed in (2.34),

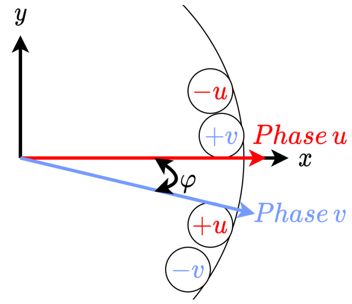

Figure 2.11: *Mechanical angular position φ between phase u and phase v.*

$$K_{son} = \frac{\sin n\frac{b_0}{2R_s}}{n\frac{b_0}{2R_s}} \tag{2.34}$$

where b_0 is the slot opening. If $b_0 \to 0$, the slot opening factor K_{son} reaches 1. The winding pitch factor is given by (2.35)

$$K_{pn} = \sin n\frac{\alpha_y}{2} \tag{2.35}$$

where α_p is the winding pitch, coil span. $F_{rn}(r)$ and $F_{tn}(r)$ are functions of the radial position r and harmonic order n, expressed in (2.36) and (2.37), respectively.

$$F_{rn}(r) = \delta\frac{n}{r}\left(\frac{r}{R_s}\right)^n \frac{1+\left(\frac{R_r}{r}\right)^{2n}}{1-\left(\frac{R_r}{R_s}\right)^{2n}} \tag{2.36}$$

$$F_{tn}(r) = \delta\frac{n}{r}\left(\frac{r}{R_s}\right)^n \frac{1-\left(\frac{R_r}{r}\right)^{2n}}{1-\left(\frac{R_r}{R_s}\right)^{2n}} \tag{2.37}$$

2.7 Fault detection techniques

In the above section, the structure of the magnetic field under healthy operating conditions is presented. However, when open-circuit faults occur in the winding structure, it needs to be detected in order to arrange an ad-hoc control strategy which enables the generation of the field distribution that allows the machine to maintain safe operating conditions. Several fault-tolerant control strategies of BMs have been introduced in the literature. In general, the control approaches for the healthy and faulty modes are different. The system first detects a fault and then switches to the faulty operating mode. There is a time gap before the controller switches to the faulty mode. The control method and the machine condition are not consistent during the time gap, which may cause undesired behaviours. Therefore, a fault detection technique is required to replicate the real control scenarios, though the project focuses on the control method under faulty operations rather than the fault detection. Reference [75] proposes a fault detection technique based on the $\mathrm{d-q}$ machine model in the rotor reference frame (without zero sequence components).

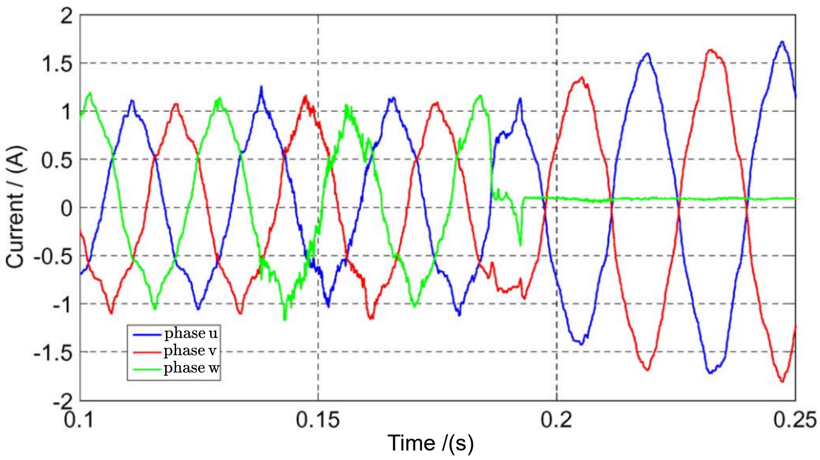

Figure 2.12: *PMSM stator three-phase currents during a single-phase open-circuit fault (experimental) [75].*

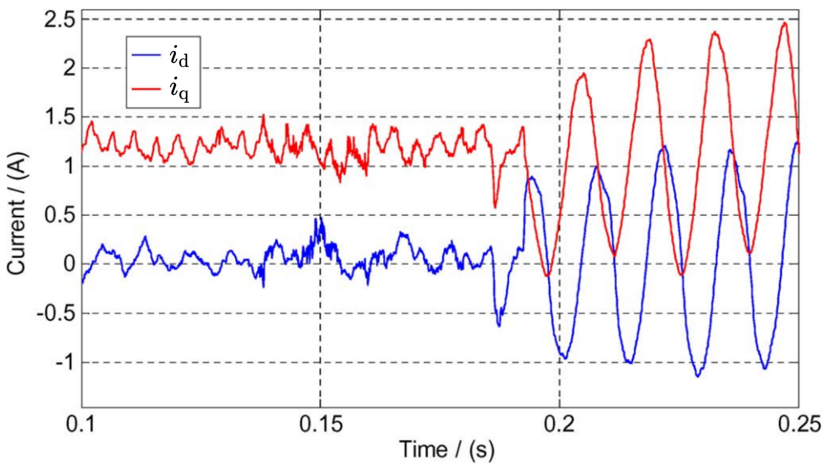

Figure 2.13: *i_{d} and i_{q} behaviour during and after a single-phase open-circuit fault (experimental) [75].*

Figure 2.12 and Figure 2.13 separately display the phase currents and the $\mathrm{d-q}$ axis currents of a PMSM equipped with an isolated neutral point during and after the fault. In healthy conditions, the quadrature and the direct axis currents are expressed in (2.38) and (2.39), respectively.

$$i_{\mathrm{q}} = \frac{2}{3}\left[\cos\left(\vartheta_{\mathrm{e}}\right) i_{\mathrm{u}} + \cos\left(\vartheta_{\mathrm{e}} - \frac{2\pi}{3}\right) i_{\mathrm{v}} + \cos\left(\vartheta_{\mathrm{e}} - \frac{4\pi}{3}\right) i_{\mathrm{w}}\right] \tag{2.38}$$

$$i_{\mathrm{d}} = \frac{2}{3}\left[\sin\left(\vartheta_{\mathrm{e}}\right) i_{\mathrm{u}} + \sin\left(\vartheta_{\mathrm{e}} - \frac{2\pi}{3}\right) i_{\mathrm{v}} + \sin\left(\vartheta_{\mathrm{e}} - \frac{4\pi}{3}\right) i_{\mathrm{w}}\right] \tag{2.39}$$

i_{u}, i_{v}, and i_{w} are the stator three-phase currents, and ϑ_{e} is the electrical position. In a single-phase open-circuit fault condition, i.e., phase w fault, the values of three-phase currents become $i_{\mathrm{w}} = 0$ and $i_{\mathrm{u}} = -i_{\mathrm{v}}$, as shown in Figure 2.12. Consequently, the d − q axis currents in the faulty mode are updated, expressed in (2.40) and (2.41).

$$\begin{aligned} i_{\mathrm{q}} &= \frac{2}{3}\left[\cos\left(\vartheta_{\mathrm{e}}\right) i_{\mathrm{u}} - \cos\left(\vartheta_{\mathrm{e}} - \frac{2\pi}{3}\right) i_{\mathrm{u}}\right] \\ &= \frac{-2}{\sqrt{3}}\left[i_{\mathrm{u}} \sin\left(\vartheta_{\mathrm{e}} - \frac{\pi}{3}\right)\right] \end{aligned} \tag{2.40}$$

$$\begin{aligned} i_{\mathrm{d}} &= \frac{2}{3}\left[\sin\left(\vartheta_{\mathrm{e}}\right) i_{\mathrm{u}} - \sin\left(\vartheta_{\mathrm{e}} - \frac{2\pi}{3}\right) i_{\mathrm{u}}\right] \\ &= \frac{2}{\sqrt{3}}\left[i_{\mathrm{u}} \cos\left(\vartheta_{\mathrm{e}} - \frac{\pi}{3}\right)\right] \end{aligned} \tag{2.41}$$

The ratio of faulty d − q currents $\left(\frac{i_{\mathrm{q}}}{i_{\mathrm{d}}}\right)$ can be expressed in (2.42), (2.43) and (2.44) for an open fault in phase u, v, and w, respectively.

$$\frac{i_{\mathrm{q}}}{i_{\mathrm{d}}} = -\tan\left(\vartheta_{\mathrm{e}} - \frac{3\pi}{3}\right) = -\tan\left(\vartheta_{\mathrm{e}} - \pi\right) \tag{2.42}$$

$$\frac{i_{\mathrm{q}}}{i_{\mathrm{d}}} = -\tan\left(\vartheta_{\mathrm{e}} - \frac{2\pi}{3}\right) \tag{2.43}$$

$$\frac{i_{\mathrm{q}}}{i_{\mathrm{d}}} = -\tan\left(\vartheta_{\mathrm{e}} - \frac{\pi}{3}\right) \tag{2.44}$$

The difference between the actual rotor electrical position ϑ_{e} measured from the resolver and the quantity $\tan^{-1}\left(-i_{\mathrm{q}}(t)/i_{\mathrm{q}}(t)\right)$ identifies the faulty phase, expressed in (2.45)

$$\angle S_1 = \angle(\vartheta_{\mathrm{e}}(t)) - \angle\left(\tan^{-1}\left(\frac{-i_{\mathrm{q}}(t)}{i_{\mathrm{d}}(t)}\right)\right) \tag{2.45}$$

where S_1 can be π, $\frac{2\pi}{3}$, or $\frac{\pi}{3}$ for the fault in phase u, v, or w, respectively, and t stands for time. The experimental test presented in [75] shows that the detection time varies depending on the rotation speed, $500\mu s$ to $103ms$ (750 to 150 r/min, respectively). A long detection time may lead to the rotor touchdown in a BM control system.

Some single-phase fault detection techniques are also analysed, but they have problems of algorithm complexity [76–80], of delays due to RMS calculation [81–83], of a long detection time [78–81]. Since the project mainly focuses on fault-tolerant control rather than fault detection, the project will implement a simple fault detection method to promptly and accurately switch the system from healthy mode to three-phase or single-phase faulty modes.

2.8 Summary of the Chapter

The chapter firstly introduces the history of bearingless machines. Then, several types of BMs and fault-tolerant control of modular BMs are analysed. Finally, techniques required for developing the project are explored.

Chapter 3

Fault-Tolerant Active Suspension Force Control in Multi-sector Permanent Magnet Synchronous Machines

3.1 Introduction

The proposed multi-sector BM consists of a multi-three-phase winding. Its structure is firstly introduced in section 3.2.1, and its voltage equation, which is different from the conventional three-phase machines due to the winding arrangement, is presented in section 3.2.2. Then, the MS BM is modelled assuming the healthy, TPOC, and SPOC faulty conditions. The healthy operating condition has been investigated and validated in [15, 84]. Hence, the TPOC and SPOC faults are the main focuses of the section. In section 3.3.1, the machine's electro-magneto-mechanical model (the relationships between the suspension force, torque, and phase currents) is built through the FEA analysis. Then, the model is developed for TPOC and SPOC conditions in section 3.4. The proposed approach leads to a generic matrix formulation of the machine models that can be applied to any machine with a multi-sector winding structure if the coupling between sectors is negligible. Finally, control strategies are verified by FEA in section 3.5, and they are experimentally validated on a prototype bearingless MS PMSM in section 3.6.

3.2 Structure of the bearingless machine and voltage equation

3.2.1 The machine structure

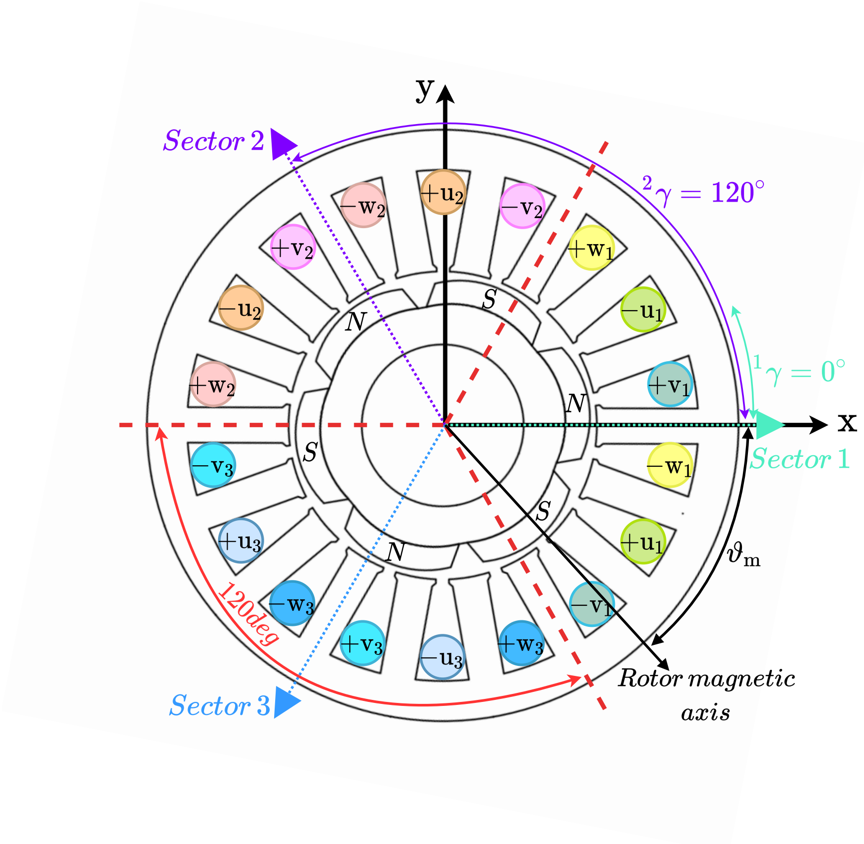

Figure 3.1: *Cross-section of the MS PMSM*

An 18-slot 6-pole surface-mounted PMSM that is available within the facilities of the Power Electronic Machine and Control (PEMC) Group of the University of Nottingham is adopted as a prototype machine. The original three-phase winding is replaced with three three-phase windings, as depicted in Figure 3.1. The red dashed lines divide the machine into three equal portions, respectively occupied by three-phase windings (named sector). Each three-phase winding is star-connected with a galvanically isolated neutral point. $\pm\mathrm{u_s}$, $\pm\mathrm{v_s}$, and $\pm\mathrm{w_s}$, indicate the phase and current direction of the machine. The symbol $+$ and $-$ mean the current direction is flowing out and into the cross-section plane, respectively. The subscript $s \in [1\,,2\,,3]$, located at the bottom right corner of each phase, is adopted to define the numerical order of the sector. For example, $+\mathrm{u_1}$ means the current direction of sector 1 phase u is flowing out the cross-section plane. ${}^s\gamma$ represents the angular position of the s^{th} sector with respect to the x-axis, ${}^1\gamma = 0\,deg$ and ${}^2\gamma = 120\,deg$ on the figure. ϑ_m is defined as the rotor angular position with respect to the winding magnetic axis, while the electrical position is $\vartheta_\mathrm{e} = p\vartheta_\mathrm{m}$, where p is the pole pair of the machine. Finally, the main parameters of the machine are listed in Table 3.1.

Table 3.1: MS PMSM Parameters

Parameter	**Value**
Pole number ($2p$)	6
PM material	NdFeB
PM remanence flux density B_{res}	1.24T
PM relative permeability μ_r	1.031
Power rating	1.5kW
Rated speed (n_{rated})	3000r/min
Rated torque	5N·m
Rated current (peak value)	13A
Turn/coil	22
PM flux of one sector (${}^s\Lambda_{PM}$)	0.0284Wb
Torque constant (k_T)	0.128N·m/A
Line to line voltage constant (k_V)	15.5V/krpm
Outer stator diameter	95mm
Inner stator diameter	49.5mm
Axial length	90mm
Airgap length	1mm
Magnets thickness	4mm

3.2.2 State representation of the voltage equation

The voltage equation presented in this section is under assumptions of the linear magnetic behaviour of the materials and centred rotor, which will be validated in section 3.3.1 and 3.5. The equation is expressed in a nine-phase form, as shown in (3.1):

$$\bar{v}_{\mathrm{uvw}} = \mathbf{R}\bar{i}_{\mathrm{uvw}} + \frac{\partial \bar{\lambda}_{\mathrm{uvw}}}{\partial t} \tag{3.1}$$

where

$$\begin{aligned}
\bar{v}_{\mathrm{uvw}} &= \begin{bmatrix} {}^{1}v_{\mathrm{u}} & {}^{1}v_{\mathrm{v}} & {}^{1}v_{\mathrm{w}} & {}^{2}v_{\mathrm{u}} & {}^{2}v_{\mathrm{v}} & {}^{2}v_{\mathrm{w}} & {}^{3}v_{\mathrm{u}} & {}^{3}v_{\mathrm{v}} & {}^{3}v_{\mathrm{w}} \end{bmatrix}' \\
\bar{i}_{\mathrm{uvw}} &= \begin{bmatrix} {}^{1}i_{\mathrm{u}} & {}^{1}i_{\mathrm{v}} & {}^{1}i_{\mathrm{w}} & {}^{2}i_{\mathrm{u}} & {}^{2}i_{\mathrm{v}} & {}^{2}i_{\mathrm{w}} & {}^{3}i_{\mathrm{u}} & {}^{3}i_{\mathrm{v}} & {}^{3}i_{\mathrm{w}} \end{bmatrix}' \\
\bar{\lambda}_{\mathrm{uvw}} &= \bar{\lambda}_{i} + \bar{\lambda}_{PM} = \begin{bmatrix} {}^{1}\lambda_{\mathrm{u}} & {}^{1}\lambda_{\mathrm{v}} & {}^{1}\lambda_{\mathrm{w}} & {}^{2}\lambda_{\mathrm{u}} & {}^{2}\lambda_{\mathrm{v}} & {}^{2}\lambda_{\mathrm{w}} & {}^{3}\lambda_{\mathrm{u}} & {}^{3}\lambda_{\mathrm{v}} & {}^{3}\lambda_{\mathrm{w}} \end{bmatrix}' \\
\mathbf{R} &= r_{\mathrm{ph}}\mathbf{I}.
\end{aligned} \tag{3.2}$$

The subscript $'$ is the transpose operator. r_{ph} stands for the phase resistance, and $\mathbf{I}$ is a 9×9 identity matrix. $\bar{v}_{\mathrm{uvw}}$, $\bar{i}_{\mathrm{uvw}}$, and $\bar{\lambda}_{\mathrm{uvw}}$ represent the nine-phase voltage vector, the nine-phase current vector, and the flux linkage of the machine, respectively. $\bar{\lambda}_{\mathrm{uvw}}$ consists of two components: phase currents contributed $\bar{\lambda}_{i}$ and permanent magnets provided $\bar{\lambda}_{PM}$. The phase inductance matrix is defined as $\mathbf{L}_{\mathrm{ph}}$, and (3.1) then can be expressed in the following equation:

$$\bar{v}_{\mathrm{uvw}} = \mathbf{R}\bar{i}_{\mathrm{uvw}} + \frac{\partial \bar{\lambda}_{i}}{\partial t} + \frac{\partial \bar{\lambda}_{PM}}{\partial t} = \mathbf{R}\bar{i}_{\mathrm{uvw}} + \mathbf{L}_{\mathrm{ph}}\frac{\partial \bar{i}_{\mathrm{uvw}}}{\partial t} + \bar{e} \tag{3.3}$$

where $\bar{e}$ is the vector of nine back-EMFs of the machine, expressed in the following equation :

$$\bar{e} = \frac{\partial \bar{\lambda}_{PM}}{\partial t} = \begin{bmatrix} {}^{1}e_{\mathrm{u}} & {}^{1}e_{\mathrm{v}} & {}^{1}e_{\mathrm{w}} & {}^{2}e_{\mathrm{u}} & {}^{2}e_{\mathrm{v}} & {}^{2}e_{\mathrm{w}} & {}^{3}e_{\mathrm{u}} & {}^{3}e_{\mathrm{v}} & {}^{3}e_{\mathrm{w}} \end{bmatrix}'. \tag{3.4}$$

In the proposed machine, the phase inductance matrix $\mathbf{L}_{\mathrm{ph}}(\vartheta_{\mathrm{e}})$ varies depending on the electrical position ϑ_{e}, as expressed in the following equations [84]:

$$\mathbf{L}_{\mathrm{ph}}(\vartheta_{\mathrm{e}}) = \begin{bmatrix} \mathbf{L}(\vartheta_{\mathrm{e}}) & \mathbf{M} & \mathbf{M} \\ \mathbf{M} & \mathbf{L}(\vartheta_{\mathrm{e}}) & \mathbf{M} \\ \mathbf{M} & \mathbf{M} & \mathbf{L}(\vartheta_{\mathrm{e}}) \end{bmatrix} \tag{3.5}$$

where

$$\mathbf{L}(\vartheta_{\mathrm{e}}) = \begin{bmatrix} L_{\mathrm{uu}}(\vartheta_{\mathrm{e}}) & M_{\mathrm{vu}}(\vartheta_{\mathrm{e}}) & M_{\mathrm{wu}}(\vartheta_{\mathrm{e}}) \\ M_{\mathrm{uv}}(\vartheta_{\mathrm{e}}) & L_{\mathrm{vv}}(\vartheta_{\mathrm{e}}) & M_{\mathrm{wv}}(\vartheta_{\mathrm{e}}) \\ M_{\mathrm{uw}}(\vartheta_{\mathrm{e}}) & M_{\mathrm{vw}}(\vartheta_{\mathrm{e}}) & L_{\mathrm{ww}}(\vartheta_{\mathrm{e}}) \end{bmatrix} \tag{3.6}$$

and

$$\mathbf{M} = \begin{bmatrix} -M_{\mathrm{c}} & M_{\mathrm{c}} & M_{\mathrm{c}} \\ M_{\mathrm{c}} & -M_{\mathrm{c}} & -M_{\mathrm{c}} \\ M_{\mathrm{c}} & -M_{\mathrm{c}} & -M_{\mathrm{c}} \end{bmatrix}. \tag{3.7}$$

$\mathbf{L}(\vartheta_{\mathrm{e}})$ reported in (3.6) contains the self and mutual inductances of a single three-phase winding, while $\mathbf{M}$ expressed in (3.7) consists of mutual inductances between phases employed in different sectors. As the voltage equation is presented under the assumption of the linear magnetic behaviour, values of mutual inductances between phases belonging to different sectors are identical. If the magnetic saturation is considered, the values of mutual inductances between phases belonging to different sectors are slightly different. The numeric values of elements involved in (3.6) and (3.7) are listed in the following equations:

$$
\begin{aligned}
&L_{\mathrm{uu}}(\vartheta_{\mathrm{e}}) = L_1 + L_2 \cos(2\vartheta_{\mathrm{e}}) \\
&L_{\mathrm{vv}}(\vartheta_{\mathrm{e}}) = L_1 + L_2 \cos\big(2(\vartheta_{\mathrm{e}} - 2\pi/3)\big) \\
&L_{\mathrm{ww}}(\vartheta_{\mathrm{e}}) = L_1 + L_2 \cos\big(2(\vartheta_{\mathrm{e}} - 4\pi/3)\big) \\
&M_{\mathrm{uv}}(\vartheta_{\mathrm{e}}) = M_{\mathrm{vu}}(\vartheta_{\mathrm{e}}) = M_1 + M_2 \cos\big(2(\vartheta_{\mathrm{e}} - \pi/3)\big) \\
&M_{\mathrm{uw}}(\vartheta_{\mathrm{e}}) = M_{\mathrm{wu}}(\vartheta_{\mathrm{e}}) = M_1 + M_2 \cos\big(2(\vartheta_{\mathrm{e}} + \pi/3)\big) \\
&M_{\mathrm{vw}}(\vartheta_{\mathrm{e}}) = M_{\mathrm{wv}}(\vartheta_{\mathrm{e}}) = M_{1\mathrm{d}} + M_{2\mathrm{d}} \cos(2\vartheta_{\mathrm{e}}) \\
&M_{\mathrm{c}} = \text{constant}
\end{aligned}
\tag{3.8}
$$

where the parameters in (3.8) are reported in Table 3.2. Since the lamination of the rotor is salient rather than a circle, the phase inductance values are composed of a DC term and a sinusoidal term.

Table 3.2: Phase inductances [84]

	L_1	L_2	M_1	M_2	$M_{1\mathrm{d}}$	$M_{2\mathrm{d}}$	M_{c}
Value (mH)	0.447	0.126e-2	-0.123	0.304e-2	0.0404	0.303e-2	0.0407

Due to the phase arrangement of each sector, the phase inductance $\mathbf{L}(\vartheta_{\mathrm{e}})$ is different from the one of conventional three-phase machines, $M_{1\mathrm{d}} \neq M_1$. In detail, phase u overlaps with phases v and w two slots, whereas phase v and w overlap with each other one tooth, which is easily observed in Figure 3.1.

3.3 Active suspension force control in a healthy condition

3.3.1 Modular approach to the production of the suspension force and torque in the MS PMSM

The definition of the machine model is required to analyse the electromagnetic behaviour of an electric motor, whose understanding is essential for the development of a suitable control algorithm. Owing to the modularity of the MS

PMSM, the model can be easily defined as function of the $\alpha-\beta$ axis electrical variables of each three-phase sub-winding (with the α-axis aligned with the centre of the north pole of the rotor magnets). It is noted that the $\alpha-\beta$ axis electrical variables are transformed from the three-phase current of each sector by the Clarke transformation.

The key inputs of the MS PMSM model are the $\alpha-\beta$ axis currents of each sector while the outputs are the mechanical suspension forces and torque acting on the rotor, hereinafter referred as wrench $\bar{W}$. The wrench can be defined as a vector of the $x-y$ components of the suspension force (F_x, F_y) and the torque T acting on the rotor:

$$\bar{W} = [F_x, F_y, T]' \tag{3.9}$$

The relation between the $\alpha-\beta$ axis currents of the generic s^{th} sector $({}^s i_\alpha, {}^s i_\beta)$ and their respective contribution to the wrench of the MS PMSM is a function of both $\alpha-\beta$ axis currents and rotor electrical position, as follows:

$${}^s\bar{W} = [{}^sF_x, {}^sF_y, {}^sT]' = f({}^s i_\alpha, {}^s i_\beta, \vartheta_\mathrm{e}). \tag{3.10}$$

Under linear operating conditions and neglecting the coupling among sectors, the wrench produced by the entire machine can be considered as the sum of the effects of all the n_s sectors supplied with the respective $\alpha-\beta$ currents:

$$\bar{W} = \sum_{s=1}^{n_s} {}^s\bar{W} = \sum_{s=1}^{n_s} {}^s f({}^s i_\alpha, {}^s i_\beta, \vartheta_\mathrm{e}). \tag{3.11}$$

The functions ${}^s f$ can be evaluated by accurate analytical models which have been presented in section 2.6 or, for a better accuracy, through FE simulations. Although analytical approaches are computationally efficient, their results need to be FE validated [85]. For this reason, the characterisation of the considered machine, whose details are reported in Table 3.1, is elaborated on via 2D FEAs [84]. Figure 3.2 reports the wrench components of the first sector of the

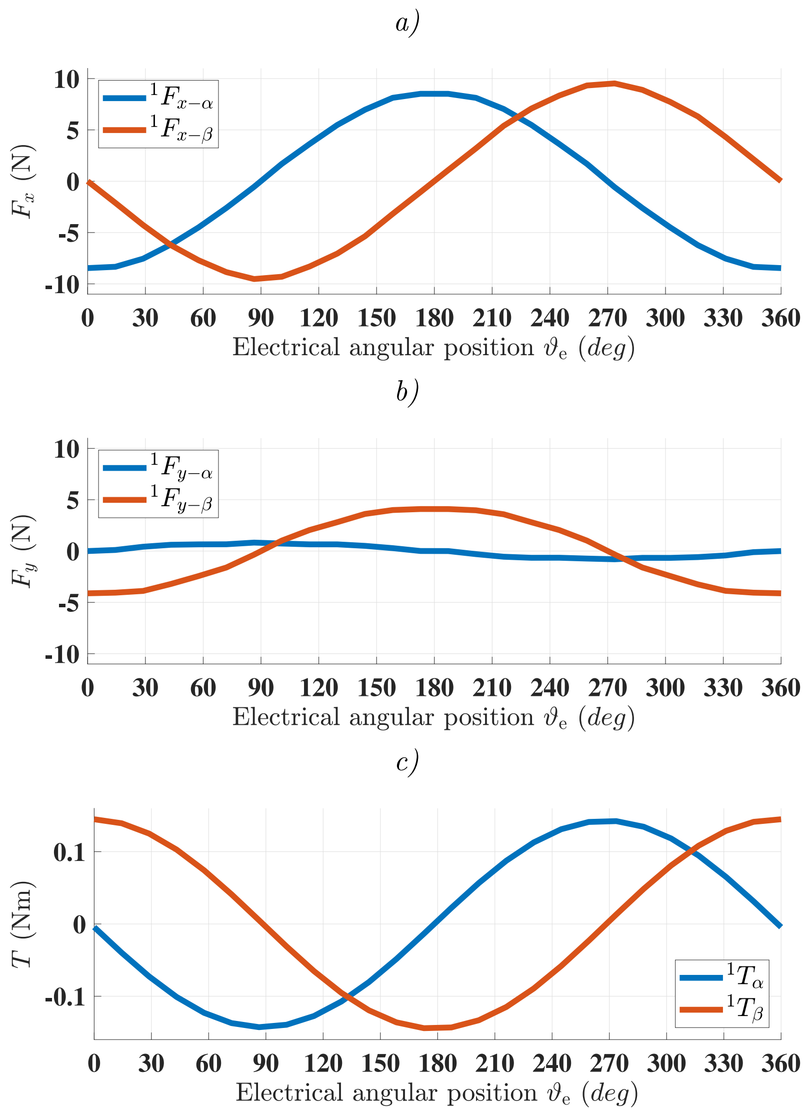

Figure 3.2: *Wrench components of the first sector of the machine with respect to the rotor electrical position. a) Suspension forces acting on the x-axis of the rotor. b) Suspension forces acting on the y-axis of the rotor. c) Torque acting on the rotor.*

machine considered throughout this study (whose first phase is placed on the x-axis). In particular, Figure 3.2 a), b) and c) show the wrench components (F_x, F_y and T) as function of the rotor electrical position when supplied by $1A$ α and β axis currents, respectively. Blue lines represent the wrench generated by $1A$ $\alpha-$axis current of sector 1. Red lines represent the wrench generated by $1A$ $\beta-$axis current of sector 1. $\alpha-$ and β axis currents are separately injected into the first sector of the machine. Figure 3.3 reports the flux density distributions analysed by FE with non-linear material (silicon steel sheet B35AV1900) when supplying positive α axis currents of $0A$, $13A$, and $25A$, respectively. From

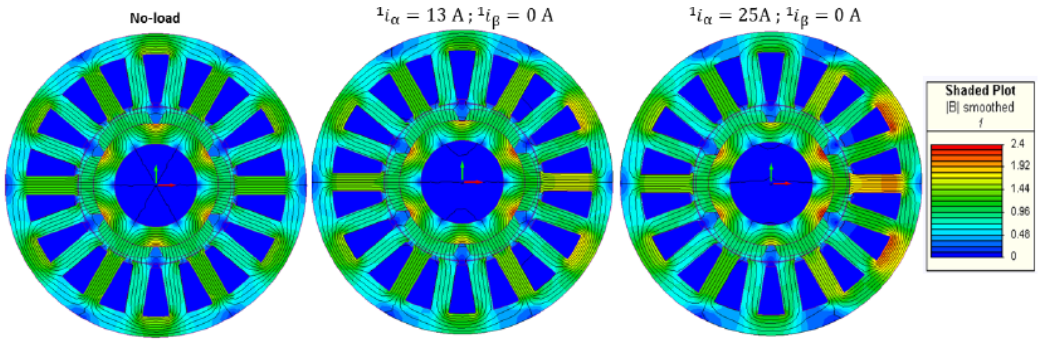

Figure 3.3: *Flux density at no-load operation condition, at I_{rated} (13A), and 25A $\alpha-$ axis current supplied to sector 1 [84]*

.

these flux maps it is possible to appreciate that the soft magnetic material is mainly operating in its linear range within the rated current [84]. Figure 3.4 depicts the amplitudes of wrench components (F_x and F_y) as function of the both α and β axis currents, respectively. In the meantime, Figure 3.5 shows that the torque linearly depends on the quadrature current (i_q) which is on the direct-quadrature coordinate under the rotor rotation reference frame. It can be noticed that force contributions vary almost linearly with the currents up to the rated value (i.e. $13A_{pk}$). Above this value, the saturation of the flux path has a relevant effect only when supplied with positive $\alpha-$axis current (i.e. when straightening the PM flux). Consequentially, the wrench contribution of each sector can be assumed linearly dependent on the respective currents, and so the matrix equation (3.10) can be written as followed:

$$^1\bar{W}(^1i_\alpha, ^1i_\beta, \vartheta_\mathrm{e}) = {}^1\mathbf{K}_{\alpha\beta}(\vartheta_\mathrm{e}) \begin{bmatrix} ^1i_\alpha \\ ^1i_\beta \end{bmatrix} \tag{3.12}$$

where $^1\mathbf{K}_{\alpha\beta}(\vartheta_\mathrm{e})$ is a 3×2 matrix of wrench coefficients, and its detail is reported in (3.13).

$$^1\mathbf{K}_{\alpha\beta}(\vartheta_\mathrm{e}) = \begin{bmatrix} ^1k_{x\alpha}(\vartheta_\mathrm{e}) & ^1k_{x\beta}(\vartheta_\mathrm{e}) \\ ^1k_{y\alpha}(\vartheta_\mathrm{e}) & ^1k_{y\beta}(\vartheta_\mathrm{e}) \\ ^1k_{T\alpha}(\vartheta_\mathrm{e}) & ^1k_{T\beta}(\vartheta_\mathrm{e}) \end{bmatrix} \tag{3.13}$$

The variable $^1k_{\#\varkappa}(\vartheta_\mathrm{e})$, where $\# \in [x, y, T]$, and $\varkappa \in [\alpha, \beta]$ describes the

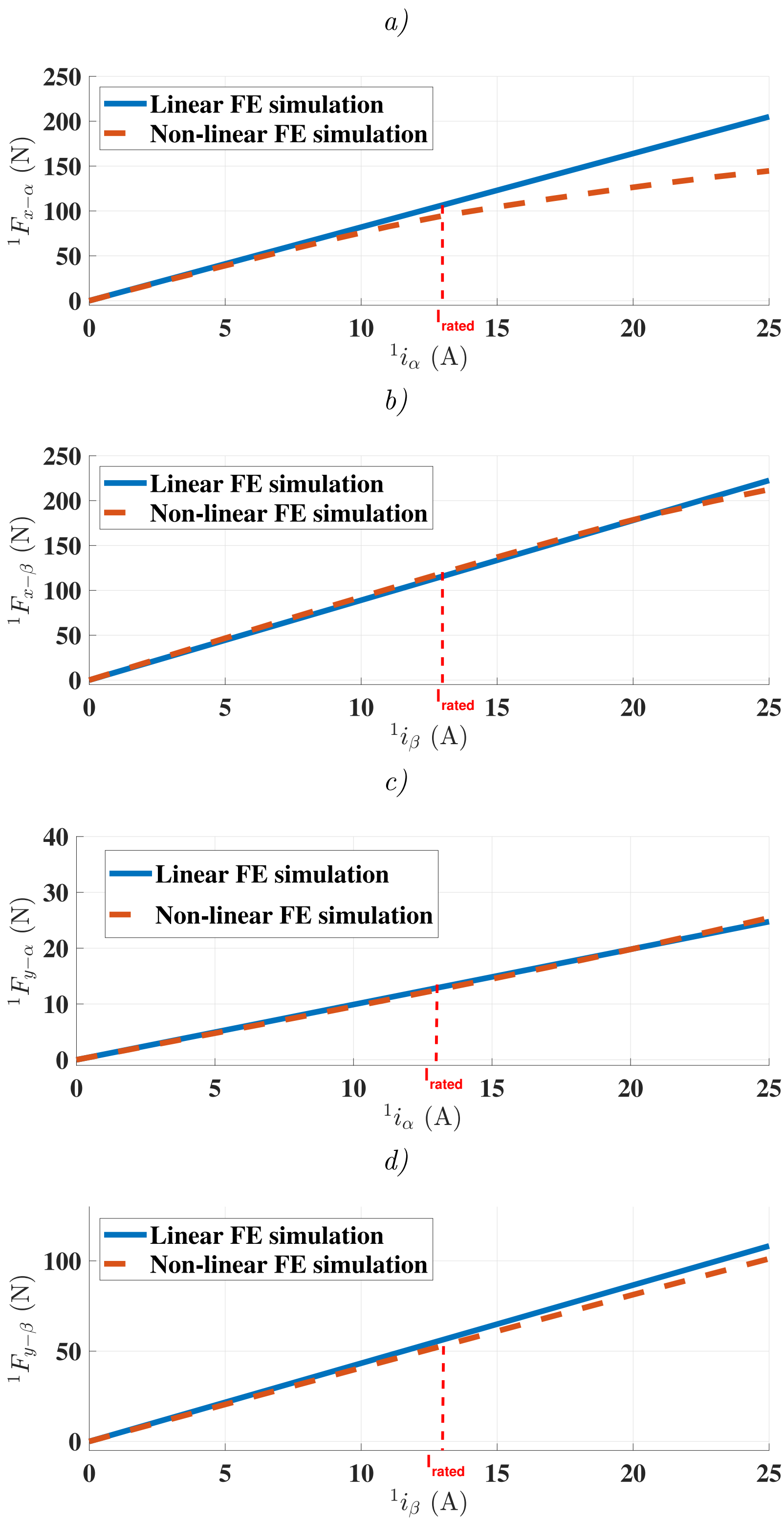

Figure 3.4: *Magnitudes of the generated forces as functions of the α-β currents of the first sector. a) Magnitudes of F_x generated by the $\alpha-$ axis current. b) Magnitudes of F_x generated by the $\beta-$ axis current. c) Magnitudes of F_y generated by the $\alpha-$ axis current. d) Magnitudes of F_y generated by the $\beta-$ axis current.*

relationship between the x-axis, y-axis forces, and torque acting on the rotor and the $\varkappa$ axis current of the 1^{st} sector. In fact, the elements involved in

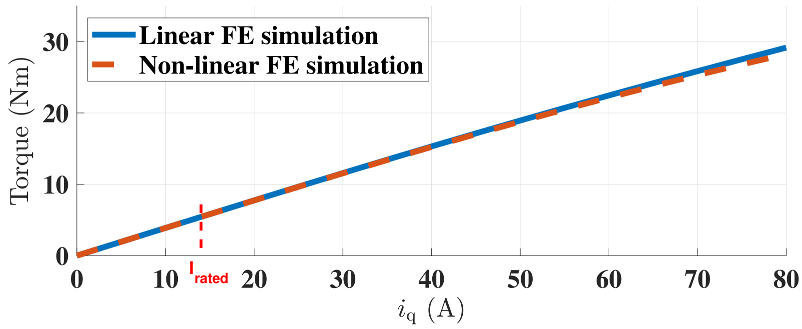

Figure 3.5: *Magnitude of the generated torque as a function of the q-axis current.*

(3.13) are the functions plotted in the Figure 3.2, and they can be expressed as functions of the electrical position through the Fourier series expansion:

$$
\begin{aligned}
{}^{1}k_{x\alpha}(\vartheta_{\mathrm{e}}) &= \sum_{n=0,1,2\cdots}^{+\infty} {}^{1}k_{x\alpha,n^{th}} \cos(n\vartheta_{\mathrm{e}} + {}^{1}\varphi_{x\alpha,n^{th}}) \\
{}^{1}k_{x\beta}(\vartheta_{\mathrm{e}}) &= \sum_{n=0,1,2\cdots}^{+\infty} {}^{1}k_{x\beta,n^{th}} \cos(n\vartheta_{\mathrm{e}} + {}^{1}\varphi_{x\beta,n^{th}}) \\
{}^{1}k_{y\alpha}(\vartheta_{\mathrm{e}}) &= \sum_{n=0,1,2\cdots}^{+\infty} {}^{1}k_{y\alpha,n^{th}} \cos(n\vartheta_{\mathrm{e}} + {}^{1}\varphi_{y\alpha,n^{th}}) \\
{}^{1}k_{y\beta}(\vartheta_{\mathrm{e}}) &= \sum_{n=0,1,2\cdots}^{+\infty} {}^{1}k_{y\beta,n^{th}} \cos(n\vartheta_{\mathrm{e}} + {}^{1}\varphi_{y\beta,n^{th}}) \\
{}^{1}k_{T\alpha}(\vartheta_{\mathrm{e}}) &= \sum_{n=0,1,2\cdots}^{+\infty} {}^{1}k_{T\alpha,n^{th}} \cos(n\vartheta_{\mathrm{e}} + {}^{1}\varphi_{T\alpha,n^{th}}) \\
{}^{1}k_{T\beta}(\vartheta_{\mathrm{e}}) &= \sum_{n=0,1,2\cdots}^{+\infty} {}^{1}k_{T\beta,n^{th}} \cos(n\vartheta_{\mathrm{e}} + {}^{1}\varphi_{T\beta,n^{th}})
\end{aligned}
\tag{3.14}
$$

where n means harmonic order. ${}^{1}k_{\#\varkappa,n^{th}}$ and ${}^{1}\varphi_{\#\varkappa,n^{th}}$, which can be obtained by applying Fast Fourier Transform (FFT) on the curves shown in Figure 3.2, stand for the magnitude and phase angle of the corresponding coefficient ${}^{1}k_{\#\varkappa}(\vartheta_{\mathrm{e}})$, respectively. Figure 3.6 displays the FFT analysis of the curves shown in Figure 3.2 a) and b). Compared to the first order harmonic of each coefficient, the magnitudes of higher harmonic orders are quite small and can be neglected. Hence, ${}^{1}k_{\#\varkappa}(\vartheta_{\mathrm{e}})$ finally consists of only one harmonic and its magnitude and phase delay are displayed in Table 3.3. Particularly, the magnitudes of ${}^{1}k_{T\alpha}(\vartheta_{\mathrm{e}})$ and ${}^{1}k_{T\beta}(\vartheta_{\mathrm{e}})$ are not analysed in Figure 3.6, while

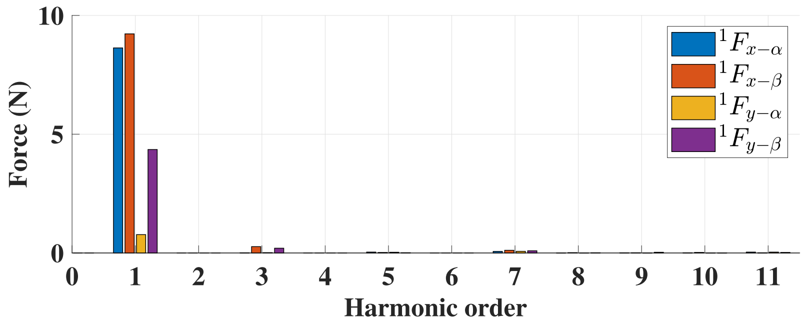

Figure 3.6: *FFT analysis of the curves shown in Figure 3.2.*

they are obtained from the torque constant k_T. In fact, d-q axis currents can be converted to $\alpha-\beta$ reference, then the torque provided by the 1^{st} sector can be expressed as the follows:

$$\begin{aligned} ^1T = \begin{bmatrix} 0 & k_T \end{bmatrix} \begin{bmatrix} ^1i_\mathrm{d} \\ ^1i_\mathrm{q} \end{bmatrix} &= \begin{bmatrix} 0 & k_T \end{bmatrix} \begin{bmatrix} \cos(\vartheta_\mathrm{e}) & \sin(\vartheta_\mathrm{e}) \\ -\sin(\vartheta_\mathrm{e}) & \cos(\vartheta_\mathrm{e}) \end{bmatrix} \begin{bmatrix} ^1i_\alpha \\ ^1i_\beta \end{bmatrix} \\ &= \begin{bmatrix} -k_T\sin(\vartheta_\mathrm{e}) & k_T\cos(\vartheta_\mathrm{e}) \end{bmatrix} \begin{bmatrix} ^1i_\alpha \\ ^1i_\beta \end{bmatrix} \\ &= \begin{bmatrix} ^1k_{T\alpha}(\vartheta_\mathrm{e}) & ^1k_{T\beta}(\vartheta_\mathrm{e}) \end{bmatrix} \begin{bmatrix} ^1i_\alpha \\ ^1i_\beta \end{bmatrix} \end{aligned} \tag{3.15}$$

Obviously, $^1k_{T\alpha}(\vartheta_\mathrm{e})$ and $^1k_{T\beta}(\vartheta_\mathrm{e})$ can be expressed by functions composed of k_T and electrical position, as presented in (3.16).

$$\begin{aligned} ^1k_{T\alpha}(\vartheta_\mathrm{e}) &= -k_T\sin(\vartheta_\mathrm{e}) \\ ^1k_{T\beta}(\vartheta_\mathrm{e}) &= k_T\cos(\vartheta_\mathrm{e}). \end{aligned} \tag{3.16}$$

This approximation is strictly valid when working within the linear region

Table 3.3: Wrench coefficient [84]

Coefficients	$^1k_{x\alpha}(\vartheta_\mathrm{e})$	$^1k_{x\beta}(\vartheta_\mathrm{e})$	$^1k_{y\alpha}(\vartheta_\mathrm{e})$	$^1k_{y\beta}(\vartheta_\mathrm{e})$	$^1k_{T\alpha}(\vartheta_\mathrm{e})$	$^1k_{T\beta}(\vartheta_\mathrm{e})$
Magnitudes	8.28	8.91	0.92	4.37	0.1282	0.1282
Phase angle	π	$\frac{\pi}{2}$	$-\frac{\pi}{2}$	π	$\frac{\pi}{2}$	0

of the wrench-current relationship as reported in Figure 3.4 and Figure 3.5.

Outside this area, each coefficient of the matrix would mainly depends on the respective current. In principle, the same identification procedure should be carried out for all sectors of the machine. However, being each sector rotated with respect to the adjacent one, under an assumption of neglecting the interaction between sectors, the wrench of the generic s^{th} sector can be evaluated by simply taking into account the mechanical shift ${}^{s}\gamma$ of the considered stator sector, as follows:

$$ {}^{s}\bar{W}({}^{s}i_{\alpha}, {}^{s}i_{\beta}, \vartheta_{\mathrm{e}}) = {}^{s}\mathbf{T}_{rot}\, {}^{1}\mathbf{K}_{\alpha\beta}(\vartheta_{\mathrm{e}}) \begin{bmatrix} {}^{s}i_{\alpha} \\ {}^{s}i_{\beta} \end{bmatrix} \tag{3.17} $$

where ${}^{s}\mathbf{T}_{rot}$ is a rotational matrix defined as:

$$ {}^{s}\mathbf{T}_{rot} = \begin{bmatrix} \cos({}^{s}\gamma) & -\sin({}^{s}\gamma) & 0 \\ \sin({}^{s}\gamma) & \cos({}^{s}\gamma) & 0 \\ 0 & 0 & 1 \end{bmatrix} \tag{3.18} $$

Finally, for the prototype machine in the thesis, the overall wrench produced by all the sectors is obtained from (3.11) and (3.17), as follows:

$$ \bar{W} = \sum_{s=1}^{n_s=3} {}^{s}\mathbf{K}_{\alpha\beta}(\vartheta_{\mathrm{e}}) \begin{bmatrix} {}^{s}i_{\alpha} \\ {}^{s}i_{\beta} \end{bmatrix} = \mathbf{K}_{\alpha\beta}(\vartheta_{\mathrm{e}}) \bar{i}_{\alpha\beta} \tag{3.19} $$

where the $\mathbf{K}_{\alpha\beta}(\vartheta_{\mathrm{e}})$ is a 3×6 matrix built by stacking the columns of the ${}^{s}\mathbf{K}_{\alpha\beta}(\vartheta_{\mathrm{e}})$ matrices obtained by (3.17) while the total current vector is $\bar{i}_{\alpha\beta} = [{}^{1}i_{\alpha}, {}^{1}i_{\beta}, {}^{2}i_{\alpha}, {}^{2}i_{\beta}, {}^{3}i_{\alpha}, {}^{3}i_{\beta}]'$. In detail, $\mathbf{K}_{\alpha\beta}(\vartheta_{\mathrm{e}})$ can be written in the following expression:

$$ \mathbf{K}_{\alpha\beta}(\vartheta_{\mathrm{e}}) = \begin{bmatrix} {}^{1}\mathbf{K}_{\alpha\beta}(\vartheta_{\mathrm{e}}) & {}^{2}\mathbf{K}_{\alpha\beta}(\vartheta_{\mathrm{e}}) & {}^{3}\mathbf{K}_{\alpha\beta}(\vartheta_{\mathrm{e}}) \end{bmatrix}. \tag{3.20} $$

The assumption underling (3.11) and (3.17), i.e., neglecting the mutual interactions among the machine sectors, will be further analysed and validated in section 3.5.

3.3.2 Control strategies of the suspension force and torque

Once the wrench-current function is identified, its inversion needs to be carried out in order to control the machine, i.e. finding the current set points which generate a given reference wrench ($\bar{W}^*$). Being the wrench-current relationship (3.19) an underdetermined system, its inverse problem has more than one solution. Among all the possible solutions to this kind of control problems, the result that minimises the stator copper loss is recognised as a valuable one within the field of multi-phase machines control [32]. In fact, supposing that the solution to the underdetermined system (3.19) has to satisfy the objective of minimising the joule losses ($P_{J,tot}$), the solution can be expressed as:

$$\begin{aligned} &\min\ P_{J,tot} = \bar{i}'_{\alpha\beta} \cdot \mathbf{R} \cdot \bar{i}_{\alpha\beta} \\ &s.t.\ \bar{W}^* = \mathbf{K}_{\alpha\beta}(\vartheta_{\mathrm{e}}) \cdot \bar{i}_{\alpha\beta} \end{aligned} \tag{3.21}$$

where $\mathbf{R}$ is the diagonal matrix of the phase resistances. (3.21) is a classic quadratic optimisation problem which can be solved applying the Langrange multiplier method, leading to the well-known result:

$$\bar{i}^*_{\alpha\beta} = \mathbf{K}'_{\alpha\beta}(\vartheta_{\mathrm{e}})[\mathbf{K}_{\alpha\beta}(\vartheta_{\mathrm{e}})\mathbf{K}'_{\alpha\beta}(\vartheta_{\mathrm{e}})]^{-1}\bar{W}^* = \mathbf{K}^+_{\alpha\beta}(\vartheta_{\mathrm{e}})\bar{W}^* \tag{3.22}$$

where $\mathbf{K}^+_{\alpha\beta}(\vartheta_{\mathrm{e}})$ is the Moore-Penrose inverse of the matrix $\mathbf{K}_{\alpha\beta}(\vartheta_{\mathrm{e}})$. In general, the Moore-Penrose inverse represents the solution of an underdetermined system of equation minimising the square of the input variables, which in this case is proportional to the stator Joule loss $P_{J,tot}$.

The current reference $\bar{i}^*_{\alpha\beta}$ obtained from (3.22) is based on the assumption that the interactions between sectors are neglected, so the results obtained from (3.22) should be verified by FEA. The validation will be presented in section 3.5.

3.4 Active suspension force control in faulty operations

3.4.1 Algorithm for generating the suspension force and torque with a three-phase open-circuit fault

The MS-PMSM is supplied by three independent inverters. Power electronic inverters may break down because of some unforeseeable reasons such as overload and capacitor breakdown [86]. As a result, the MS-PMSM loses the contribution of the faulty sector to the suspension force and torque generation, as shown in Figure 3.7. However, the forces and torque can still be generated by

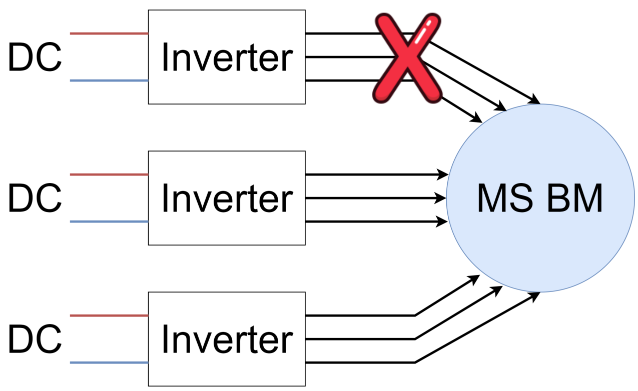

Figure 3.7: *Schematic diagram of the system with a TPOC fault. The MS BM loses the contribution of the faulty sector.*

the remaining two healthy sectors, and the bearingless drive continues to operate. In a TPOC fault condition, the three-phase current of the faulty sector drops to zero. Therefore, the matrix formulation can be written in case of a TPOC fault in sector s simply setting the related sub-matrix ${}^{s}\mathbf{K}_{\alpha\beta}(\vartheta_{\mathrm{e}})$ to 0, shown in (3.23)

$$
\begin{aligned}
\mathbf{K}_{\alpha\beta,\mathrm{f1}}(\vartheta_\mathrm{e}) &= \begin{bmatrix} \mathbf{0} & {}^2\mathbf{K}_{\alpha\beta}(\vartheta_\mathrm{e}) & {}^3\mathbf{K}_{\alpha\beta}(\vartheta_\mathrm{e}) \end{bmatrix} \\
&= \begin{bmatrix} 0 & 0 & {}^2k_{x\alpha}(\vartheta_\mathrm{e}) & {}^2k_{x\beta}(\vartheta_\mathrm{e}) & {}^3k_{x\alpha}(\vartheta_\mathrm{e}) & {}^3k_{x\beta}(\vartheta_\mathrm{e}) \\ 0 & 0 & {}^2k_{y\alpha}(\vartheta_\mathrm{e}) & {}^2k_{y\beta}(\vartheta_\mathrm{e}) & {}^3k_{y\alpha}(\vartheta_\mathrm{e}) & {}^3k_{y\beta}(\vartheta_\mathrm{e}) \\ 0 & 0 & {}^2k_{T\alpha}(\vartheta_\mathrm{e}) & {}^2k_{T\beta}(\vartheta_\mathrm{e}) & {}^3k_{T\alpha}(\vartheta_\mathrm{e}) & {}^3k_{T\beta}(\vartheta_\mathrm{e}) \end{bmatrix} \\
\mathbf{K}_{\alpha\beta,\mathrm{f2}}(\vartheta_\mathrm{e}) &= \begin{bmatrix} {}^1\mathbf{K}_{\alpha\beta}(\vartheta_\mathrm{e}) & 0 & {}^3\mathbf{K}_{\alpha\beta}(\vartheta_\mathrm{e}) \end{bmatrix} \\
&= \begin{bmatrix} {}^1k_{x\alpha}(\vartheta_\mathrm{e}) & {}^1k_{x\beta}(\vartheta_\mathrm{e}) & 0 & 0 & {}^3k_{x\alpha}(\vartheta_\mathrm{e}) & {}^3k_{x\beta}(\vartheta_\mathrm{e}) \\ {}^1k_{y\alpha}(\vartheta_\mathrm{e}) & {}^1k_{y\beta}(\vartheta_\mathrm{e}) & 0 & 0 & {}^3k_{y\alpha}(\vartheta_\mathrm{e}) & {}^3k_{y\beta}(\vartheta_\mathrm{e}) \\ {}^1k_{T\alpha}(\vartheta_\mathrm{e}) & {}^1k_{T\beta}(\vartheta_\mathrm{e}) & 0 & 0 & {}^3k_{T\alpha}(\vartheta_\mathrm{e}) & {}^3k_{T\beta}(\vartheta_\mathrm{e}) \end{bmatrix} \\
\mathbf{K}_{\alpha\beta,\mathrm{f3}}(\vartheta_\mathrm{e}) &= \begin{bmatrix} {}^1\mathbf{K}_{\alpha\beta}(\vartheta_\mathrm{e}) & {}^2\mathbf{K}_{\alpha\beta}(\vartheta_\mathrm{e}) & 0 \end{bmatrix} \\
&= \begin{bmatrix} {}^1k_{x\alpha}(\vartheta_\mathrm{e}) & {}^1k_{x\beta}(\vartheta_\mathrm{e}) & {}^2k_{x\alpha}(\vartheta_\mathrm{e}) & {}^2k_{x\beta}(\vartheta_\mathrm{e}) & 0 & 0 \\ {}^1k_{y\alpha}(\vartheta_\mathrm{e}) & {}^1k_{y\beta}(\vartheta_\mathrm{e}) & {}^2k_{y\alpha}(\vartheta_\mathrm{e}) & {}^2k_{y\beta}(\vartheta_\mathrm{e}) & 0 & 0 \\ {}^1k_{T\alpha}(\vartheta_\mathrm{e}) & {}^1k_{T\beta}(\vartheta_\mathrm{e}) & {}^2k_{T\alpha}(\vartheta_\mathrm{e}) & {}^2k_{T\beta}(\vartheta_\mathrm{e}) & 0 & 0 \end{bmatrix}
\end{aligned}
\tag{3.23}
$$

for a TPOC fault in sector 1, 2 and 3, respectively. Matrices $\mathbf{K}_{\alpha\beta,\mathrm{f1}}(\vartheta_\mathrm{e})$, $\mathbf{K}_{\alpha\beta,\mathrm{f2}}(\vartheta_\mathrm{e})$, and $\mathbf{K}_{\alpha\beta,\mathrm{f3}}(\vartheta_\mathrm{e})$ are also rectangular; hence, their pseudo-inverses can still be computed with (3.22) replacing $\mathbf{K}_{\alpha\beta}(\vartheta_\mathrm{e})$ with $\mathbf{K}_{\alpha\beta,\mathrm{fs}}(\vartheta_\mathrm{e})$. Finally, the current reference can be calculated by (3.24)

$$
\bar{i}^*_{\alpha\beta} = \mathbf{K}^+_{\alpha\beta,\mathrm{fs}}(\vartheta_\mathrm{e})\bar{W}^* \tag{3.24}
$$

where fs means that s-th sector is in TPOC fault condition. The control effect of the algorithm designed for the TPOC fault will be validated by a FE simulation in section 3.5.

3.4.2 Algorithm for generating the suspension force and torque with a single-phase open-circuit fault

To derive the model of the SPOC fault it is convenient to re-write $\mathbf{K}_{\alpha\beta}(\vartheta_\mathrm{e})$ in the uvw three-phase reference frame, as expressed in (3.25)

$$\bar{W} = \mathbf{K}_\mathrm{uvw}(\vartheta_\mathrm{e})\bar{i}_\mathrm{uvw} \tag{3.25}$$

where

$$\mathbf{K}_\mathrm{uvw}(\vartheta_\mathrm{e}) = \mathbf{K}_{\alpha\beta}(\vartheta_\mathrm{e})\mathbf{T}_{C9}\,. \tag{3.26}$$

$\bar{i}_\mathrm{uvw}$ is the nine-phase current vector and $\mathbf{T}_{C9}$ is a nine-phase amplitude invariant Clarke transformation matrix written in the following equations:

$$\mathbf{T}_{C9} = \frac{2}{3}\begin{bmatrix} \mathbf{T}_c & 0 & 0 \\ 0 & \mathbf{T}_c & 0 \\ 0 & 0 & \mathbf{T}_c \end{bmatrix} \tag{3.27}$$

where

$$\mathbf{T}_c = \begin{bmatrix} 1 & -\frac{1}{2} & -\frac{1}{2} \\ 0 & \frac{\sqrt{3}}{2} & -\frac{\sqrt{3}}{2} \end{bmatrix}. \tag{3.28}$$

When a SPOC fault occurs in a sector s, the current of the faulty phase goes to zero while currents of two remaining healthy phases have the identical amplitude but opposite direction due to the series connection. i.e.: Figure 3.8 depicts a three-phase winding with a phase u SPOC fault. In the figure, the

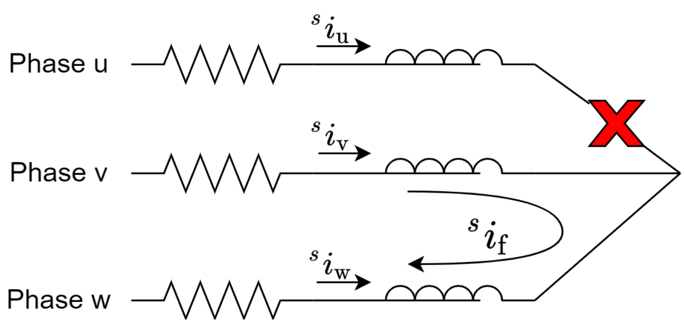

Figure 3.8: *Schematic diagram of a three-phase winding with an open-circuit fault in phase* u.

faulty phase current ${}^{s}i_{\mathrm{u}}$ is 0, while the series current is defined as ${}^{s}i_{\mathrm{f}}$. Then, the three-phase current vector can be expressed as:

$$\begin{bmatrix} {}^{s}i_{\mathrm{u}} \\ {}^{s}i_{\mathrm{v}} \\ {}^{s}i_{\mathrm{w}} \end{bmatrix} = \begin{bmatrix} 0 \\ 1 \\ -1 \end{bmatrix} {}^{s}i_{\mathrm{f}} \tag{3.29}$$

and the wrench vector of corresponding sector is obtained by the following equation:

$${}^{s}\bar{W} = {}^{s}\mathbf{K}_{\mathrm{uvw}}(\vartheta_{\mathrm{e}}) \begin{bmatrix} {}^{s}i_{\mathrm{u}} \\ {}^{s}i_{\mathrm{v}} \\ {}^{s}i_{\mathrm{w}} \end{bmatrix} = {}^{s}\mathbf{K}_{\mathrm{uvw}}(\vartheta_{\mathrm{e}}) \begin{bmatrix} 0 \\ 1 \\ -1 \end{bmatrix} {}^{s}i_{\mathrm{f}} = {}^{s}\mathbf{K}_{\mathrm{uvw,fu}}(\vartheta_{\mathrm{e}})\, {}^{s}i_{\mathrm{f}}\,. \tag{3.30}$$

It is possible to note that a new wrench coefficient sub-matrix ${}^{s}\mathbf{K}_{\mathrm{uvw,fu}}(\vartheta_{\mathrm{e}}) \in \mathbb{R}^{3\times 1}$, applied for sector s phase u open-circuit fault, is obtained by the healthy wrench coefficient matrix and an auxiliary vector $[0\ 1\ -1]'$. The latter is represented by $\mathbf{F}_{\mathrm{u}}$ in the following text. Generalising the above considerations, the SPOC fault in the generic sector s can be then modelled through introducing the auxiliary vector $\mathbf{F}_{\varkappa}$:

$$\begin{aligned} \mathbf{F}_{\mathrm{u}} &= \begin{bmatrix} 0 & 1 & -1 \end{bmatrix}' \\ \mathbf{F}_{\mathrm{v}} &= \begin{bmatrix} 1 & 0 & -1 \end{bmatrix}' \\ \mathbf{F}_{\mathrm{w}} &= \begin{bmatrix} 1 & -1 & 0 \end{bmatrix}' \end{aligned} \tag{3.31}$$

when the faulty phase is u, v, and w, respectively. The wrench coefficient sub-matrix of the faulty sector, which is defined as ${}^{s}\mathbf{K}_{\mathrm{uvw,f}\varkappa}(\vartheta_{\mathrm{e}})$, is obtained by applying the auxiliary vector:

$$ {}^{s}\mathbf{K}_{\mathrm{uvw,f}\varkappa}\left(\vartheta_{\mathrm{e}}\right) = {}^{s}\mathbf{K}_{\mathrm{uvw}}\left(\vartheta_{\mathrm{e}}\right)\mathbf{F}_{\varkappa} = \begin{bmatrix} {}^{s}k_{x\mathrm{f}}(\vartheta_{\mathrm{e}}) \\ {}^{s}k_{y\mathrm{f}}(\vartheta_{\mathrm{e}}) \\ {}^{s}k_{T\mathrm{f}}(\vartheta_{\mathrm{e}}) \end{bmatrix} \tag{3.32} $$

where the subscript $\varkappa$ stands for u, v, and w depending on the faulty phase. ${}^{s}k_{\#\mathrm{f}}(\vartheta_{\mathrm{e}})$ (where $\# \in [x,\, y,\, T,]$) represents the coefficient of the fault sector. It is now possible to construct the coefficient matrix ($\mathbf{K}_{\mathrm{uvw,fs}\varkappa}(\vartheta_{\mathrm{e}})$) of the entire machine for any open circuited phase. For instance, the wrench-current coefficient matrix for an open-circuit fault in phase $\varkappa$ of sector s becomes:

$$ \mathbf{K}_{\mathrm{uvw,fs}\varkappa}(\vartheta_{e}) = \begin{bmatrix} {}^{1}\mathbf{K}_{\mathrm{uvw}}(\vartheta_{\mathrm{e}}) & \cdots & {}^{s}\mathbf{K}_{\mathrm{uvw,f}\varkappa}(\vartheta_{\mathrm{e}}) & \cdots & {}^{n_s}\mathbf{K}_{\mathrm{uvw}}(\vartheta_{\mathrm{e}}) \end{bmatrix} = $$
$$ \begin{bmatrix} {}^{1}k_{x\mathrm{u}}(\vartheta_{\mathrm{e}}) & {}^{1}k_{x\mathrm{v}}(\vartheta_{\mathrm{e}}) & {}^{1}k_{x\mathrm{w}}(\vartheta_{\mathrm{e}}) & \cdots & {}^{s}k_{x\mathrm{f}}(\vartheta_{\mathrm{e}}) & \cdots & {}^{n_s}k_{x\mathrm{u}}(\vartheta_{\mathrm{e}}) & {}^{n_s}k_{x\mathrm{v}}(\vartheta_{\mathrm{e}}) & {}^{n_s}k_{x\mathrm{w}}(\vartheta_{\mathrm{e}}) \\ {}^{1}k_{y\mathrm{u}}(\vartheta_{\mathrm{e}}) & {}^{1}k_{y\mathrm{v}}(\vartheta_{\mathrm{e}}) & {}^{1}k_{y\mathrm{w}}(\vartheta_{\mathrm{e}}) & \cdots & {}^{s}k_{y\mathrm{f}}(\vartheta_{\mathrm{e}}) & \cdots & {}^{n_s}k_{y\mathrm{u}}(\vartheta_{\mathrm{e}}) & {}^{n_s}k_{y\mathrm{v}}(\vartheta_{\mathrm{e}}) & {}^{n_s}k_{y\mathrm{w}}(\vartheta_{\mathrm{e}}) \\ {}^{1}k_{T\mathrm{u}}(\vartheta_{\mathrm{e}}) & {}^{1}k_{T\mathrm{v}}(\vartheta_{\mathrm{e}}) & {}^{1}k_{T\mathrm{w}}(\vartheta_{\mathrm{e}}) & \cdots & {}^{s}k_{T\mathrm{f}}(\vartheta_{\mathrm{e}}) & \cdots & {}^{n_s}k_{T\mathrm{u}}(\vartheta_{\mathrm{e}}) & {}^{n_s}k_{T\mathrm{v}}(\vartheta_{\mathrm{e}}) & {}^{n_s}k_{T\mathrm{w}}(\vartheta_{\mathrm{e}}) \end{bmatrix}. \tag{3.33} $$

Matrix $\mathbf{K}_{\mathrm{uvw,fs}\varkappa}(\theta_{e}) \in \mathbb{R}^{3\times(3n_s-2)}$ is in general rectangular; hence, its pseudo-inverse $\mathbf{K}^{+}_{\mathrm{uvw,fs}\varkappa}(\vartheta_{\mathrm{e}}) \in \mathbb{R}^{(3n_s-2)\times 3}$ is computed by means of (3.22) in order to obtain the faulty reference phase current vector ${}^{\mathrm{fs}\varkappa}\bar{i}^{*}_{\mathrm{uvw}} \in \mathbb{R}^{(3n_s-2)\times 1}$, as expressed in (3.34).

$$ {}^{\mathrm{fs}\varkappa}\bar{i}^{*}_{\mathrm{uvw}} = \mathbf{K}^{+}_{\mathrm{uvw,fs}\varkappa}(\vartheta_{\mathrm{e}})\bar{W}^{*} = \begin{bmatrix} {}^{1}i^{*}_{\mathrm{u}} & {}^{1}i^{*}_{\mathrm{v}} & {}^{1}i^{*}_{\mathrm{w}} \ldots {}^{s}i^{*}_{\mathrm{f}} \ldots {}^{n_s}i^{*}_{\mathrm{u}} & {}^{n_s}i^{*}_{\mathrm{v}} & {}^{n_s}i^{*}_{\mathrm{w}} \end{bmatrix}' \tag{3.34} $$

Then, the reference phase current vector $\bar{i}^{*}_{\mathrm{uvw}} \in \mathbb{R}^{(3n_s)\times 1}$ can be obtained through applying the auxiliary vector, as expressed in (3.35).

$$ \bar{i}^{*}_{\mathrm{uvw}} = \begin{bmatrix} {}^{1}i^{*}_{\mathrm{u}} & {}^{1}i^{*}_{\mathrm{v}} & {}^{1}i^{*}_{\mathrm{w}} \ldots \mathbf{F}'_{\varkappa}\,{}^{s}i^{*}_{\mathrm{f}} \ldots {}^{n_s}i^{*}_{\mathrm{u}} & {}^{n_s}i^{*}_{\mathrm{v}} & {}^{n_s}i^{*}_{\mathrm{w}} \end{bmatrix}' \tag{3.35} $$

For example, if the faulty phase is in sector 1 phase u, the faulty coefficient and faulty reference phase current vector are $\mathbf{K}_{\mathrm{uvw,f1u}}(\vartheta_{\mathrm{e}})$ and ${}^{\mathrm{f1u}}\bar{i}^{*}_{\mathrm{uvw}}$, expressed in (3.36) and (3.37), respectively.

$$\mathbf{K}_{\mathrm{uvw,f1u}}(\vartheta_e) = \begin{bmatrix} {}^{1}\mathbf{K}_{\mathrm{uvw,fu}}(\vartheta_{\mathrm{e}}) & {}^{2}\mathbf{K}_{\mathrm{uvw}}(\vartheta_{\mathrm{e}}) & {}^{3}\mathbf{K}_{\mathrm{uvw}}(\vartheta_{\mathrm{e}}) \end{bmatrix}$$
$$= \begin{bmatrix} {}^{1}k_{x\mathrm{f}}(\vartheta_{\mathrm{e}}) & {}^{2}k_{x\mathrm{u}}(\vartheta_{\mathrm{e}}) & {}^{2}k_{x\mathrm{v}}(\vartheta_{\mathrm{e}}) & {}^{2}k_{x\mathrm{w}}(\vartheta_{\mathrm{e}}) & {}^{3}k_{x\mathrm{u}}(\vartheta_{\mathrm{e}}) & {}^{3}k_{x\mathrm{v}}(\vartheta_{\mathrm{e}}) & {}^{3}k_{x\mathrm{w}}(\vartheta_{\mathrm{e}}) \\ {}^{1}k_{y\mathrm{f}}(\vartheta_{\mathrm{e}}) & {}^{2}k_{y\mathrm{u}}(\vartheta_{\mathrm{e}}) & {}^{2}k_{y\mathrm{v}}(\vartheta_{\mathrm{e}}) & {}^{2}k_{y\mathrm{w}}(\vartheta_{\mathrm{e}}) & {}^{3}k_{y\mathrm{u}}(\vartheta_{\mathrm{e}}) & {}^{3}k_{y\mathrm{v}}(\vartheta_{\mathrm{e}}) & {}^{3}k_{y\mathrm{w}}(\vartheta_{\mathrm{e}}) \\ {}^{1}k_{T\mathrm{f}}(\vartheta_{\mathrm{e}}) & {}^{2}k_{T\mathrm{u}}(\vartheta_{\mathrm{e}}) & {}^{2}k_{T\mathrm{v}}(\vartheta_{\mathrm{e}}) & {}^{2}k_{T\mathrm{w}}(\vartheta_{\mathrm{e}}) & {}^{3}k_{T\mathrm{u}}(\vartheta_{\mathrm{e}}) & {}^{3}k_{T\mathrm{v}}(\vartheta_{\mathrm{e}}) & {}^{3}k_{T\mathrm{w}}(\vartheta_{\mathrm{e}}) \end{bmatrix} \tag{3.36}$$

$$\begin{aligned} {}^{\mathrm{f1u}}\bar{i}^{*}_{\mathrm{uvw}} &= \mathbf{K}^{+}_{\mathrm{uvw,f1u}}(\vartheta_{\mathrm{e}})\bar{W}^{*} \\ &= \begin{bmatrix} {}^{1}i^{*}_{\mathrm{f}} & {}^{2}i^{*}_{\mathrm{u}} & {}^{2}i^{*}_{\mathrm{v}} & {}^{2}i^{*}_{\mathrm{w}} & {}^{3}i^{*}_{\mathrm{u}} & {}^{3}i^{*}_{\mathrm{v}} & {}^{3}i^{*}_{\mathrm{w}} \end{bmatrix}' \end{aligned} \tag{3.37}$$

Consequently, the nine-phase current is obtained by applying the auxiliary matrix $\mathbf{F}_{\mathrm{u}}$, expressed in (3.38).

$$\begin{aligned} \bar{i}^{*}_{\mathrm{uvw}} &= \begin{bmatrix} \mathbf{F}'_{\mathrm{u}}\,{}^{1}i^{*}_{\mathrm{f}} & {}^{2}i^{*}_{\mathrm{u}} & {}^{2}i^{*}_{\mathrm{v}} & {}^{2}i^{*}_{\mathrm{w}} & {}^{3}i^{*}_{\mathrm{u}} & {}^{3}i^{*}_{\mathrm{v}} & {}^{3}i^{*}_{\mathrm{w}} \end{bmatrix}' \\ &= \begin{bmatrix} 0 & {}^{1}i^{*}_{\mathrm{f}} & -{}^{1}i^{*}_{\mathrm{f}} & {}^{2}i^{*}_{\mathrm{u}} & {}^{2}i^{*}_{\mathrm{v}} & {}^{2}i^{*}_{\mathrm{w}} & {}^{3}i^{*}_{\mathrm{u}} & {}^{3}i^{*}_{\mathrm{v}} & {}^{3}i^{*}_{\mathrm{w}} \end{bmatrix}' \end{aligned} \tag{3.38}$$

In a similar manner, the SPOC fault in two sectors can also be represented. i.e.: for the proposed machine, if SPOC faults occur in the phase u of the 1^{st} sector and phase v of the 2^{nd} sector simultaneously, the wrench coefficient matrix of the machine is reported in (3.39).

$$\begin{aligned} \mathbf{K}_{\mathrm{uvw,f1u2v}}(\vartheta_{\mathrm{e}}) &= \begin{bmatrix} {}^{1}\mathbf{K}_{\mathrm{uvw}}(\vartheta_{\mathrm{e}})\mathbf{F}_{\mathrm{u}} & {}^{2}\mathbf{K}_{\mathrm{uvw}}(\vartheta_{\mathrm{e}})\mathbf{F}_{\mathrm{v}} & {}^{3}\mathbf{K}_{\mathrm{uvw}}(\vartheta_{\mathrm{e}}) \end{bmatrix} \\ &= \begin{bmatrix} {}^{1}\mathbf{K}_{\mathrm{uvw,fu}}(\vartheta_{\mathrm{e}}) & {}^{2}\mathbf{K}_{\mathrm{uvw,fv}}(\vartheta_{\mathrm{e}}) & {}^{3}\mathbf{K}_{\mathrm{uvw}}(\vartheta_{\mathrm{e}}) \end{bmatrix} \\ &= \begin{bmatrix} {}^{1}k_{x\mathrm{f}}(\vartheta_{\mathrm{e}}) & {}^{2}k_{x\mathrm{f}}(\vartheta_{\mathrm{e}}) & {}^{3}k_{x\mathrm{u}}(\vartheta_{\mathrm{e}}) & {}^{3}k_{x\mathrm{v}}(\vartheta_{\mathrm{e}}) & {}^{3}k_{x\mathrm{w}}(\vartheta_{\mathrm{e}}) \\ {}^{1}k_{y\mathrm{f}}(\vartheta_{\mathrm{e}}) & {}^{2}k_{y\mathrm{f}}(\vartheta_{\mathrm{e}}) & {}^{3}k_{y\mathrm{u}}(\vartheta_{\mathrm{e}}) & {}^{3}k_{y\mathrm{v}}(\vartheta_{\mathrm{e}}) & {}^{3}k_{y\mathrm{w}}(\vartheta_{\mathrm{e}}) \\ {}^{1}k_{T\mathrm{f}}(\vartheta_{\mathrm{e}}) & {}^{2}k_{T\mathrm{f}}(\vartheta_{\mathrm{e}}) & {}^{3}k_{T\mathrm{u}}(\vartheta_{\mathrm{e}}) & {}^{3}k_{T\mathrm{v}}(\vartheta_{\mathrm{e}}) & {}^{3}k_{T\mathrm{w}}(\vartheta_{\mathrm{e}}) \end{bmatrix} \end{aligned} \tag{3.39}$$

It is possible to note that the size of the coefficient matrix of the healthy machine is 3×9, whereas the size of the matrix $\mathbf{K}_{\mathrm{uvw,fs}\varkappa}(\vartheta_{\mathrm{e}})$ depends on the number of the faulty phase. Two columns will disappear with each single-phase open-circuit fault, i.e.: $\mathbf{K}_{\mathrm{uvw,f1u}}(\vartheta_{\mathrm{e}}) \in 3 \times 7$ and $\mathbf{K}_{\mathrm{uvw,f1u2v}}(\vartheta_{\mathrm{e}}) \in 3 \times 5$.

To obtain the reference current vector, the pseudo-inverse of $\mathbf{K}_{\mathrm{uvw,f1u2v}}(\vartheta_{\mathrm{e}})$ is derived by applying (3.22). Consequently, with a wrench vector reference, the 1^{st} and 2^{nd} sector series currents and the 3^{rd} sector three-phase currents are obtained and expressed in (3.40).

$$^{\mathrm{f1u2v}}\bar{i}^{*}_{\mathrm{uvw}} = \mathbf{K}^{+}_{\mathrm{uvw,f1u2v}}(\vartheta_{\mathrm{e}})\bar{W}^{*} = \begin{bmatrix} {}^{1}i^{*}_{\mathrm{f}} & {}^{2}i^{*}_{\mathrm{f}} & {}^{3}i^{*}_{\mathrm{u}} & {}^{3}i^{*}_{\mathrm{v}} & {}^{3}i^{*}_{\mathrm{w}} \end{bmatrix}' \tag{3.40}$$

Finally, by substituting $\mathbf{F}_{\varkappa}$ into $^{\mathrm{f1u2v}}\bar{i}^{*}_{\mathrm{uvw}}$, nine-phase reference current vector is evaluated from (3.35):

$$\bar{i}^{*}_{\mathrm{uvw}} = \begin{bmatrix} \mathbf{F}'_{\mathrm{u}}\,{}^{1}i^{*}_{\mathrm{f}} & \mathbf{F}'_{\mathrm{v}}\,{}^{2}i^{*}_{\mathrm{f}} & {}^{3}i^{*}_{\mathrm{u}} & {}^{3}i^{*}_{\mathrm{v}} & {}^{3}i^{*}_{\mathrm{w}} \end{bmatrix}'. \tag{3.41}$$

3.4.3 The implementation for controlling the suspension force and torque

Models of the healthy machine, the TPOC faulty machine, and the SPOC faulty machine have been introduced in section 3.3.1, 3.4.1, and 3.4.2, respectively. The wrench coefficient matrices can be transformed to uvw three-phase frame through the transformation matrix introduced in (3.26), though they are expressed in the $\alpha - \beta$ stationary frame for healthy and TPOC fault conditions in the previous sections. By applying (3.22), the inverse of the wrench-current coefficient is obtained in uvw three-phase reference frame. Under the three-phase reference frame, the dimensions of the wrench coefficient matrices vary depending on faulty conditions, resulting in various dimensions in their pseudo-inverses. i.e.:

- $\mathbf{K}_{\mathrm{uvw}}(\vartheta_{\mathrm{e}})$ is a $3 \times 3n_s$ matrix and its pseudo-inverse is a $3n_s \times 3$ matrix.

For the proposed BM in the thesis, $n_s = 3$, the dimensions of matrices are 3×9 and 9×3, respectively.

- $\mathbf{K}_{\mathrm{uvw,f1u}}(\vartheta_{\mathrm{e}})$ is a 3×7 matrix while its pseudo-inverse is a 7×3 matrix.

In order to plot and compare the elements of the coefficient in different faulty scenarios, it is better to extend all SPOC faulty coefficient matrix to 9×3. The inverted coefficient corresponding to the faulty phase can be filled by 0, while the remaining two rows can be occupied by ${}^{s}k^{+}_{x\mathrm{f}}(\vartheta_{\mathrm{e}})$ and $-{}^{s}k^{+}_{x\mathrm{f}}(\vartheta_{\mathrm{e}})$ depending on the auxiliary matrix, where the subscript $+$ means the corresponding variable is an element of the pseudo-inverse matrix. For example, the pseudo-inverse of $\mathbf{K}_{\mathrm{uvw,f1uf2v}}(\vartheta_{\mathrm{e}})$ is expressed in (3.42), and it can be extended to 9×3, as shown in (3.43).

$$\mathbf{K}^{+}_{\mathrm{uvw,f1uf2v}}(\vartheta_{\mathrm{e}}) = \begin{bmatrix} {}^{1}k^{+}_{x\mathrm{f}}(\vartheta_{\mathrm{e}}) & {}^{1}k^{+}_{y\mathrm{f}}(\vartheta_{\mathrm{e}}) & {}^{1}k^{+}_{T\mathrm{f}}(\vartheta_{\mathrm{e}}) \\ {}^{2}k^{+}_{x\mathrm{f}}(\vartheta_{\mathrm{e}}) & {}^{2}k^{+}_{y\mathrm{f}}(\vartheta_{\mathrm{e}}) & {}^{2}k^{+}_{T\mathrm{f}}(\vartheta_{\mathrm{e}}) \\ {}^{3}k^{+}_{xu}(\vartheta_{\mathrm{e}}) & {}^{3}k^{+}_{yu}(\vartheta_{\mathrm{e}}) & {}^{3}k^{+}_{Tu}(\vartheta_{\mathrm{e}}) \\ {}^{3}k^{+}_{xv}(\vartheta_{\mathrm{e}}) & {}^{3}k^{+}_{yv}(\vartheta_{\mathrm{e}}) & {}^{3}k^{+}_{Tv}(\vartheta_{\mathrm{e}}) \\ {}^{3}k^{+}_{xw}(\vartheta_{\mathrm{e}}) & {}^{3}k^{+}_{yw}(\vartheta_{\mathrm{e}}) & {}^{3}k^{+}_{Tw}(\vartheta_{\mathrm{e}}) \end{bmatrix} \tag{3.42}$$

$$\mathbf{K}^{+}_{\mathrm{uvw,f1uf2v}}(\vartheta_{\mathrm{e}}) = \begin{bmatrix} 0 & 0 & 0 \\ {}^{1}k^{+}_{x\mathrm{f}}(\vartheta_{\mathrm{e}}) & {}^{1}k^{+}_{y\mathrm{f}}(\vartheta_{\mathrm{e}}) & {}^{1}k^{+}_{T\mathrm{f}}(\vartheta_{\mathrm{e}}) \\ -{}^{1}k^{+}_{x\mathrm{f}}(\vartheta_{\mathrm{e}}) & -{}^{1}k^{+}_{y\mathrm{f}}(\vartheta_{\mathrm{e}}) & -{}^{1}k^{+}_{T\mathrm{f}}(\vartheta_{\mathrm{e}}) \\ {}^{2}k^{+}_{x\mathrm{f}}(\vartheta_{\mathrm{e}}) & {}^{2}k^{+}_{y\mathrm{f}}(\vartheta_{\mathrm{e}}) & {}^{2}k^{+}_{T\mathrm{f}}(\vartheta_{\mathrm{e}}) \\ 0 & 0 & 0 \\ -{}^{2}k^{+}_{x\mathrm{f}}(\vartheta_{\mathrm{e}}) & -{}^{2}k^{+}_{y\mathrm{f}}(\vartheta_{\mathrm{e}}) & -{}^{2}k^{+}_{T\mathrm{f}}(\vartheta_{\mathrm{e}}) \\ {}^{3}k^{+}_{xu}(\vartheta_{\mathrm{e}}) & {}^{3}k^{+}_{yu}(\vartheta_{\mathrm{e}}) & {}^{3}k^{+}_{Tu}(\vartheta_{\mathrm{e}}) \\ {}^{3}k^{+}_{xv}(\vartheta_{\mathrm{e}}) & {}^{3}k^{+}_{yv}(\vartheta_{\mathrm{e}}) & {}^{3}k^{+}_{Tv}(\vartheta_{\mathrm{e}}) \\ {}^{3}k^{+}_{xw}(\vartheta_{\mathrm{e}}) & {}^{3}k^{+}_{yw}(\vartheta_{\mathrm{e}}) & {}^{3}k^{+}_{Tw}(\vartheta_{\mathrm{e}}) \end{bmatrix} \tag{3.43}$$

Each element of $\mathbf{K}^{+}_{\mathrm{uvw}}(\vartheta_{\mathrm{e}})$ is a function of the rotor electrical position and its graphical representations is shown in Figure 3.9. Blue, red, yellow, and purple lines stand for the coefficient in healthy, sector 1 TPOC fault, sector 1 phase u SPOC fault, and phase u_1v_2 SPOC fault, respectively. It can be noted that

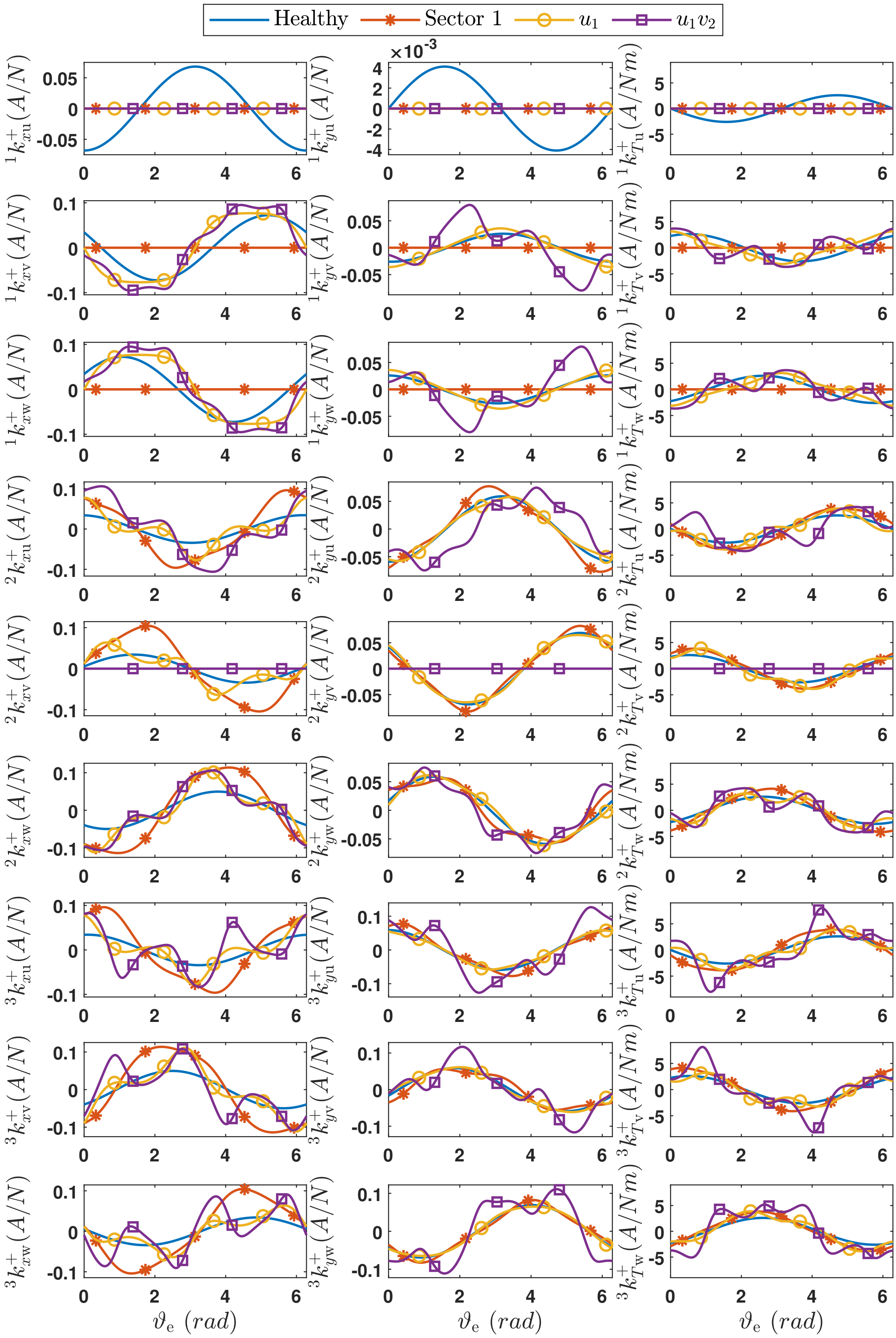

Figure 3.9: *Graphical representation of* ${}^{s}k^{+}_{\#\varkappa}(\vartheta_e)$.

blue lines are non-zero curve in all sub-figures, while lines of other colour have

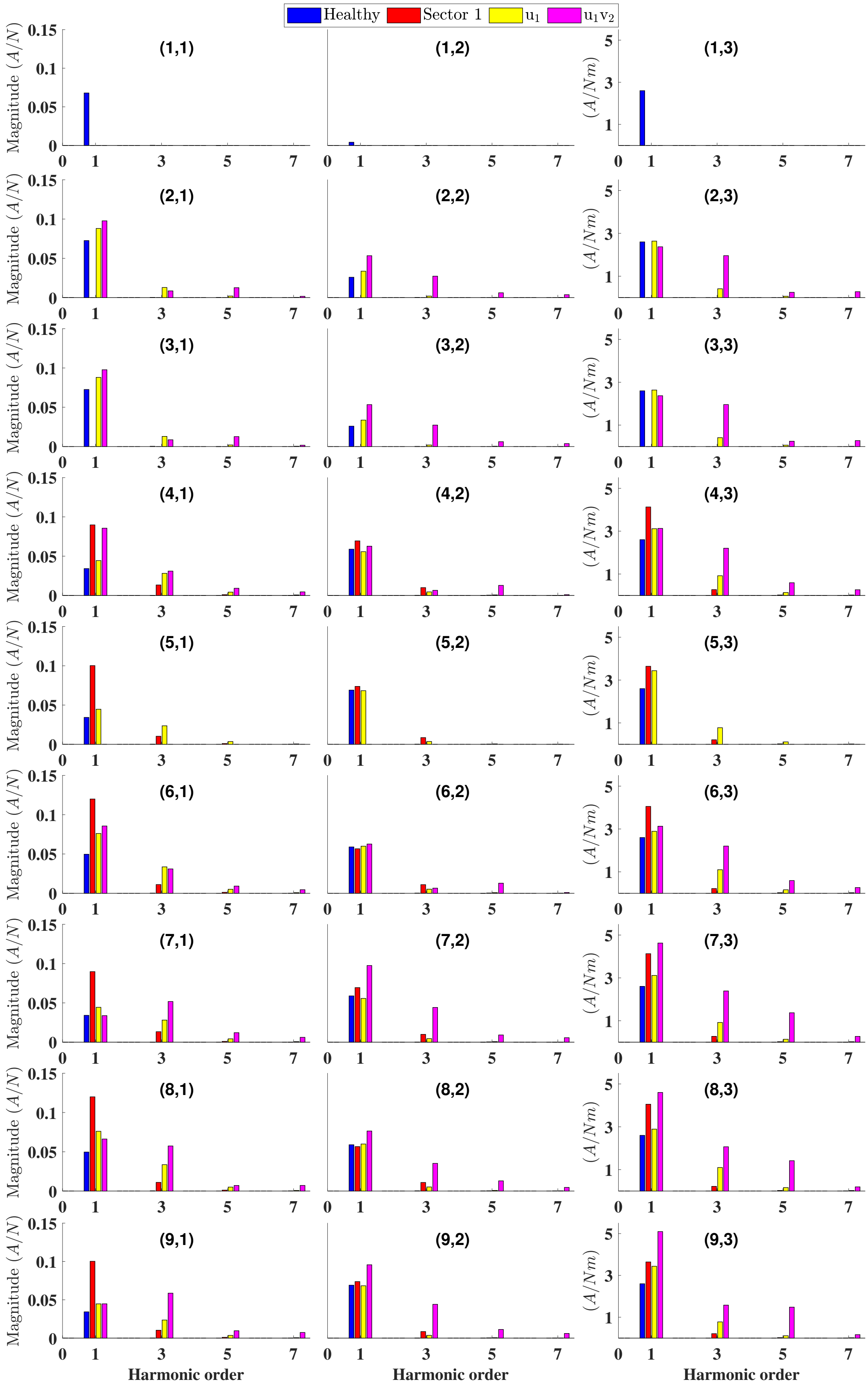

Figure 3.10: *Time harmonic spectrum of* ${}^{s}k^{+}_{\#\varkappa}(\vartheta_{\mathrm{e}})$ *corresponding the Figure 3.9.*

zero value in the faulty phases. Indeed, the red lines of the first three rows keep zero due to the sector 1 TPOC fault while the yellow lines and purple lines have zero value in the first row and the first and fifth rows, respectively. Figure 3.10 displays the harmonic spectrum of the pseudo-inverse matrix coefficients corresponding to the ones in Figure 3.9. It can be noted that while coefficients of the healthy pseudo-inverse matrix appear in all sub-figures, the others are not present in the rows related to the faulty phases. In detail, the first three rows do not display red bars as the three-phase current of sector 1 are equal to zero for a TPOC fault in the same sector. Instead, the first row, and the first and fifth rows do not contain yellow, and pink bars, respectively. It is observed that in healthy condition, harmonic orders higher than one are very small, and can be neglected. Instead, higher order coefficients cannot be neglected in case of a TPOC fault and SPOC fault in one sector or two sectors. The harmonic amplitudes of the 3^{rd} and 5^{th} orders are remarkable and in some cases comparable with the first harmonic order (see pink bars in (7,2) and (9,2)).

Finally, the phase current is computed by combining the reference wrench vector and ${}^{s}k^{+}_{\#\varkappa}(\vartheta_{\mathrm{e}})$ which contains several order harmonics, shown in (3.44).

$$\begin{aligned}{}^{s}i^{*}_{\varkappa} = \sum_{n=0,1,2,\dots}^{+\infty} \Big(& \big({}^{s}k^{+}_{x\varkappa,n^{th}} \cos(n\vartheta_{\mathrm{e}} + {}^{s}\varphi^{+}_{x\varkappa,n^{th}}) \big) F^{*}_{x} \\ & + \big({}^{s}k^{+}_{y\varkappa,n^{th}} \cos(n\vartheta_{\mathrm{e}} + {}^{s}\varphi^{+}_{y\varkappa,n^{th}}) \big) F^{*}_{y} \\ & + \big({}^{s}k^{+}_{T\varkappa,n^{th}} \cos(n\vartheta_{\mathrm{e}} + {}^{s}\varphi^{+}_{T\varkappa,n^{th}}) \big) T^{*} \Big)\end{aligned} \tag{3.44}$$

The ${}^{s}k^{+}_{x\varkappa,n^{th}}$ is the magnitude shown in Figure 3.10, and ${}^{s}\varphi^{+}_{x\varkappa,n^{th}}$ is the phase angle of the corresponding harmonic. Then, the coefficient $\mathbf{K}^{+}_{\mathrm{uvw}}(\vartheta_{\mathrm{e}})$, function of the rotor electrical position, can be stored via look up tables (LUT) on the real time hardware in order to compute the current reference. The fact that the harmonic content in faulty conditions is higher causes heavier computation in the DSP. Hence, harmonics with small magnitudes should be neglected. Indeed, for healthy operating conditions, the harmonics higher than the first order can be neglected, whereas for TPOC or SPOC faulty operating conditions, the harmonics higher than the third order can be neglected. The influence in the force and torque generation of higher harmonic orders in the coefficients will be analysed in section 3.5.

3.5 Validation through simulation

FEA is a good approach to simulate the magnetic and mechanical behaviour of the machine. This section shows the FE simulation results obtained to verify validities of the proposed TPOC and SPOC fault control algorithms and to check if the neglected interaction between sectors, as mentioned in (3.11), (3.17), and (3.22), strongly impacts the force and torque generation. Multi-static non-linear simulations have been performed with the FE commercial software MagNet 7.8.3. The results are presented split into two parts.

The first part aims to verify that the proposed algorithm can carry out a set of appropriate current references (9 phase currents) to provide the desired wrench vector. The magnitude of the reference force vector $|\bar{F}_r|$ is set equal to $100\,N$ while the direction φ_F with respect to the $x-$ axis of Figure 3.1 is set equal to $0\,deg$. The reference load torque is set equal to $2\,Nm$. With the above wrench reference, the pseudo-inverse matrices, $\mathbf{K}^{+}_{\mathrm{uvw}}(\vartheta_{\mathrm{e}})$, $\mathbf{K}^{+}_{\mathrm{uvw,f1}}(\vartheta_{\mathrm{e}})$, and $\mathbf{K}^{+}_{\mathrm{uvw,f1u}}(\vartheta_{\mathrm{e}})$, obtained from (3.22), are applied to calculate the current reference. In this part, all harmonics of pseudo-inverse matrices are considered when the current reference is computed. Figure 3.11, Figure 3.12, and Figure 3.13 show the three-phase current references in the healthy condition, in the phase u_1 open-circuit fault condition, and in the 1^{st} sector open-circuit fault condition, respectively. The current reference is considered as the input of the FE model, and the generated wrench vector is displayed in Figure 3.14. From Figure 3.14, it is worth highlighting that the small deviations between the reference and FE calculated wrench components exist when considering

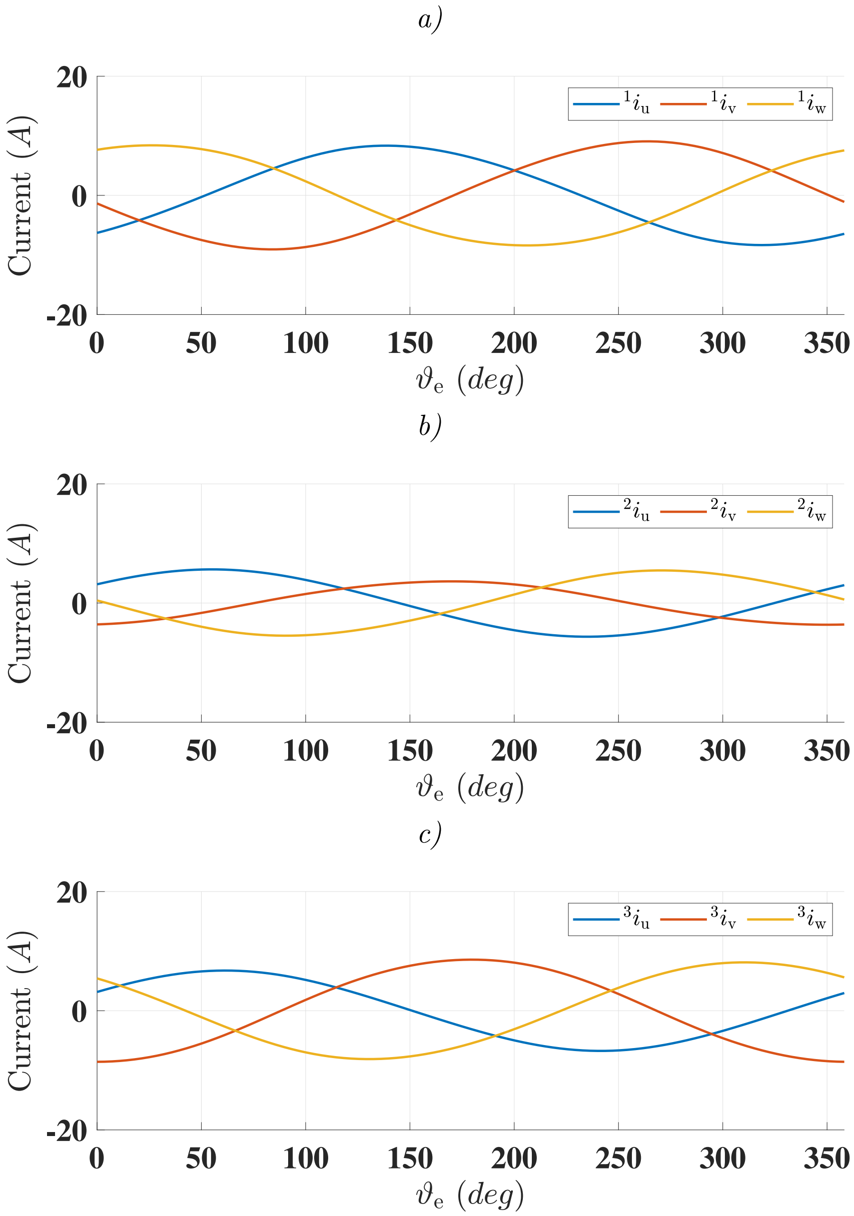

Figure 3.11: *Three-phase currents of three sectors in the healthy condition. a) Sector 1. b) Sector 2. c) Sector 3.*

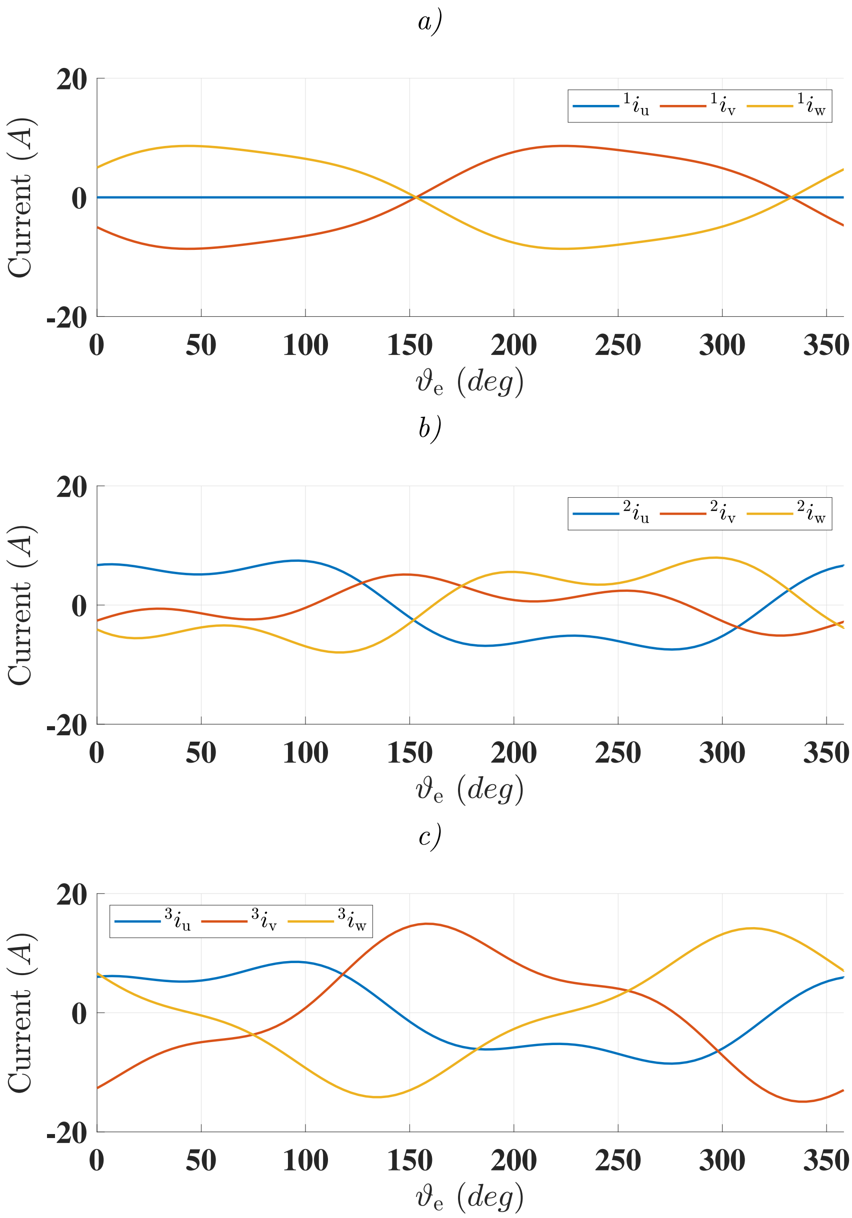

Figure 3.12: *Three-phase currents of three sectors in case of SPOC fault of phase* u_1*. a) Sector 1. b) Sector 2. c) Sector 3.*

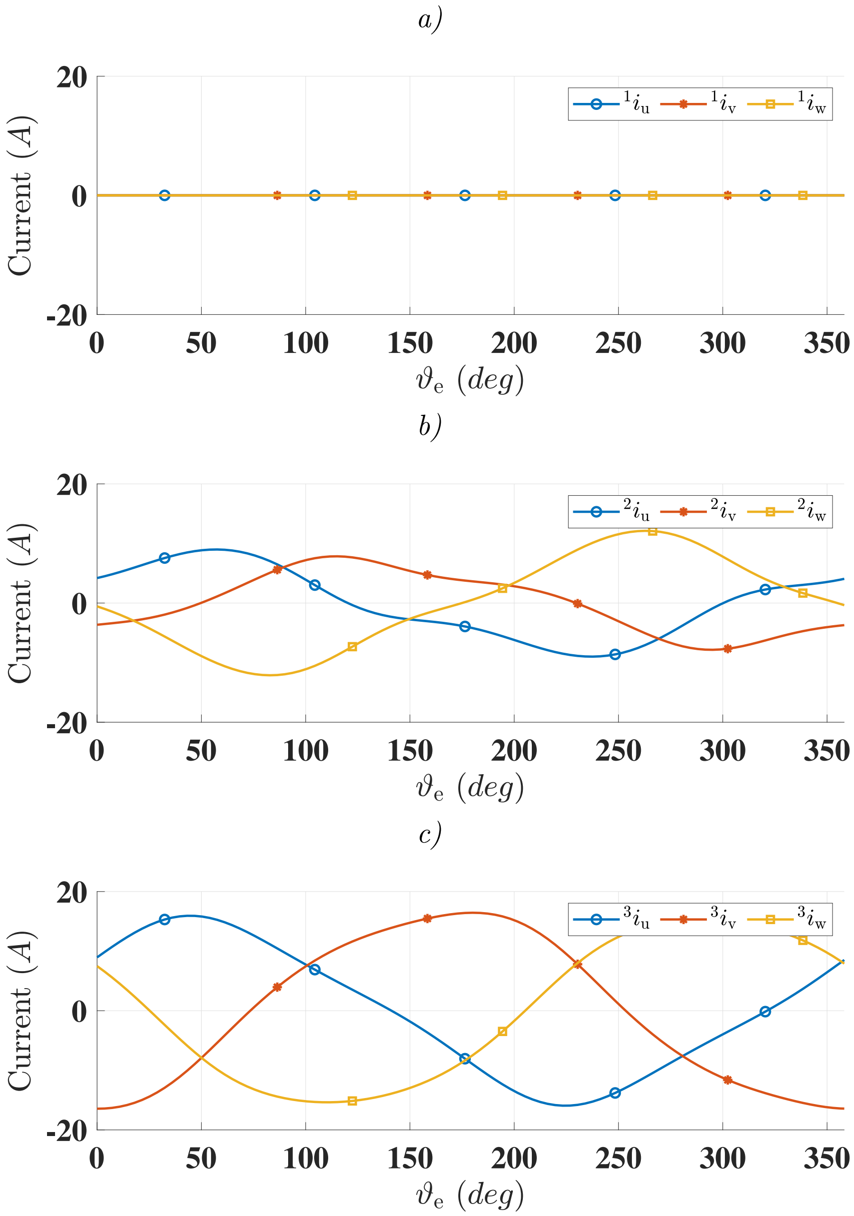

Figure 3.13: *Three-phase currents of three sectors in case of TPOC fault of the* 1^{st} *sector. a) Sector 1. b) Sector 2. c) Sector 3.*

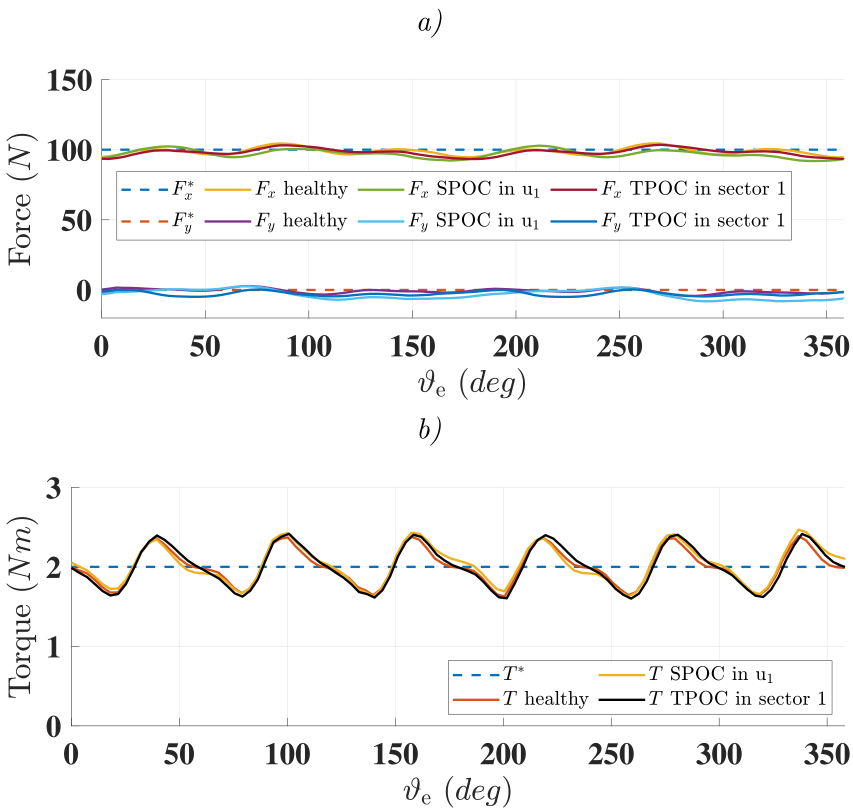

Figure 3.14: *FE simulation results for the suspension force and torque generation in healthy condition, SPOC fault of phase* u_1 *and TPOC fault of sector 1: a) Force generation. b) Torque generation.*

the full harmonic spectrum of all ${}^{s}k^{+}_{\#\varkappa}(\vartheta_e)$. From the previous analyses, these differences are mainly attributed to the mutual interaction among the stator modules. In the meantime, the torque ripple is almost caused by the cogging effect (no load torque). As it can be observed, the proposed SPOC and TPOC fault tolerant techniques are also capable of producing the required suspension force and torque without significantly increasing their ripples. This can be quantified in terms of Total Harmonic Distortion (THD) of $|\bar{F}_r|$ and of the torque T and maximum error of φ_F from the reference direction. Observing the first three rows of Table 3.4, it is possible to note that the THD values of $|\bar{F}_r|$ and T slightly increase from healthy to TPOC fault and SPOC fault, the latter presenting the highest THD value among the three cases considered. However, the SPOC fault posses the advantage of reduced derating of the bearingless drive if compared to the TPOC fault. Indeed, the drive would not lose the contribution of a whole sector to the suspension force and motoring torque

Table 3.4: Force and torque generation quality

	$THD_{\|F\|}$ (%)	Err_{φ_F} (deg)	THD_T (%)
Healthy	7	1.3	27.6
TPOC sector 1	7.7	1.1	29.7
SPOC u_1	9.5	1	31.5
SPOC u_1 and v_2 case I	8.5	1.5	27.7
SPOC u_1 and v_2 case II	18.2	7.4	40.2
SPOC u_1 and v_2 case III	45.5	11.3	40.9

generation but only of one sector phase. This can be observed in the total machine Joule losses which are equal to $12.9\,W$, $18\,W$ and $26.4\,W$ in case of healthy condition, SPOC fault of u_1 and TPOC fault of sector 1, respectively, when the rotational speed is 3000rpm. Overall, the simulation verifies that the proposed healthy, TPOC, and SPOC fault control algorithms are valid. And, the neglected interaction between sectors does not significantly impact the suspension force and torque generation. These errors can be compensated by the outer loop position and speed controllers.

The second part of the simulation examines how the harmonics involved in the pseudo-inverse matrices influence the generated force and torque results. The wrench reference is the same as the one in the previous simulation. Figure 3.15 shows the suspension force and torque generation in case of SPOC fault in two sectors: phase u_1 (sector 1) and v_2 (sector 2). Three different harmonic compositions of the force and torque coefficients, mentioned in (3.44), have been considered. In particular, quantities with suffixes I, II, and III have been generated including the 1^{st}, 3^{rd}, and 5^{th} harmonics, the 1^{st} and 3^{rd} harmonics, and only 1^{st} harmonic, respectively in the force and torque coefficients. The aforementioned harmonics in the coefficients are presented in Figure 3.10 in section 3.4.3. It is straightforward to notice how the quality of the produced force and torque significantly deteriorates when a simplified expression of the

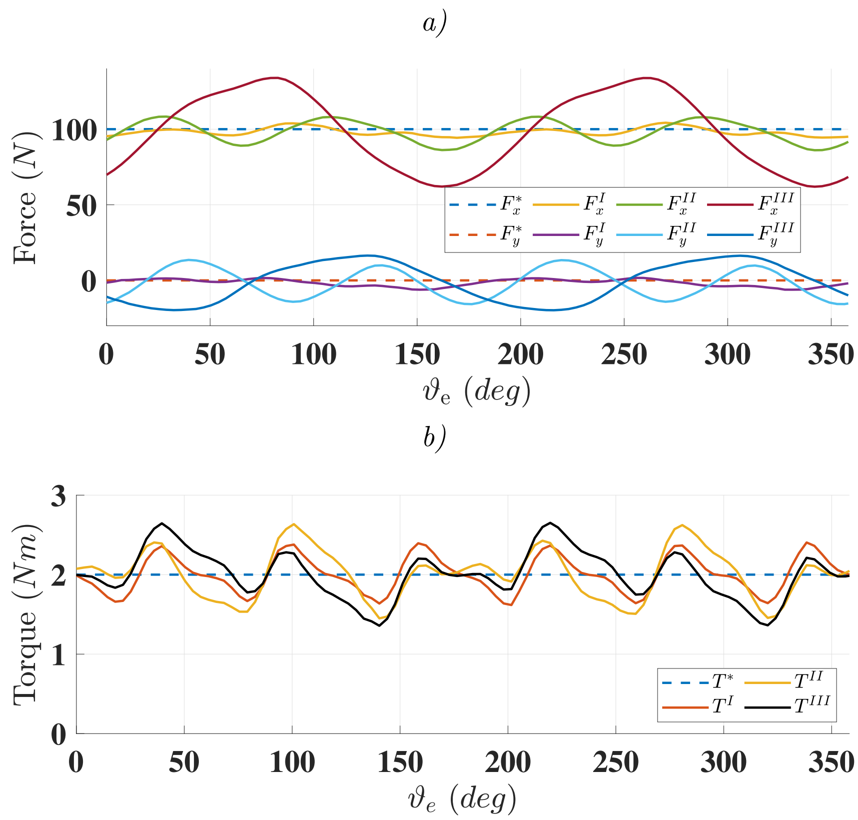

Figure 3.15: *FE simulation results for the suspension force and torque generation in case of SPOC fault of phases* u_1 *and* v_2*: a) Force generation. b) Torque generation.*

coefficients is adopted. This can be quantified in terms of $THD_{|F|}$ and THD_T and maximum error of φ_F by observing the last three rows of Table 3.4. Indeed, $THD_{|F|}$ and THD_T increase from 8.5% and 27.7% % to 45.5 and 40.9 % respectively from case I to III, leading to an unacceptable force and torque quality.

Additionally, Figure 3.16 shows the harmonic spectra of the simulation results presented in Figure 3.15. It can be observed that cases II and III result in undesired harmonic generations in both force and torque compared to case I. It is therefore possible to conclude that an accurate estimation of the force and torque coefficients is necessary in order to guarantee acceptable performances during an open-circuit fault. However, more harmonics mean heavier computations. Therefore, the harmonics involved in the DSP should balance the control performance and the computational load.

Finally, Figure 3.17, Figure 3.18, and Figure 3.19 display the corresponding

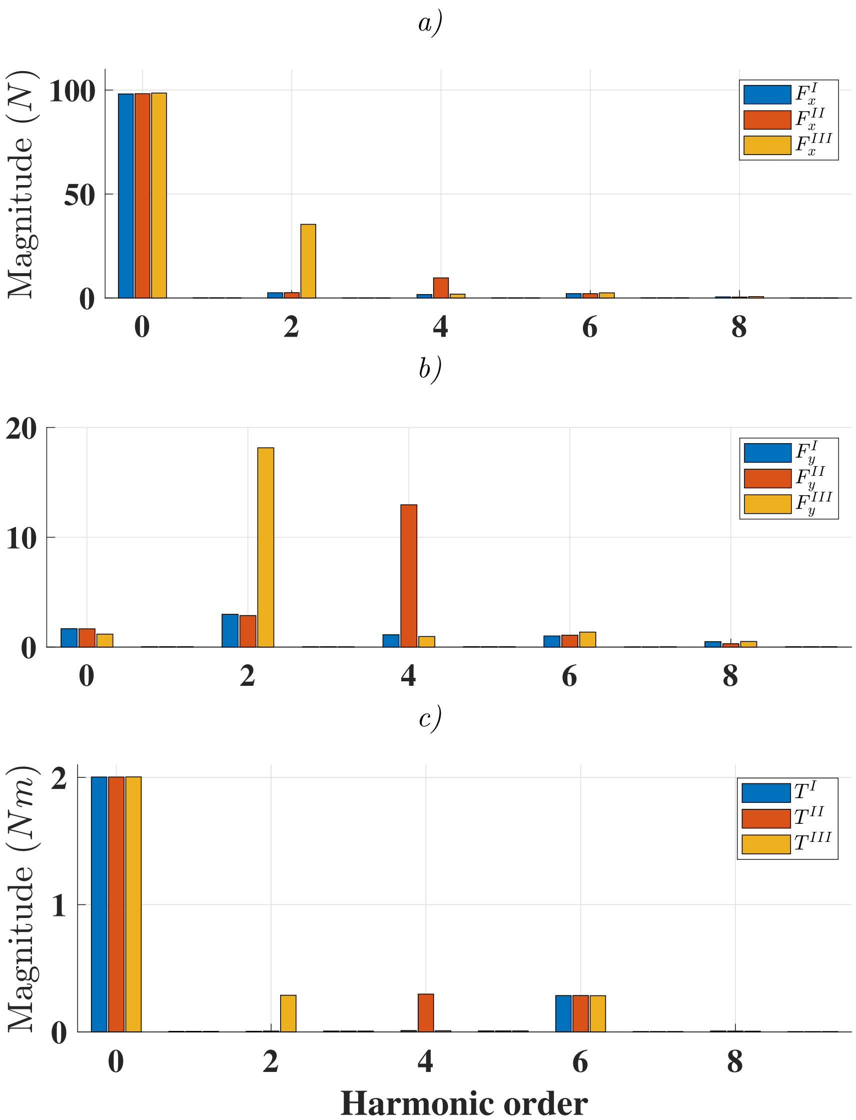

Figure 3.16: *Harmonic spectra of the simulation results in Figure 3.15. a) Harmonic spectrum of F_x. The reference is $100N$. b) Harmonic spectrum of F_y. The reference i s $0N$. c) Harmonic spectrum of T. The reference is $2Nm$.*

current references obtained by three different harmonic compositions. In detail, ${}^s i_{\mathrm{u}}^I$, ${}^s i_{\mathrm{v}}^I$, and ${}^s i_{\mathrm{w}}^I$ in Figure 3.17 represent the current references obtained by the coefficients composed of the 1^{st}, 3^{rd}, and 5^{th} harmonics. ${}^s i_{\mathrm{u}}^{II}$, ${}^s i_{\mathrm{v}}^{II}$, and ${}^s i_{\mathrm{w}}^{II}$ in Figure 3.18 stand for the current references obtained by the coefficients composed of the 1^{st} and 3^{rd} harmonics. ${}^s i_{\mathrm{u}}^{III}$, ${}^s i_{\mathrm{v}}^{III}$, and ${}^s i_{\mathrm{w}}^{III}$ in Figure 3.19 represent the current references obtained by the coefficients composed of the 1^{st} harmonic.

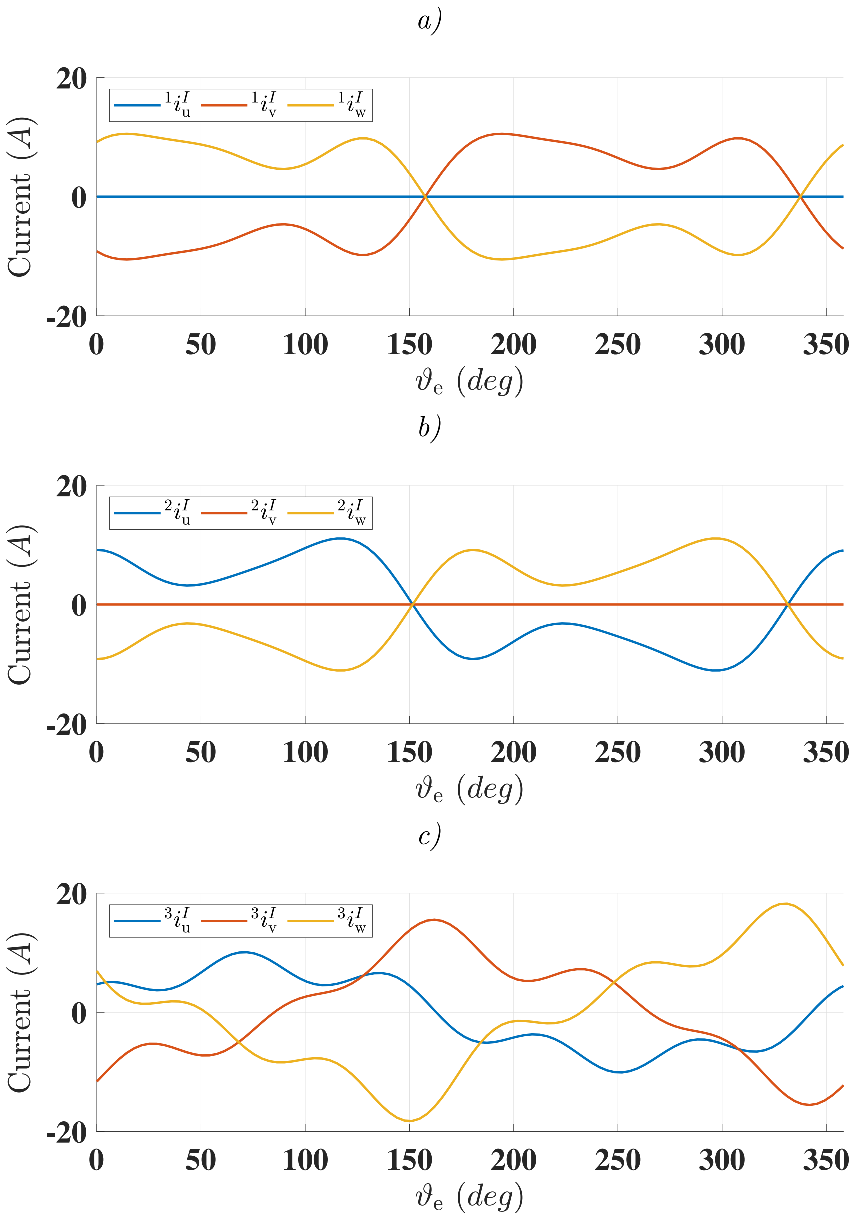

Figure 3.17: *Three-phase currents of three sectors in case of SPOC fault of phases* u_1 *and* v_2*. The* 1^{st}*,* 3^{rd}*, and* 5^{th} *harmonics are included in the current. a) Sector 1. b) Sector 2. c) Sector 3.*

a)

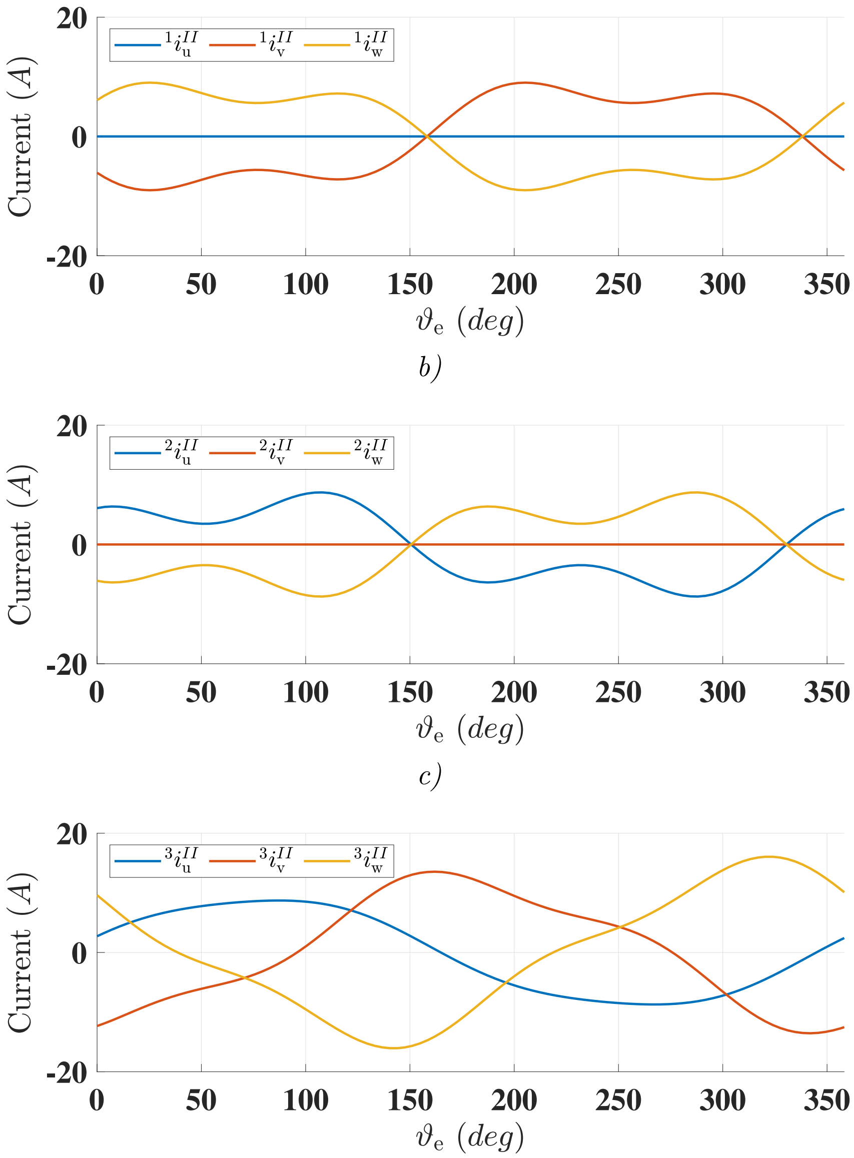

Figure 3.18: *Three-phase currents of three sectors in case of SPOC fault of phases* u_1 *and* v_2*. The* 1^{st} *and* 3^{rd} *harmonics are included in the current. a) Sector 1. b) Sector 2. c) Sector 3.*

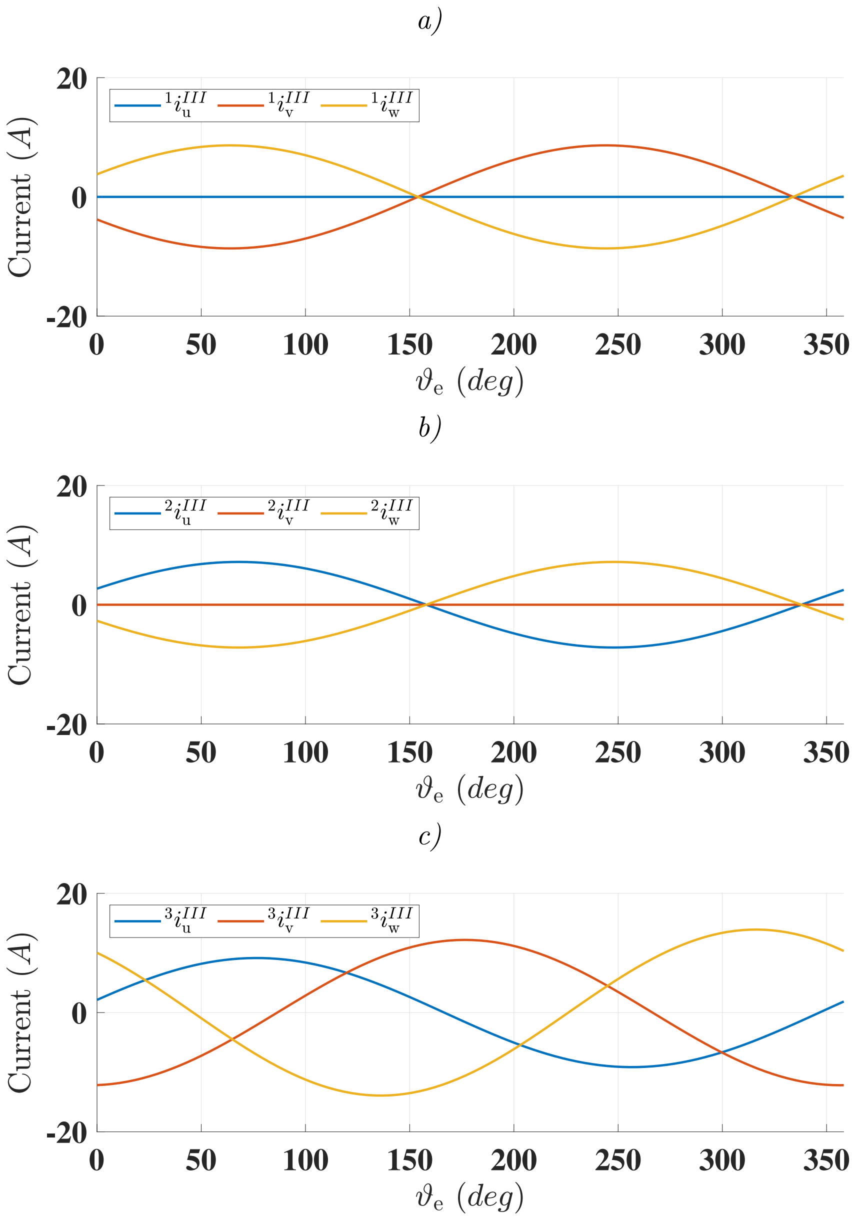

Figure 3.19: *Three-phase currents of three sectors in case of SPOC fault of phases* u_1 *and* v_2*. The* 1^{st} *harmonic is included in the current. a) Sector 1. b) Sector 2. c) Sector 3.*

3.6 Experimental validations

The suspension force and torque control strategy of the proposed BM is introduced and simulated in the previous sections. The FE simulations show that the approach can generate the desired suspension force and torque. Hence, it is now possible to verify the algorithm in experimental tests. In this section, the system diagram of the BM control system is first introduced. Then, the system is built on a prototype MS PMSM that is located at the PEMC Group, University of Nottingham. The TPOC and SPOC fault control strategies are separately validated with under representative load conditions. To switch the control algorithm from healthy condition to faulty conditions, a current filter and an open-circuit fault detector are designed and implemented. Finally, experimental results show the good performance of the proposed control technique.

3.6.1 Bearingless machine control system diagram

Figure 3.20 a) shows the diagram of the implemented BM control system. Green dashed wires are feedbacks measured from the experimental rig, while red wires are supply cables to the machine. Black wires are the signals processed in the DSP. It can be noted that the shaft movement is measured in two directions, x-axis and y-axis. Indeed, the two degrees of the freedom of the shaft is allowed at the drive-end, but it is limited by a backup bearing with a clearance of $150\mu m$. At the non-drive-end of the BM, a self-alignment bearing avoids the axial and x-y displacement of the shaft. Moreover, the system consists of an inner current loop and outer loops, including position and speed loops. The outer loop controllers receive as input the speed and position measurements as well as references, and gives as output the wrench vector reference that can be applied to calculate current reference by the wrench coefficient matrix displayed in Figure 3.20 b). The reference current calculation block selects the appropriate wrench coefficient matrix according to the fault

a)

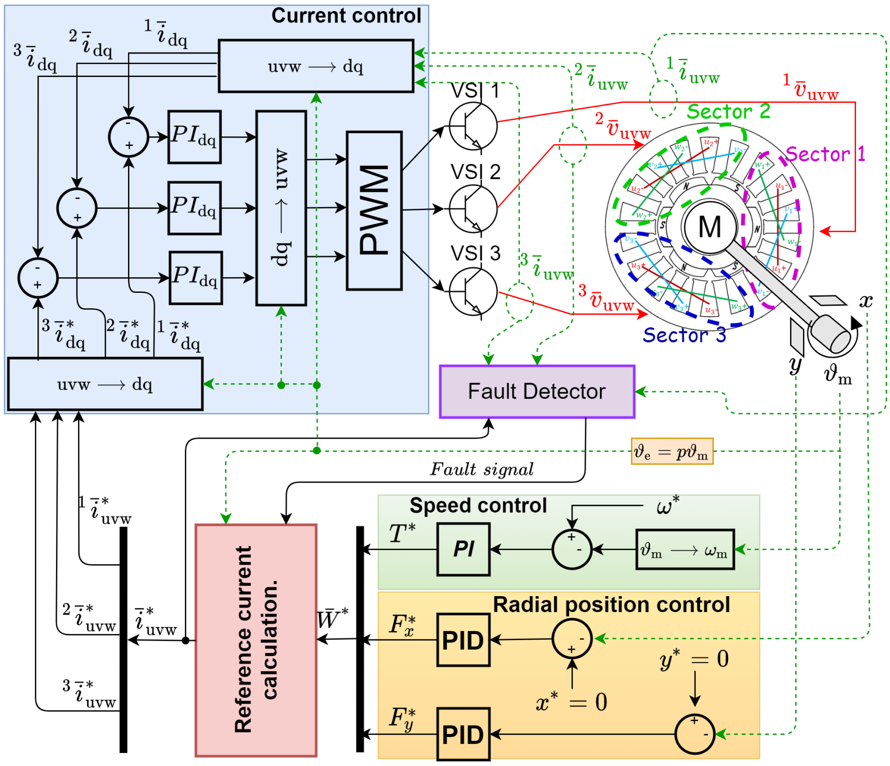

b)

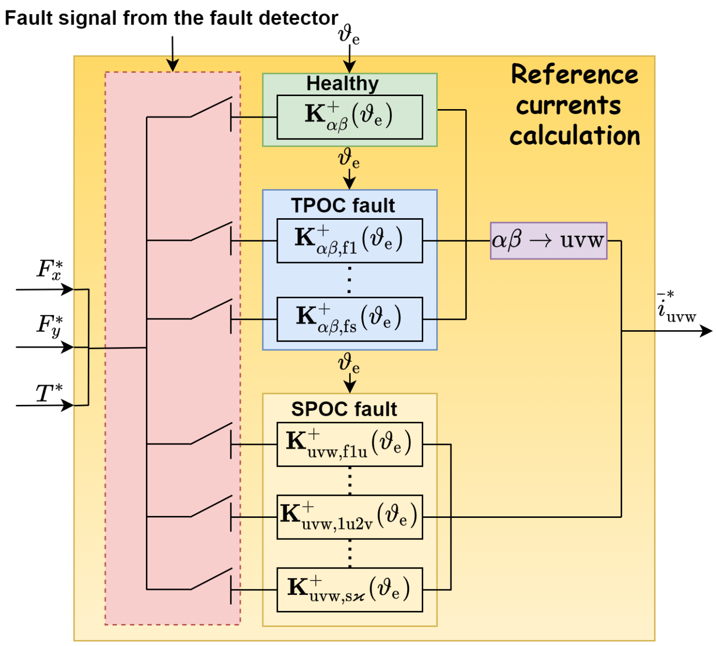

Figure 3.20: *Control diagram of the MS-PMSM. a) BM control system diagram. b) Schematic of the reference current calculation block.*

signal from the fault detector. Six independent conventional PI current controllers are designed and implemented in the current loop, regulating the d-q currents of each sector. When the position controllers and the speed controller

are designed, the assumption is that the current loop guarantees that the feedback to follow the reference with a minimal delay. Consequently, the natural frequency of current controllers should be much faster than that of the speed and position controllers. Finally, voltage references, which are also the outputs of the current controllers, are realized by Sinusoidal Pulse Width Modulation (SPWM) technique with conventional 2-level three-phase power inverters. The currents are measured through the power inverters.
The design of position, speed, current controllers and fault detectors are detailed in the appendix.

3.6.1.1 Open-circuit fault detector

The fault detection technique is an important aspect in fault-tolerant operations and several methods of fault diagnosis for motor drives have already been presented in the literature [87–89]. Especially when dealing with BMs, the fault diagnosis needs to be able to detect the fault in a very short time. Indeed, the control algorithm has to switch from healthy to faulty mode before a rotor touchdown which would result in a potential damage of the rotor and backup bearing element. Moreover, there is a time gap before the controller switches to the faulty mode. The control method and the machine condition are not consistent during the time gap. Therefore, a fault detection technique is required to replicate the real control scenarios. This subsection presents the fault detection strategy designed and implemented in this work.
In modern drive systems, high performance current controllers ensure that the current feedback follows the current reference with only a few sample times of delay. Once an open circuit fault happens, the current of the faulty phase drops to zero but the reference may still be large. If the difference between the current reference and feedback is large while the current feedback signal is zero, it can be assumed that this phase is open circuited.

Both conditions shown in (3.45) and (3.46) must be true for reporting a fault.

$$|i_{\varkappa}| < i_{\text{noise}} \tag{3.45}$$

$$\big||i_{\varkappa}| - |i^*_{\varkappa}|\big| > |i_{\varkappa}|k_h + i_{\text{noise,dyn}} \tag{3.46}$$

If the current feedback $i_{\varkappa}$ and the current reference $i^*_{\varkappa}$ ($\varkappa \in$ [u, v, w]) satisfy (3.45) and (3.46) for a specific period of time which is longer than the designed settling time, fault detector will report a fault signal. In general, current sensors introduce some noise in the current measurement; hence, $i_{\varkappa}$ may not be zero even when the phase is open circuited. i_{noise} is designed as a noise tolerance for current measurement. In this work, i_{noise}, the value reported in Table 3.5, varies depending on the machine rotational speed to achieve the reliable detection performance covering the full speed range. k_h can be set to

Table 3.5: Values of i_{noise}

Rotational speed ω_{m} (rpm)	Value (A)
$\omega_{\text{m}} < 100$	0.05
$100 \leq \omega_{\text{m}} < 200$	0.3
$200 \leq \omega_{\text{m}} < 300$	0.8
$300 \leq \omega_{\text{m}}$	1.3

50% or lower. Measured current cannot follow $i^*_{\varkappa}$ exactly. A small error occurs between $i_{\varkappa}$ and $i^*_{\varkappa}$ during the healthy operation. k_h is designed to avoid fault reporting in healthy condition. However, $|i_{\varkappa}|k_h$ is almost zero when an open circuit fault happens because $|i_{\varkappa}|$ is really small in open circuited condition. $i_{\text{noise,dyn}}$ is designed to avoid reporting a fault when the machine is at low speed and no-load conditions, which have a small value of $i_{\varkappa}$. In the proposed system, $i_{\text{noise,dyn}}$ is set to 0.05. i_{noise} and k_h decide the sensitivity of the fault detection technique.

In order to avoid the noise from the PWM that existed in the current feedback influencing the detection, a low pass filter is required before the fault detector aiming to improve the sensitivity while introducing time delays and phase shift in the sensing loop. Figure 3.21 shows a Butterworth IIR low pass filter that implemented in the experimental system. The parameters of the filter

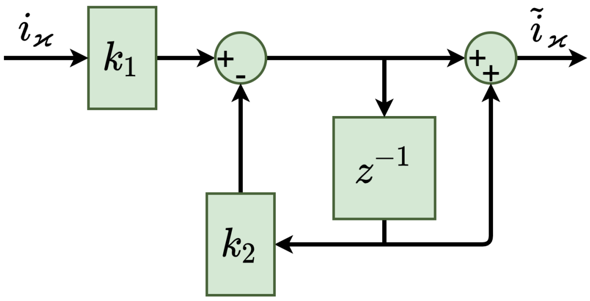

Figure 3.21: *The system diagram of current filter.*

are listed in Table 3.6. It should be noted that the low pass filter is only employed before the fault detectors, whereas the current controllers, which are introduced in section A.3, still use unfiltered current feedback. Additionally,

Table 3.6: Parameters of the Butterworth IIR low pass filter

Variate	Value
Sample frequency	20000Hz
Cutting frequency	1000Hz
k_1	0.13672873599731955
k_2	-0.72654252800536101

the low pass filter leads to a small delay. Hence, the current reference is also filtered by the same filter described above so that the reference and feedback of the current have the same delay. It is worth highlighting that a significant delay will make the detector fail to report the fault. The performance of the proposed low pass filter are detailed in section 3.6.3.

The fault detector block receives as input the feedback and reference currents to perform an on-line monitoring of the drive health condition. This block reports the faults to the reference current calculation block by a fault code consisting of three numbers, jkz. The first number j, the second number k and the third number z are states of sector 1, 2, and 3, respectively. The value of each number, 0, 1 ,2, 4, and 7, stands for healthy condition, phase u, v, w SPOC fault condition, and TPOC fault condition, respectively. Table 3.7 lists some fault codes for open-circuit faults in different locations. A schematic representation of the reference current calculation block is shown in Figure 3.20 b). A switch will select the appropriate path for the force and torque references based on the fault code therefore having the reference currents computed accordingly.

Table 3.7: Fault code for different fault location

Open-circuit fault location	**Sector 1**	**Sector 2**	**Sector 3**	**Sector 1 & 2**
Healthy	000	000	000	000
Phase U	100	010	001	110
Phase V	200	020	002	220
Phase W	400	040	004	440
Three-phase	700	070	007	None

3.6.2 Description of the experimental set-up

The experimental set-up is presented in this sub-section. The stator of the proposed bearingless PMSM is displayed in Figure 3.22. It is clearly observed that three three-phase windings are galvanically isolated. Figure 3.23 shows

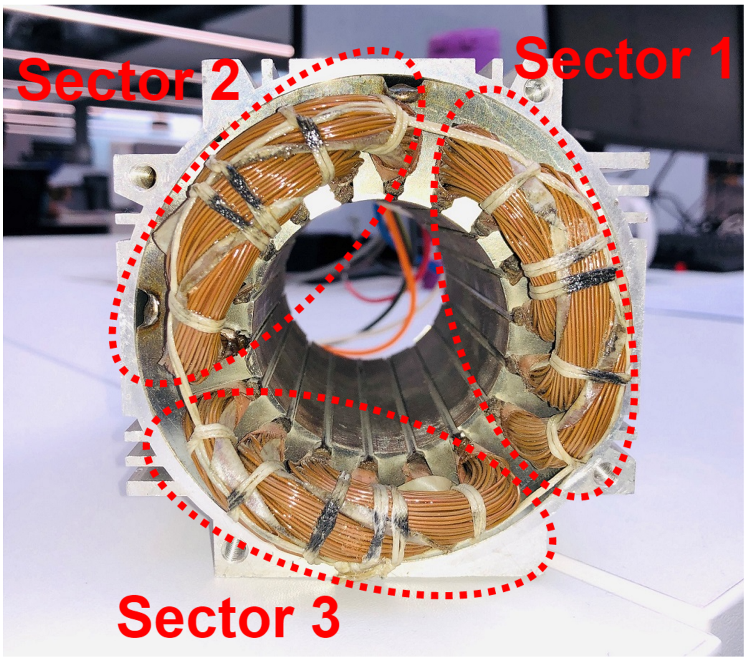

Figure 3.22: *The stator of the BM.*

the instrumented test rig. The BM and the load motor are connected through an universal joint. At the non-drive-end of the BM, a self-alignment bearing avoids the axial and $x - y$ displacement of the shaft. The two degrees

a)

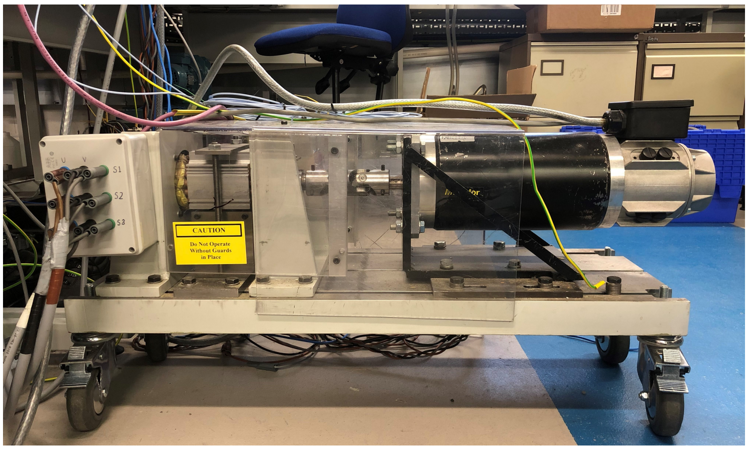

b)

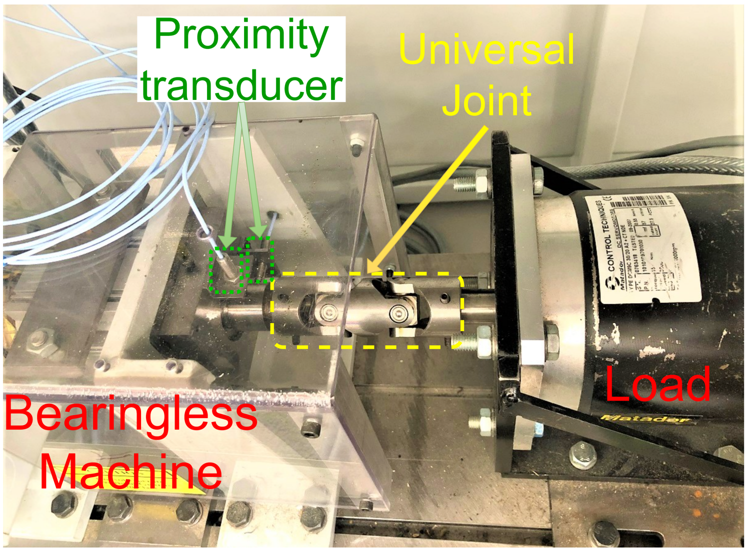

Figure 3.23: *Experimental rig. a) The BM and the load machine. b) The universal joint and the proximity transducers.*

of the freedom of the shaft is allowed at the drive-end but it is limited by a backup bearing with a clearance of $150\mu m$. The rotor radial $x - y$ positions are measured via two 3300 XL NSv proximity transducers based on eddy current sensing technology, as shown in Figure 3.24. The main parameters of the proximity transducers are 10kHz bandwidth, a linear range from 0.25 to 1.75 mm and an Incremental Scale Factor of 7.87V/mm. The offset is cancelled in the DSP. A solid cylinder of AISI 4140 is mounted on the shaft to

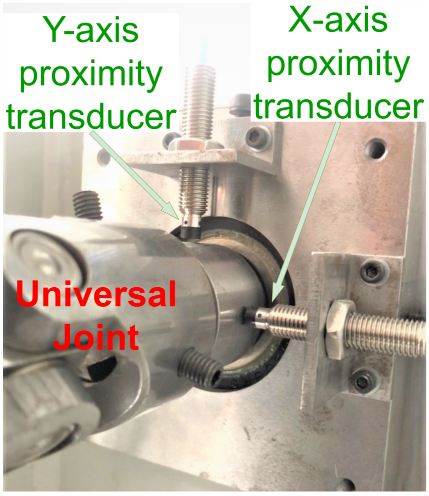

Figure 3.24: *Proximity transducers in x and y axes.*

maximise the measurement performance, being the sensor calibrated in the factory for acting on this material. Each sector of the BM is supplied by a 2 kW three-phase power inverter, as shown in Figure 3.25. The inverters are

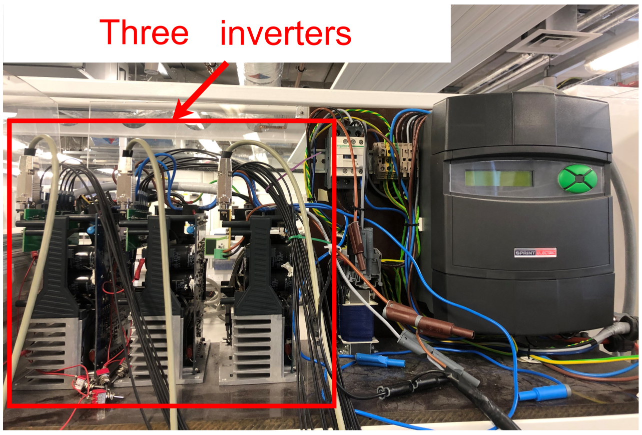

Figure 3.25: *Three inverters.*

SPWM modulated, and the voltage references are obtained from conventional PI current controllers. The power inverters (PS21A79) are manufactured by Mitsubishi Semiconductor, and their switching frequency is set to 10 kHz.

The custom-made control board (*uCube*) is based on the Microzed Xilinx Zynq-7000 All Programmable SoC from Avnet [90], as shown in Figure 3.26. The sample time of the control board is 50 μs. The communication between inverters and the control board is realized by means of fibre optic cables.

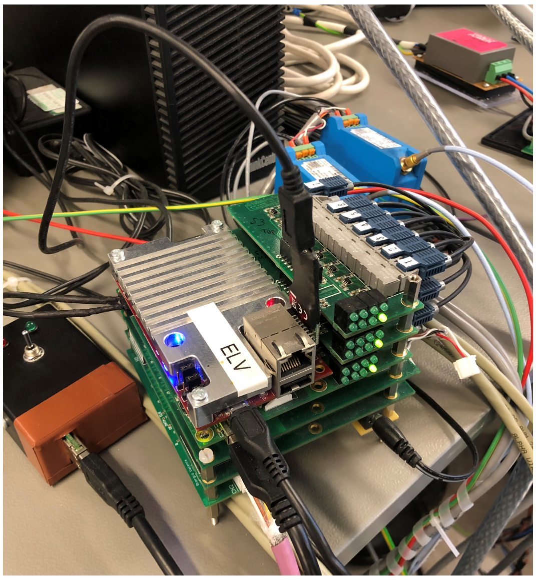

Figure 3.26: *Control board*

3.6.3 Experimental results

A "switching off" command is created at software level in the control board so that each leg of three inverters can be disabled. The experimental validations are completed in three steps, listed as follows:

- First, the proposed BM operates with a 2 Nm load rotating at 3000rpm in the healthy condition. The step verifies that the proposed algorithm can handle the machine realizing the levitation while being coupled to a load.

- The second step validates the TPOC and SPOC fault-tolerant controls at the steady state. The randomly selected phases are disabled while the machine operates at 3000rpm with a 2 Nm load. This step is designed to test the performance of proposed fault-tolerant control approaches.

- The third step tests the control effects during the speed transient. Two experimental tests have been performed to validate both the TPOC and SPOC fault operating conditions.

3.6.3.1 Experimental test results in the healthy condition

The experimental tests are performed at steady state at nominal speed of 3000 rpm with a 2 Nm load. 0.1 second results are recorded, as shown in Figure 3.27, Figure 3.28, Figure 3.29, and Figure 3.30.

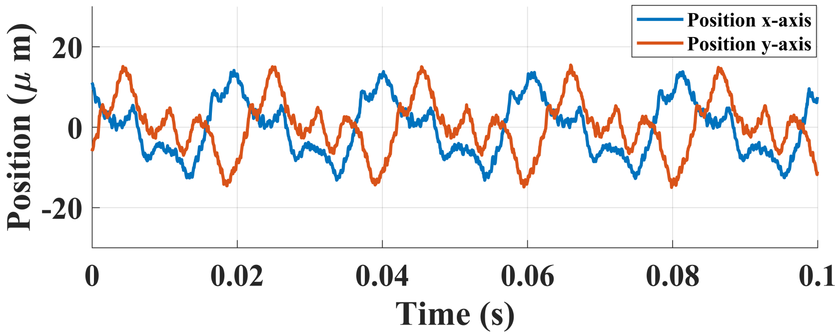

Figure 3.27: *Rotor radial position of the experimental test for the proposed BM in the healthy condition. The position is decomposed into two directions, x- and y-axis.*

Figure 3.27 displays the rotor radial position which is measured in two directions, x- and y- axis. The rotor displacement is within 20 μm during the test, which is much smaller than the clearance of the backup bearing, 150 μm.

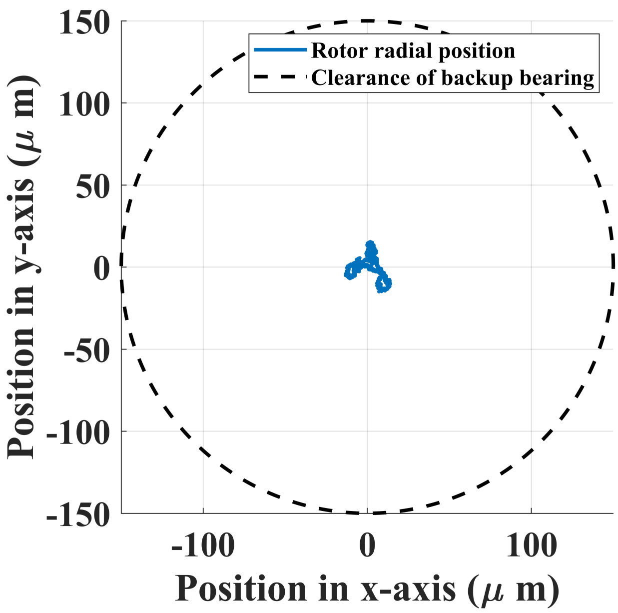

Figure 3.28: *Rotor radial position of the experimental test for the proposed BM in the healthy condition, displayed in the Cartesian coordinate system. The blue line shows the rotor position trajectory.*

In order to clearly show the control performance of the levitation system, the rotor radial position trajectory is displayed in Figure 3.28. It is important to highlight that the rotor position remains limited in a small neighbourhood of the centre of the rotor/stator geometrical centre.

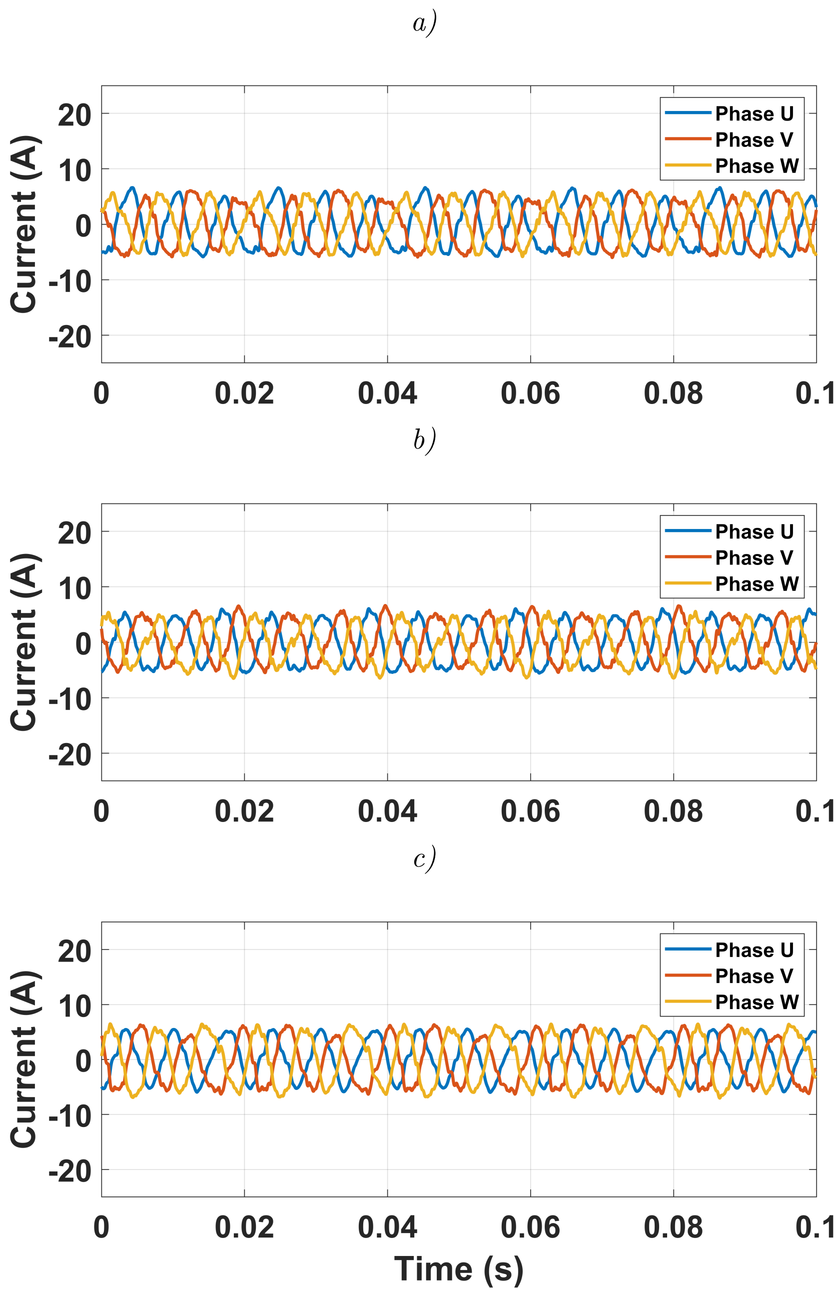

Figure 3.29: *Experimental results in the healthy condition, three-phase currents of three sectors. a) Three-phase current of sector 1. b) Three-phase current of sector 2. c) Three-phase current of sector 3.*

Figure 3.29 and Figure 3.30 show the three-phase currents and the d-q axis currents of three sectors, respectively. It is noted that the three-phase currents are not as smooth as for the conventional three-phase machine, since the d-axis currents are not 0 when the suspension force is generated, displayed in

Figure 3.30.

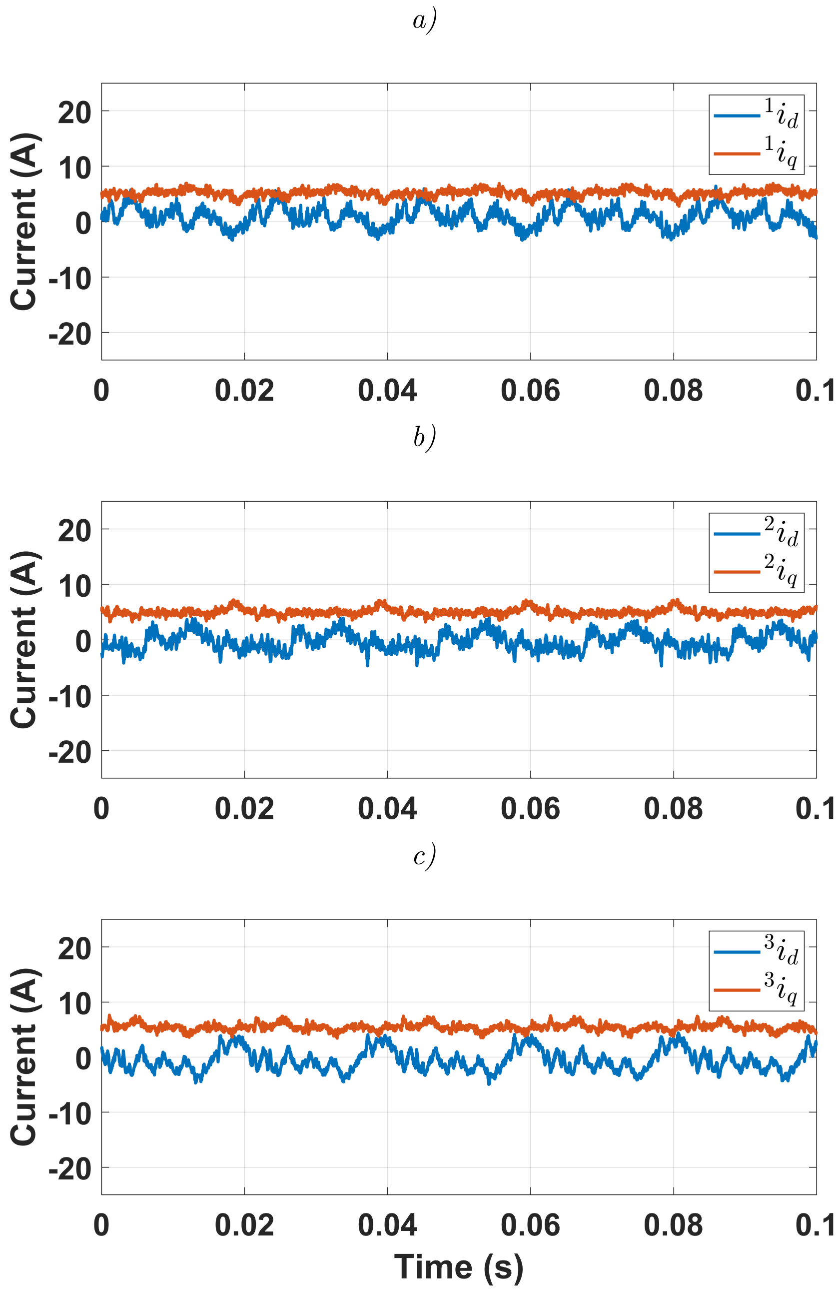

Figure 3.30: *Experimental results in the healthy condition, d-q axis currents of three sectors. a) d- and q- axis currents of sector 1. b) d- and q- axis currents of sector 2. c) d- and q- axis currents of sector 3.*

Furthermore, it is worth highlighting that the proposed control approach considers the coupling between the d-axis current and the q-axis current as described in the section where the control algorithm is presented. Hence, the q-axis currents, which contribute to both the controllable suspension force and torque generation, contain high order harmonics, as displayed in Figure 3.30. Additionally, based on the measured three-phase currents during the experiments, with a $0.08 Ohm$ resistance, the copper loss is computed, $11.16W$.

3.6.3.2 Experimental test results in the faulty conditions

Two experimental tests are implemented to address the performance in faulty conditions. Firstly, the MS-PMSM transits from a healthy condition to the sector 1 TPOC fault condition. In the second one, the machine transits from a healthy condition to the phase u_1 and v_2 SPOC faults condition. The experimental tests are performed at steady state nominal speed of 3000 rpm with a 2 Nm load.

Figure 3.32, Figure 3.31, and Figure 3.33 show the state of the fault signal, the phase currents of the three sectors, and the $x - y$ axis position of the rotor, respectively. For the first 20 ms the drive is healthy, and then the inverter connected to sector 1 is disabled. This can be observed from the three-phase currents of sector 1 in Figure 3.31 a) dropping to zero. As Figure 3.32 shown, the fault detector takes $4\,ms$ to detect the fault of sector 1 while the fault signals of the two remaining healthy sectors remain equal to zero, so the fault code is 700. The detection time is not long enough to cause a rotor touch with the backup bearing, though the current filters installed in the fault detectors introduce a phase angle delay of the current. From Figure 3.33, it is observed that the rotor $x - y$ position is stable during the experiment, even after one inverter was disabled. Only a small increment of the position ripple can be detected during the transition, before the control algorithm has switched from healthy to faulty mode. Indeed, the maximum displacement is 21 μm during the transition and 15 μm during the rest of the test while the maximum displacement allowed given by the backup bearing is 150 μm.

The TPOC fault causes a lack of contribution to the suspension force and torque generation from sector 1. Meanwhile, the operating conditions (load torque and rotational speed) are controlled to remain during the experimental tests of the healthy and faulty operations. Therefore, sector 2 and sector 3 generate higher currents to compensate for the lost contribution of sector 1.

a)

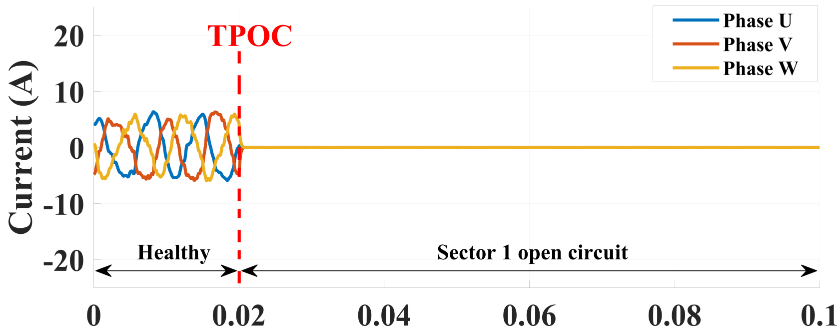

b)

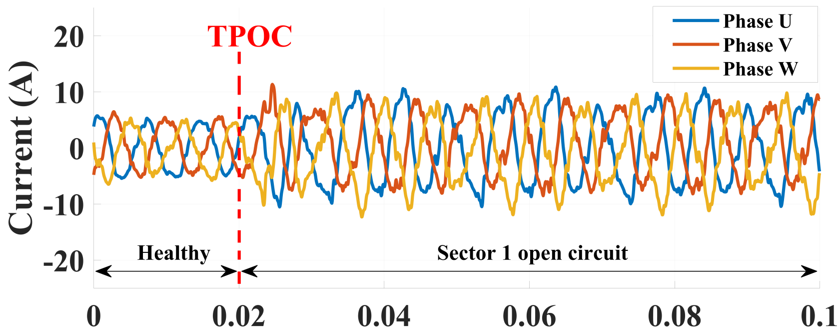

c)

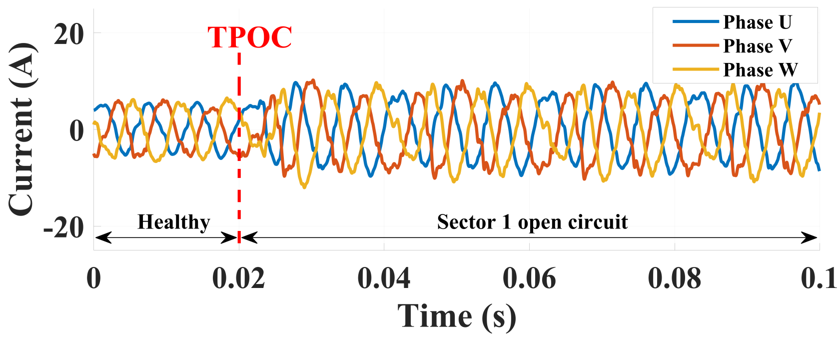

Figure 3.31: *Experimental test results for the TPOC condition: the phase current feedback from power inverters. a) Sector 1; b) Sector 2; c) Sector 3.*

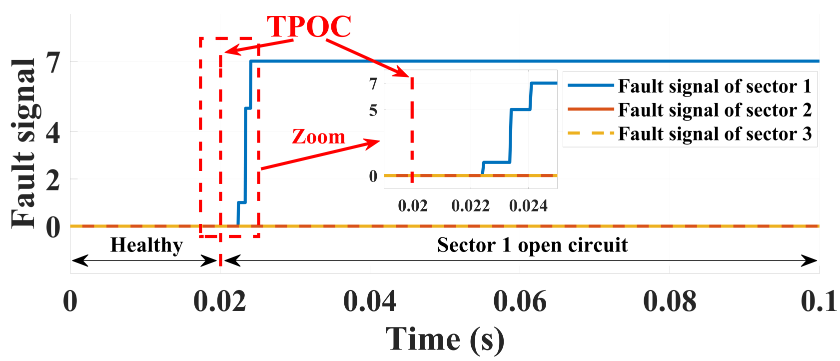

Figure 3.32: *Experimental test results for the TPOC condition: fault signals from fault detector. Fault code is displayed by three separated lines.*

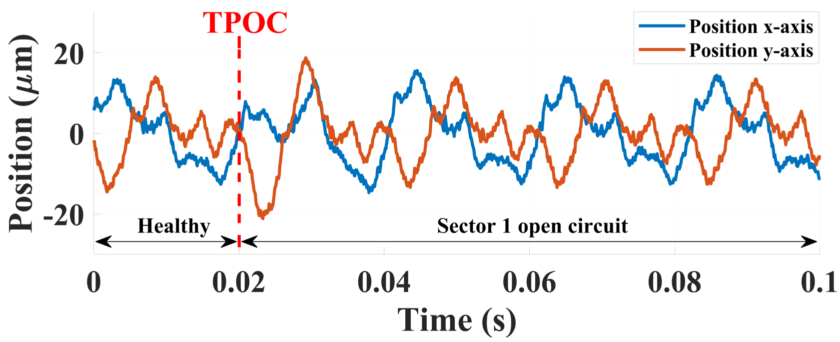

Figure 3.33: *Experimental test results for the TPOC condition: the position feedback in x-axis and y-axis.*

Table 3.8 lists RMS values for each phase current of sector 2 and sector 3. It is observed that the RMS values increase by 35.5%-68.4% in the TPOC fault considered. Meanwhile, the copper loss increases from 11.16W to 17.37W from the healthy condition to the faulty condition.

Table 3.8: The RMS values of the phase currents in the healthy condition and the TPOC faulty condition.

Sector	Phase	Healthy (A)	Faulty (A)	Increased (%)
2	u	3.79	6.16	62.8
2	v	3.63	5.44	50.0
2	w	3.56	5.99	68.4
3	u	3.69	5.88	59.0
3	v	3.93	5.95	51.6
3	w	4.34	5.87	35.5

Concerning the second experimental test, Figure 3.35, Figure 3.34, and Figure 3.36 show the state of the fault signal, the phase currents of the three sectors, and the $x - y$ axis position of the rotor, respectively. The drive is healthy for the first 20 ms and then the legs corresponding to phase u of sector 1 and phase v of sector 2 are disabled having the relative currents drop to zero as can be observed in Figure 3.34 a) and b). After 3.5 ms the fault detector reports the correct fault and the control algorithm switches from healthy to the corresponding faulty mode as shown in Figure 3.35. It can be observed that the rotor $x - y$ axis position keeps stable during test time even when SPOC happens, as shown in Figure 3.36.

In the SPOC faulty condition, the current amplitudes of the remaining healthy

a)

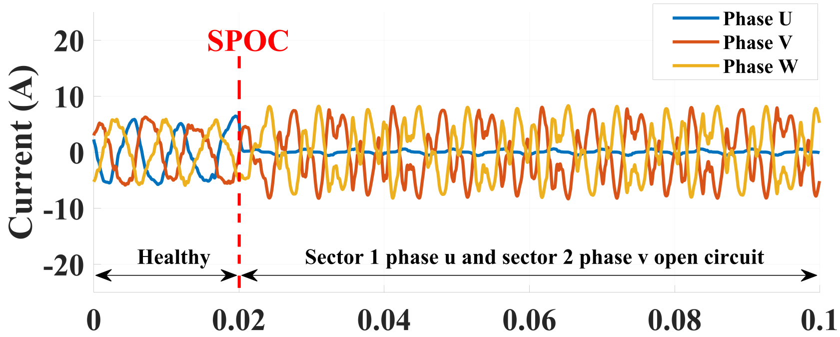

b)

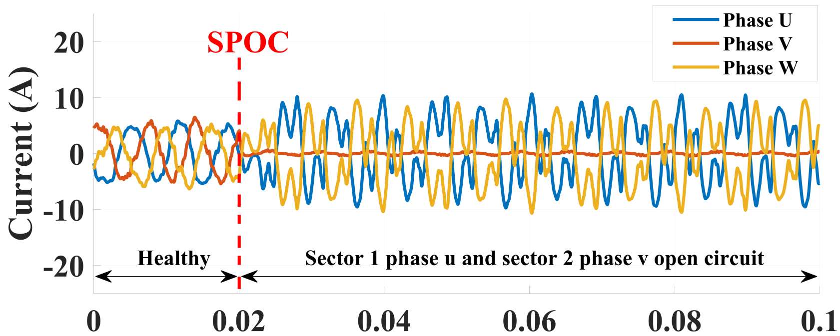

c)

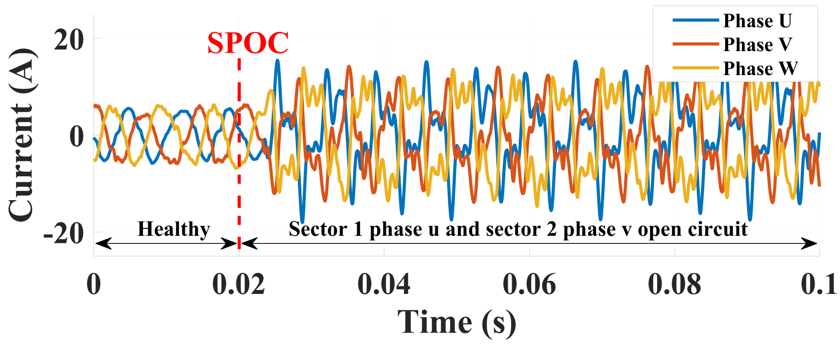

Figure 3.34: *Experimental test results for the SPOC condition: the phase current feedback from power inverters. a) Sector 1; b) Sector 2; c) Sector 3.*

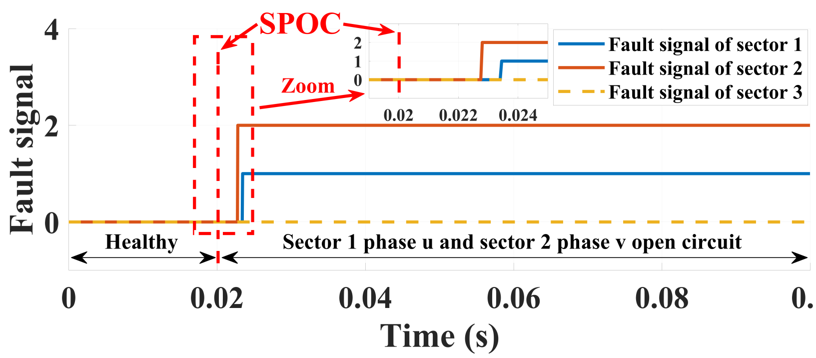

Figure 3.35: *Experimental test results for the SPOC condition: fault signals from fault detector. Fault code is displayed by three separated lines.*

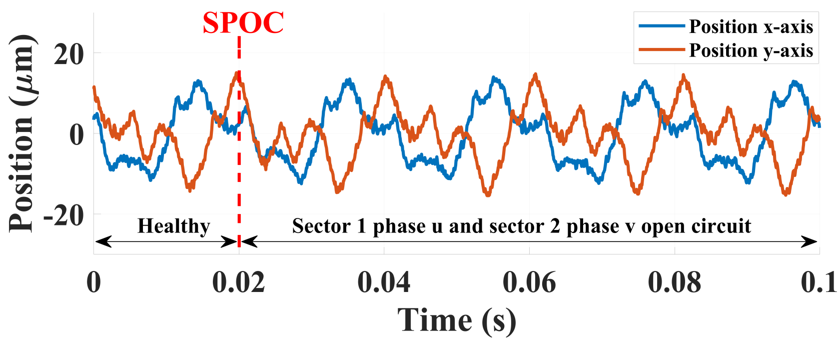

Figure 3.36: *Experimental test results for the SPOC condition: the position feedback in x-axis and y-axis.*

phases increase after the fault has occurred in order to compensate for the lack of forces and torque generated by the faulty phases. Table 3.9 lists the RMS values of the phase currents. Meanwhile, the copper loss increases from 11.16W to 23.19W from the healthy condition to the faulty condition.

Table 3.9: The RMS values of the phase currents in the healthy condition and the SPOC faulty condition.

Sector	Phase	Healthy (A)	Faulty (A)	Increased (%)
1	v	4.03	4.57	13.2
1	w	3.66	4.50	23.1
2	u	3.84	5.52	43.8
2	w	3.50	5.44	55.5
3	u	3.68	7.20	95.9
3	v	3.98	6.74	69.4
3	w	4.27	8.06	88.7

In both TPOC and SPOC fault conditions, it is observed that the harmonic content of the phase current for a SPOC fault in two sectors is higher than that for a TPOC fault in one sector. Figure 3.37 displays the harmonic spectra of the phase currents of sector 3 for healthy, TPOC fault, and SPOC fault operating conditions. The phase currents for the SPOC fault contain significant 3^{rd} and 5^{th} order harmonics which are predicted from the force coefficient in Figure 3.10, whereas it is possible to observe that the main harmonic contribution of the phase currents for healthy and TPOC fault conditions is the 1^{st} order as expected from the results presented in Figure 3.10.

In both experimental tests, the output torque of the machine remains constant

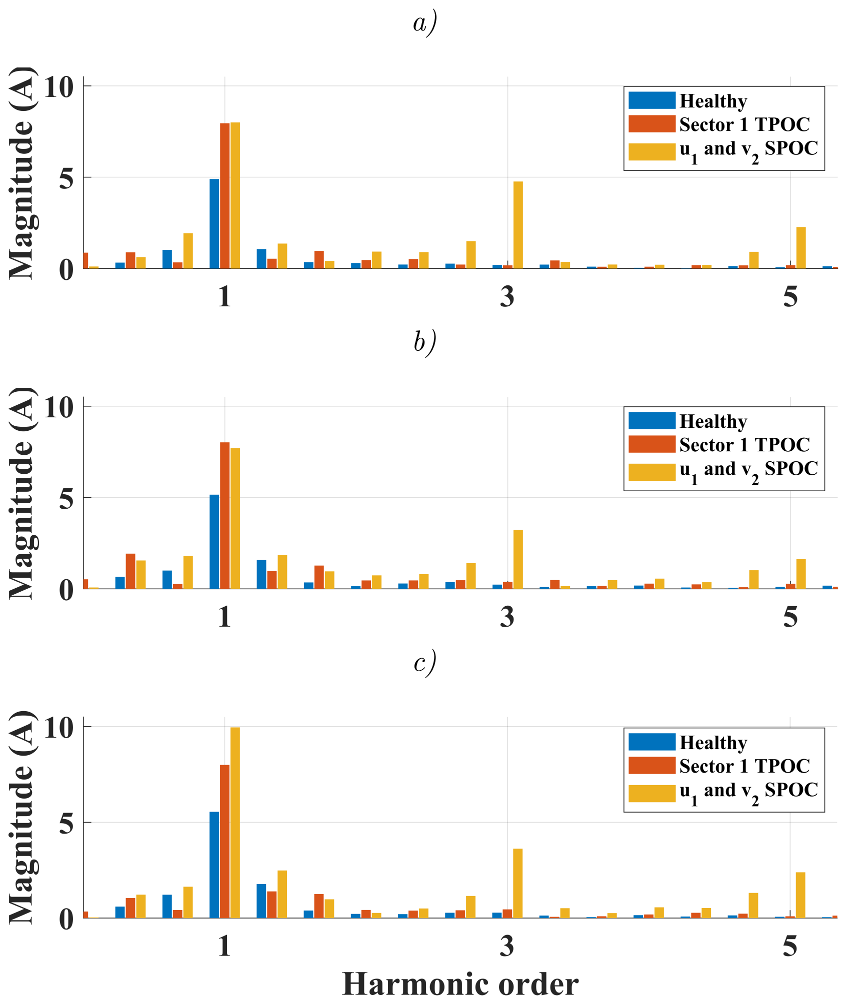

Figure 3.37: *Sector 3 phase currents harmonic spectra of healthy, TPOC, and SPOC conditions. a) Phase u. b) Phase v. c) Phase w.*

to the value of 2 Nm also during faulty conditions. Hence, there are no thermal restrictions, and the machine can operate continuously. Indeed, the tests are performed with a 2 Nm load, while the rated machine torque is 5 Nm. If the machine has to deliver its rated torque, it could only operate for a limited time due to the higher current flowing in the winding under faulty conditions.

Some conclusion can be drawn from the above presented experimental results for the BM operation under TPOC and SPOC fault conditions. The rotor position remains stable in all the performed tests, validating the suspension force and torque control strategy. The phase current waveforms are analysed by Fast Fourier transform to verify the prediction presented in section 3.4.3.

3.6.3.3 Experimental test results in the speed transient

This experimental test verifies the dynamic performance of the proposed control strategies. 4 seconds of experimental results are recorded, and the test is performed following procedure described below:

- The rotor is levitated before 0s, as shown in Figure 3.40.
- The machine accelerates from 0 rpm to 3000 rpm, starting at 0.2s, as displayed in Figure 3.38.
- At 2s, the sector 1 phase u open-circuit fault happens, so the corresponding current drops to zero, as shown in Figure 3.41 a).
- The fault detector takes approximate 3 ms on detecting the fault, as displayed in Figure 3.39. Then, the control strategy switches to the faulty mode.
- The rotational speed of the machine reaches 3000 rpm at 3.8s.

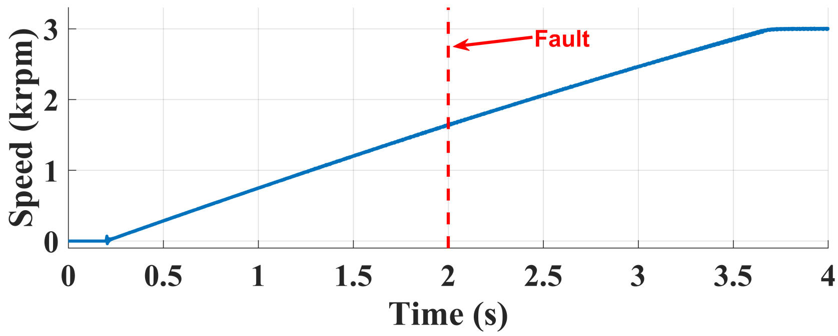

Figure 3.38: *Experimental results: speed transient. Sector 1 phase u open-circuit fault happens at 2s, and the output torque is limited at 2 Nm.*

Since the open-circuit happens during the speed transient, the torque output is limited at 2 Nm during the test, which is the torque limit achievable under fault conditions to avoid overload currents. Indeed, even in a healthy condition, the torque output cannot reach its rated value because the phase current provides the suspension force and torque simultaneously. This negatively affects the angular acceleration of the machine. The problem will be addressed and tackled in the next chapter.

It is observed that the fault detector takes 3 ms detecting the open-circuit fault. The machine condition and the control strategy are mismatched during the detection time, but this does not cause an increment in the rotor displacement, as shown in Figure 3.40. In contrast, the increase of the rotational speed leads to an increase in the rotor displacement, such displacement does not show an significant increases after 1500 rpm.

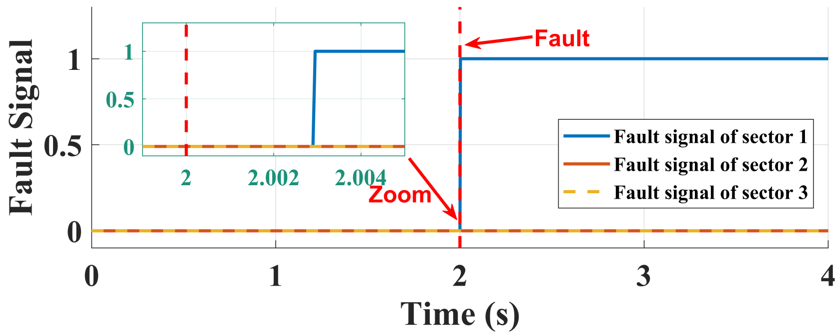

Figure 3.39: *Experimental result during the speed transient: fault detector signals which are displayed by three lines.*

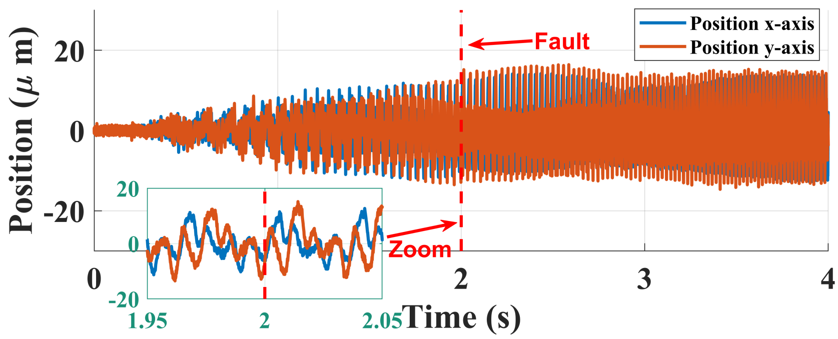

Figure 3.40: *Experimental results during the speed transient: rotor radial position. Sector 1 phase u open-circuit fault happened at 2s.*

The lack of sector 1 phase u leads the corresponding d-q axis currents to contain a huge significant order harmonic content (Figure 3.42 a)). From Figure 3.41 b) and c), it can be found that high order harmonics appear in the phase current after SPOC fault, which is predicted in Figure 3.10. Meanwhile, the high order harmonics contained in d-q currents of healthy sectors also increase after SPOC fault, as displayed in Figure 3.42 b) and c).

The sub-section presents the experimental validation during the speed transient checking the performance of the SPOC fault control strategy. The results

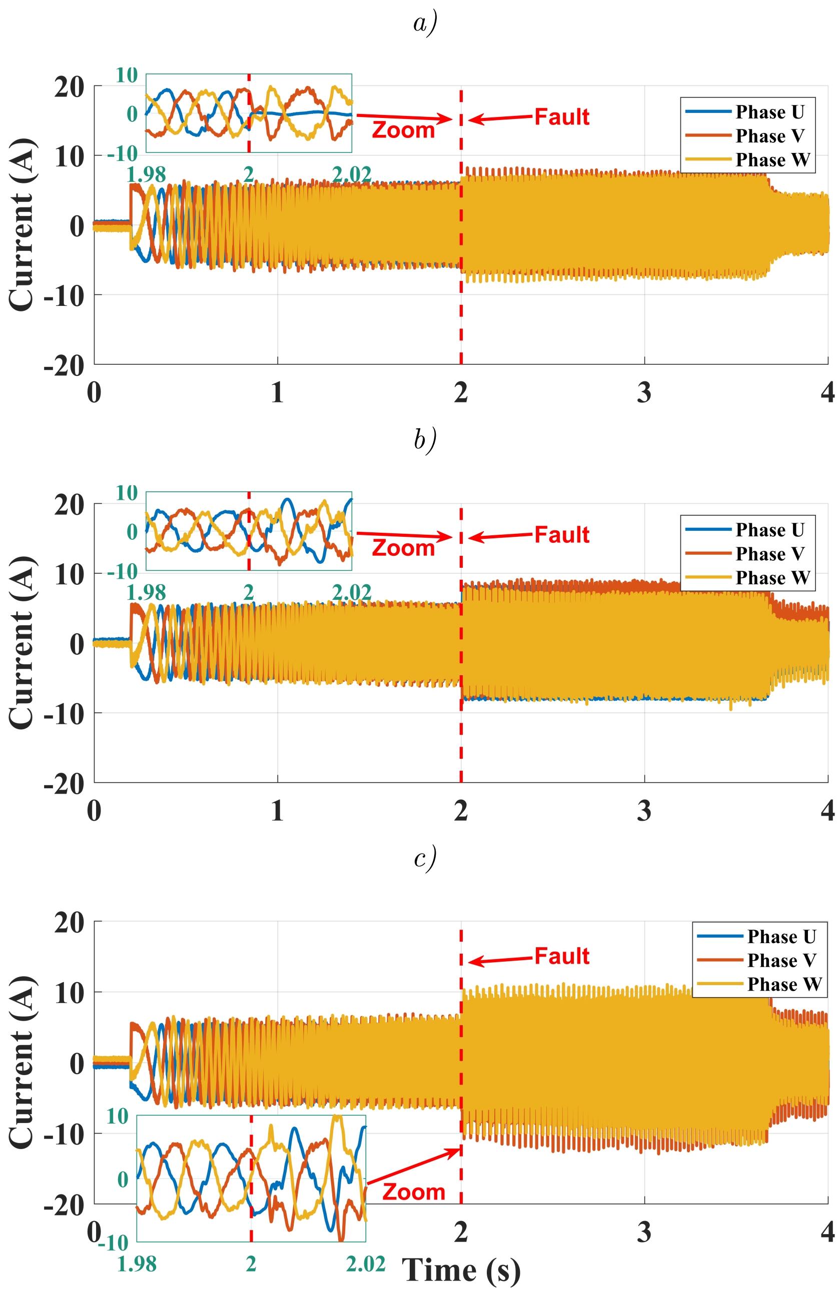

Figure 3.41: *Experimental results during the speed transient: three-phase currents. Sector 1 phase u open-circuit fault happened at 2s. a) sector 1. b) sector 2. c) sector 3.*

show that the proposed approach could implement the rotor levitation and achieve stable control performances. Even if the SPOC fault happens during the rotor angular acceleration, the fault does not strongly affect the rotor levitation.

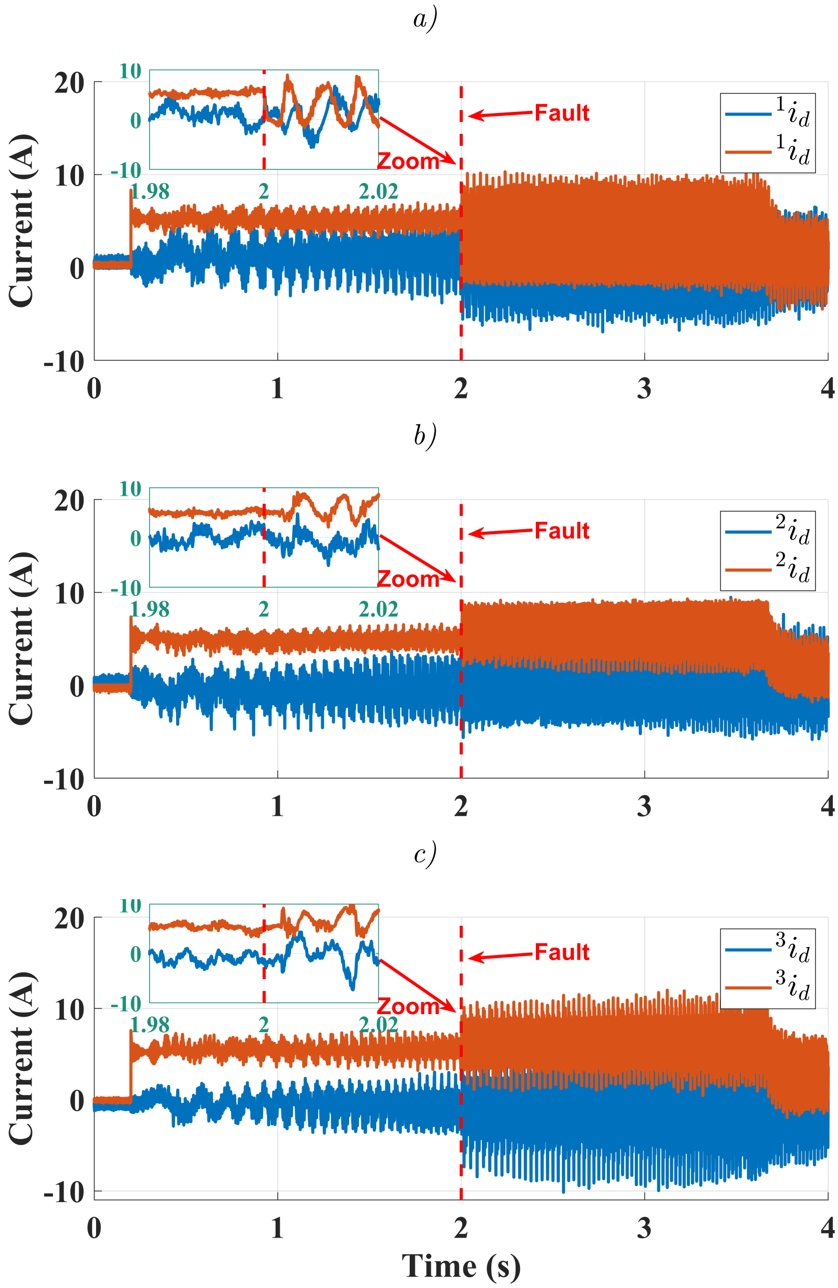

Figure 3.42: *Experimental result during the speed transient: d-q axis currents. Sector 1 phase u open-circuit fault happened at 2s. a) sector 1. b) sector 2. c) sector 3.*

3.7 Conclusion

The Chapter firstly proposes the machine's structure and the voltage equation. Then, a suspension force and torque generation principle is presented. Based on the healthy model, a control method for TPOC fault condition and a control strategy for SPOC fault in one or two sectors are developed. A fault detector is also designed in order to replicate the real control scenarios. The control theory is verified by FEA and experimental tests. The FEA simulations show that the proposed fault-tolerant control algorithm can generate the desired suspension forces and torque. Furthermore, the FEA results also highlight the importance of an accurate estimation of the force and torque coefficients to guarantee good performances during an open-circuit fault. The experimental test has verified the performance of the BM control system including the force control algorithm in healthy and faulty conditions.

However, the section also exposes the disadvantage of the proposed techniques, that the output torque is limited to lower than the rated value during the faulty conditions. Therefore, a smart current limitation technique will be presented in the next chapter showing the solution that exploits the maximum capabilities of the MS PMSM.

Chapter 4

A Novel Current Limitation Technique Exploiting the Maximum Capability of Power Electronic Inverters and Bearingless Machines

4.1 Introduction

As mentioned in section 3.7, the fault tolerance technique allows the operation of the MS BM in open-circuit fault conditions, but the technique cannot achieve the rated torque output during the faulty operating conditions to avoid the machine reaching its thermal limitation. In order to maintain the maximum performance of the machine, this chapter presents an algorithm that can exploit the maximum capability of the proposed MS BM in healthy and faulty conditions. In other words, the algorithm attempts to exploit the suspension force and torque as much as possible while the technique guarantees the current does not exceed the physical limits of the power inverters and the machine.

In a general drive system, both machine and power electronics have an intrinsic current limit. If this limit is exceeded for an extended duration, permanent damages can occur. A standard and simple method to avoid the problem is limiting the inverter current reference. However, in sectored multiphase BMs, the relations between phase currents, torque, and forces are complex: saturating the phase currents could result in uncontrolled torque and forces, which, in turn, can lead to a rotor touchdown. An alternative approach is to limit force references and torque reference separately in order to fulfil the maximum currents limit. This technique limits the system performances as the maximum current capability is exploited only when rated torque and forces are simultaneously required. Furthermore, maximum torque and forces must be further reduced in faulty conditions, thus requiring a more advanced scheme to handle current saturation. The work proposed in this chapter is built upon [91], presenting a more detailed theoretical analysis, in particular in the presence of TPOC and SPOC faults. The model of suspension force and torque generation in case of TPOC and SPOC faults is introduced in the direct-quadrature domain in order to reduce torque ripple during current saturation. Both these standard current saturation methods are tested against the proposed method in order to show the advantages of the latter. Drive systems reliability requirements depend on the application. However, especially when BMs are operated at high speed, shaft touchdown could lead to catastrophic system failure. Therefore, in this chapter, the novel suspension force and torque control strategy prioritizes suspension force production at the expense of torque generation in order to guarantee rotor suspension.

The proposed approach is tested and compared against traditional current saturation techniques both in simulation and experiments using the prototype MS PMSM.

4.2 Coordinate transformation

In section 3.4.2, the pseudo-inverse matrix $\mathbf{K}^{+}_{\mathrm{uvw}}(\vartheta_{\mathrm{e}})$ is written in the three-phase reference frame. To achieve the smooth force and torque limitations, the matrix can be transformed to the direct-quadrature reference frame, presented in detail in the following steps:

- Split the matrix $\mathbf{K}^{+}_{\mathrm{uvw}}(\vartheta_{\mathrm{e}})$ into three sub-matrices:

$$\mathbf{K}^{+}_{\mathrm{uvw}}(\vartheta_{\mathrm{e}}) = \begin{bmatrix} {}^{1}\mathbf{K}^{+}_{\mathrm{uvw}}(\vartheta_{\mathrm{e}}) \\ {}^{2}\mathbf{K}^{+}_{\mathrm{uvw}}(\vartheta_{\mathrm{e}}) \\ {}^{3}\mathbf{K}^{+}_{\mathrm{uvw}}(\vartheta_{\mathrm{e}}) \end{bmatrix} \tag{4.1}$$

  where

$$\begin{aligned}
{}^{1}\mathbf{K}^{+}_{\mathrm{uvw}}(\vartheta_{\mathrm{e}}) &= \begin{bmatrix} {}^{1}k^{+}_{x\mathrm{u}}(\vartheta_{\mathrm{e}}) & {}^{1}k^{+}_{y\mathrm{u}}(\vartheta_{\mathrm{e}}) & {}^{1}k^{+}_{T\mathrm{u}}(\vartheta_{\mathrm{e}}) \\ {}^{1}k^{+}_{x\mathrm{v}}(\vartheta_{\mathrm{e}}) & {}^{1}k^{+}_{y\mathrm{v}}(\vartheta_{\mathrm{e}}) & {}^{1}k^{+}_{T\mathrm{v}}(\vartheta_{\mathrm{e}}) \\ {}^{1}k^{+}_{x\mathrm{w}}(\vartheta_{\mathrm{e}}) & {}^{1}k^{+}_{y\mathrm{w}}(\vartheta_{\mathrm{e}}) & {}^{1}k^{+}_{T\mathrm{w}}(\vartheta_{\mathrm{e}}) \end{bmatrix} \\
{}^{2}\mathbf{K}^{+}_{\mathrm{uvw}}(\vartheta_{\mathrm{e}}) &= \begin{bmatrix} {}^{2}k^{+}_{x\mathrm{u}}(\vartheta_{\mathrm{e}}) & {}^{2}k^{+}_{y\mathrm{u}}(\vartheta_{\mathrm{e}}) & {}^{2}k^{+}_{T\mathrm{u}}(\vartheta_{\mathrm{e}}) \\ {}^{2}k^{+}_{x\mathrm{v}}(\vartheta_{\mathrm{e}}) & {}^{2}k^{+}_{y\mathrm{v}}(\vartheta_{\mathrm{e}}) & {}^{2}k^{+}_{T\mathrm{v}}(\vartheta_{\mathrm{e}}) \\ {}^{2}k^{+}_{x\mathrm{w}}(\vartheta_{\mathrm{e}}) & {}^{2}k^{+}_{y\mathrm{w}}(\vartheta_{\mathrm{e}}) & {}^{2}k^{+}_{T\mathrm{w}}(\vartheta_{\mathrm{e}}) \end{bmatrix} \\
{}^{3}\mathbf{K}^{+}_{\mathrm{uvw}}(\vartheta_{\mathrm{e}}) &= \begin{bmatrix} {}^{3}k^{+}_{x\mathrm{u}}(\vartheta_{\mathrm{e}}) & {}^{3}k^{+}_{y\mathrm{u}}(\vartheta_{\mathrm{e}}) & {}^{3}k^{+}_{T\mathrm{u}}(\vartheta_{\mathrm{e}}) \\ {}^{3}k^{+}_{x\mathrm{v}}(\vartheta_{\mathrm{e}}) & {}^{3}k^{+}_{y\mathrm{v}}(\vartheta_{\mathrm{e}}) & {}^{3}k^{+}_{T\mathrm{v}}(\vartheta_{\mathrm{e}}) \\ {}^{3}k^{+}_{x\mathrm{w}}(\vartheta_{\mathrm{e}}) & {}^{3}k^{+}_{y\mathrm{w}}(\vartheta_{\mathrm{e}}) & {}^{3}k^{+}_{T\mathrm{w}}(\vartheta_{\mathrm{e}}) \end{bmatrix}.
\end{aligned} \tag{4.2}$$

- Each sub-matrix ${}^{s}\mathbf{K}^{+}_{\mathrm{uvw}}(\vartheta_{\mathrm{e}})$ can be transformed to DQZ reference frame by applying the Park transformation matrix $\mathbf{T}_{\mathrm{Pk}}(\vartheta_{\mathrm{e}})$ where the Z-component is neglected, as presented in (4.3):

$${}^{s}\mathbf{K}^{+}_{\mathrm{dq}}(\vartheta_{\mathrm{e}}) = \mathbf{T}_{\mathrm{Pk}}(\vartheta_{\mathrm{e}})\,{}^{s}\mathbf{K}^{+}_{\mathrm{uvw}}(\vartheta_{\mathrm{e}}) = \begin{bmatrix} {}^{s}k^{+}_{x\mathrm{d}}(\vartheta_{\mathrm{e}}) & {}^{s}k^{+}_{y\mathrm{d}}(\vartheta_{\mathrm{e}}) & {}^{s}k^{+}_{T\mathrm{d}}(\vartheta_{\mathrm{e}}) \\ {}^{s}k^{+}_{x\mathrm{q}}(\vartheta_{\mathrm{e}}) & {}^{s}k^{+}_{y\mathrm{q}}(\vartheta_{\mathrm{e}}) & {}^{s}k^{+}_{T\mathrm{q}}(\vartheta_{\mathrm{e}}) \end{bmatrix} \tag{4.3}$$

where

$$\mathbf{T}_{\mathrm{Pk}}(\vartheta_{\mathrm{e}}) = \frac{2}{3}\begin{bmatrix} \cos(\vartheta_{\mathrm{e}}) & \cos(\vartheta_{\mathrm{e}} - \frac{2\pi}{3}) & \cos(\vartheta_{\mathrm{e}} + \frac{2\pi}{3}) \\ -\sin(\vartheta_{\mathrm{e}}) & -\sin(\vartheta_{\mathrm{e}} - \frac{2\pi}{3}) & -\sin(\vartheta_{\mathrm{e}} + \frac{2\pi}{3}) \end{bmatrix}. \tag{4.4}$$

- Finally, the inverted wrench-current coefficient matrix in the direct-quadrature reference frame consists of all sub-matrix, expressed in the follow:

$$\mathbf{K}^{+}_{\mathrm{dq}}(\vartheta_{\mathrm{e}}) = \begin{bmatrix} {}^{1}\mathbf{K}^{+}_{\mathrm{dq}}(\vartheta_{\mathrm{e}}) \\ {}^{2}\mathbf{K}^{+}_{\mathrm{dq}}(\vartheta_{\mathrm{e}}) \\ {}^{3}\mathbf{K}^{+}_{\mathrm{dq}}(\vartheta_{\mathrm{e}}) \end{bmatrix}. \tag{4.5}$$

Similar to the representation introduced in (4.3), the inverse of the coefficient matrix can be written in different reference frames by applying the Park transformation or the Clarke transformation.

4.3 Force limitation

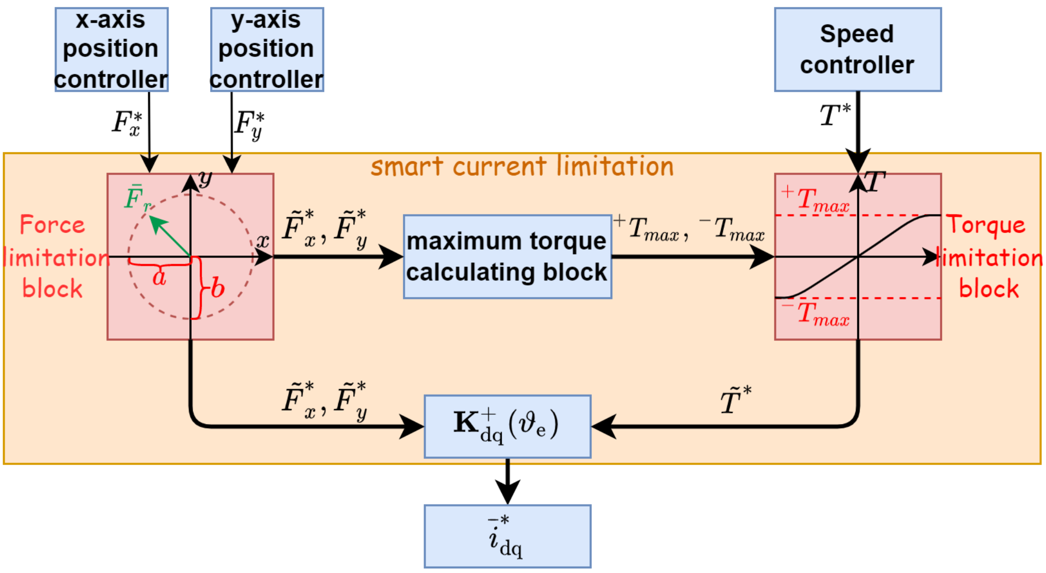

Figure 4.1: *Flow chart of the smart current limitation technique.*

This section presents the force limitation approach of healthy and faulty operating conditions. Figure 4.1 shows the flow chart of the technique. The position controllers output the force references F_x^* and F_y^*, and then the references are limited by a force limitation block. Once the limited force references $\tilde{F}_x^*$ and $\tilde{F}_y^*$ are obtained, the limited force references are applied to calculate the torque limits. Finally, the limited force references and the limited torque reference are used to calculate the stator current references.

4.3.1 Force limitation of the healthy operation

From Figure 4.1, it is clearly observed that the force limitation is required to calculate the torque limitation, therefore the limitation of the suspension force is explored at first.

For the considered machine, $\bar{i}^*_{\mathrm{uvw}} = \mathbf{K}^+_{\mathrm{uvw}}(\vartheta_\mathrm{e})\bar{W}^*$ can be converted to the direct-quadrature reference frame, expressed as

$$\begin{bmatrix} {}^1i_\mathrm{d}^* \\ {}^1i_\mathrm{q}^* \\ {}^2i_\mathrm{d}^* \\ {}^2i_\mathrm{q}^* \\ {}^3i_\mathrm{d}^* \\ {}^3i_\mathrm{q}^* \end{bmatrix} = \begin{bmatrix} {}^1k^+_{x\mathrm{d}}(\vartheta_\mathrm{e}) & {}^1k^+_{y\mathrm{d}}(\vartheta_\mathrm{e}) & {}^1k^+_{T\mathrm{d}}(\vartheta_\mathrm{e}) \\ {}^1k^+_{x\mathrm{q}}(\vartheta_\mathrm{e}) & {}^1k^+_{y\mathrm{q}}(\vartheta_\mathrm{e}) & {}^1k^+_{T\mathrm{q}}(\vartheta_\mathrm{e}) \\ {}^2k^+_{x\mathrm{d}}(\vartheta_\mathrm{e}) & {}^2k^+_{y\mathrm{d}}(\vartheta_\mathrm{e}) & {}^2k^+_{T\mathrm{d}}(\vartheta_\mathrm{e}) \\ {}^2k^+_{x\mathrm{q}}(\vartheta_\mathrm{e}) & {}^2k^+_{y\mathrm{q}}(\vartheta_\mathrm{e}) & {}^2k^+_{T\mathrm{q}}(\vartheta_\mathrm{e}) \\ {}^3k^+_{x\mathrm{d}}(\vartheta_\mathrm{e}) & {}^3k^+_{y\mathrm{d}}(\vartheta_\mathrm{e}) & {}^3k^+_{T\mathrm{d}}(\vartheta_\mathrm{e}) \\ {}^3k^+_{x\mathrm{q}}(\vartheta_\mathrm{e}) & {}^3k^+_{y\mathrm{q}}(\vartheta_\mathrm{e}) & {}^3k^+_{T\mathrm{q}}(\vartheta_\mathrm{e}) \end{bmatrix} \begin{bmatrix} F_x^* \\ F_y^* \\ T^* \end{bmatrix} \tag{4.6}$$

where ${}^sk^+_{\#\varkappa}(\vartheta_\mathrm{e})$ is an element of the matrix $\mathbf{K}^+_{\mathrm{dq}}(\vartheta_\mathrm{e}) \in \mathbb{R}^{6\times 3}$. The subscripts $s \in (1,2,3)$, $\varkappa \in (\mathrm{d},\mathrm{q})$ and $\# \in (x, y, T)$ together determine the position of ${}^sk^+_{\#\varkappa}(\vartheta_\mathrm{e})$ in the matrix $\mathbf{K}^+_{\mathrm{dq}}(\vartheta_\mathrm{e})$. Based on the pseudo-inverse method introduced in section 3.3.2 (minimizing the copper loss), the values of ${}^sk^+_{\#\varkappa}(\vartheta_\mathrm{e})$ are determined by the machine structure and material properties. Therefore, it is observed that the force limitation can be derived by the phase currents.

To achieve the force limitation, the torque reference is assumed to be $0Nm$ in this step. In polar coordinate, force references can be expressed by a force vector and reported in (4.7):

$$
\begin{aligned}
F_x^*(\vartheta_f) &= \left|\bar{F}_r^*\right| \cos(\vartheta_f) \\
F_y^*(\vartheta_f) &= \left|\bar{F}_r^*\right| \sin(\vartheta_f)
\end{aligned}
\tag{4.7}
$$

where $\left|\bar{F}_r^*\right|$ is the force vector magnitude, and ϑ_f is the angle with respect to x-axis. In a fixed rotor electrical position ϑ_e, for the s^{th} sector, $\mathrm{d}-\mathrm{q}$ current references can be calculated as

$$
\begin{aligned}
{}^s i_\mathrm{d}^* &= \left|\bar{F}_r^*\right| \left({}^s k_{x\mathrm{d}}^+(\vartheta_\mathrm{e}) \cos(\vartheta_f) + {}^s k_{y\mathrm{d}}^+(\vartheta_\mathrm{e}) \sin(\vartheta_f) \right) \\
{}^s i_\mathrm{q}^* &= \left|\bar{F}_r^*\right|^* \left({}^s k_{x\mathrm{q}}^+(\vartheta_\mathrm{e}) \cos(\vartheta_f) + {}^s k_{y\mathrm{q}}^+(\vartheta_\mathrm{e}) \sin(\vartheta_f) \right).
\end{aligned}
\tag{4.8}
$$

The current module of sector s can be calculated as

$$
\begin{aligned}
{}^s i_{amp} = \sqrt{{}^s i_\mathrm{d}^{*2} + {}^s i_\mathrm{q}^{*2}} = \\
\sqrt{\begin{aligned}&\left|\bar{F}_r^*\right|^2 \Bigg(\left({}^s k_{x\mathrm{d}}^+(\vartheta_\mathrm{e}) \cos(\vartheta_f) + {}^s k_{y\mathrm{d}}^+(\vartheta_\mathrm{e}) \sin(\vartheta_f) \right)^2 \\ &+ \left({}^s k_{x\mathrm{q}}^+(\vartheta_\mathrm{e}) \cos(\vartheta_f) + {}^s k_{y\mathrm{q}}^+(\vartheta_\mathrm{e}) \sin(\vartheta_f) \right)^2 \Bigg).\end{aligned}}
\end{aligned}
\tag{4.9}
$$

In a fixed rotor electrical position ϑ_e, with the rated current magnitude $\hat{i}_{amp}$, the peak value of the force magnitude of the s^{th} sector $\left(\text{expressed by } {}^s\hat{F}_r(\vartheta_f)\right)$ can be computed from (4.9), resulting in

$$
{}^s\hat{F}_r(\vartheta_f) = \sqrt{\frac{\hat{i}_{amp}^2}{\sigma(\vartheta_f)}}
\tag{4.10}
$$

where

$$
\begin{aligned}
\sigma(\vartheta_f) = &\left({}^s k_{x\mathrm{d}}^+(\vartheta_\mathrm{e}) \cos(\vartheta_f) + {}^s k_{y\mathrm{d}}^+(\vartheta_\mathrm{e}) \sin(\vartheta_f) \right)^2 \\
&+ \left({}^s k_{x\mathrm{q}}^+(\vartheta_\mathrm{e}) \cos(\vartheta_f) + {}^s k_{y\mathrm{q}}^+(\vartheta_\mathrm{e}) \sin(\vartheta_f) \right)^2
\end{aligned}
\tag{4.11}
$$

${}^s\hat{F}_r(\vartheta_f)$ is computed numerically for n values of $\vartheta_f \in [0 \ldots 2\pi]$ resulting in a vector ${}^s\hat{\mathbf{F}}_r(\vartheta_f) \in \mathbb{R}^{1\times n}$. The procedure can be performed for all sectors obtaining ${}^1\hat{\mathbf{F}}_r(\vartheta_f) \in \mathbb{R}^{1\times n}$, ${}^2\hat{\mathbf{F}}_r(\vartheta_f) \in \mathbb{R}^{1\times n}$, and ${}^3\hat{\mathbf{F}}_r(\vartheta_f) \in \mathbb{R}^{1\times n}$. Then, the minimum values obtained in a fixed electrical position ϑ_{e} among the three sectors are chosen as the force limitation of the machine and are expressed in (4.12).

$$\hat{\mathbf{F}}_r(\vartheta_f) = \min\left(\begin{bmatrix} {}^1\hat{\mathbf{F}}_r(\vartheta_f) \\ {}^2\hat{\mathbf{F}}_r(\vartheta_f) \\ {}^3\hat{\mathbf{F}}_r(\vartheta_f) \end{bmatrix}\right) \tag{4.12}$$

min chooses the minimum value of each column in a matrix. In this chapter, $\hat{\mathbf{F}}_r(\vartheta_f) \in \mathbb{R}^{1\times n}$ is obtained considering the prototype bearingless machine parameters listed in Table 3.1. Figure 4.2 shows the obtained force boundary in

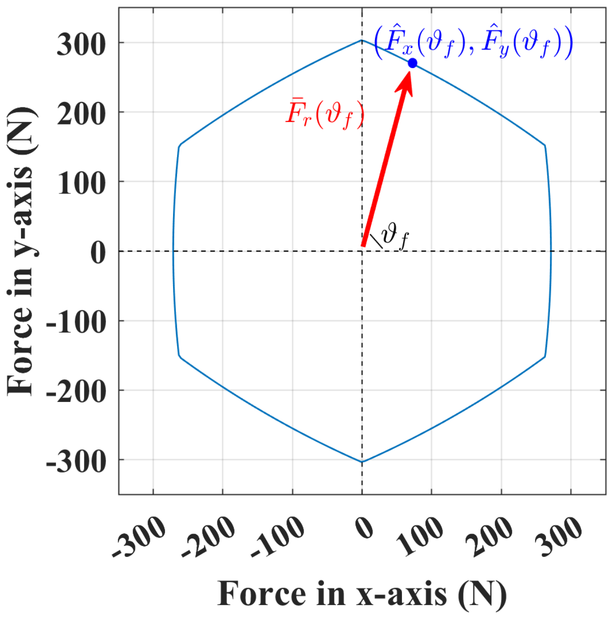

Figure 4.2: *Force limitation* $\left(\hat{F}_x(\vartheta_f), \hat{F}_y(\vartheta_f)\right)$ *when the rotor electrical position is fixed at* $\vartheta_{\mathrm{e}} = 0\,rad$.

the Cartesian plane when rotor electrical position is 0. Varying the electrical position from 0 to 2π and plotting all obtained boundaries leads to the result depicted in Figure 4.3. The blue dashed line defines the maximum force vector module achievable in any rotor position and is computed as

$$\hat{\mathbf{F}}_{r,tot}(\vartheta_{\mathrm{e}}, \vartheta_f) = \min\left(\begin{bmatrix} \hat{\mathbf{F}}_r(\vartheta_{\mathrm{e}} = 0, \vartheta_f) \\ \vdots \\ \hat{\mathbf{F}}_r(\vartheta_{\mathrm{e}} = 2\pi, \vartheta_f) \end{bmatrix}\right). \tag{4.13}$$

In other words, any force vector reference fallen in the blue polygon of Figure 4.3 will not cause an overload phase current. However, the mentioned

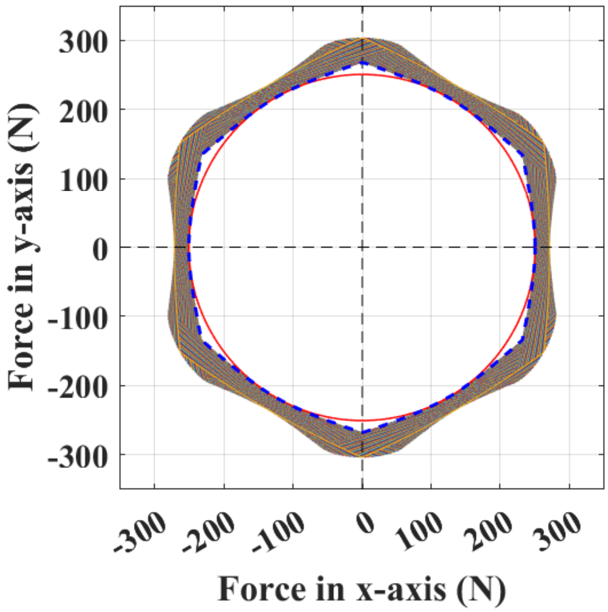

Figure 4.3: *Force limitation of 360 rotor electrical positions and their inscribed circle.*

blue polygon can be approximated by an hexagon. If the hexagon is applied to limit the suspension force reference, the force ripple is bigger than the one when applying a cycle limitation. Therefore, a red circle ,inscribed in the blue polygon, is chosen to be the final force limitation, and depicted in Figure 4.3.

4.3.2 Force limitation for TPOC and SPOC fault operations

The application of the smart current limitation technique described in the previous sub-section is now analysed for TPOC and SPOC faulty operations. In the TPOC fault condition, the faulty sector does not contribute to the force and torque generation. Hence, the matrix $\mathbf{K}_{\alpha\beta,\mathrm{fs}}(\vartheta_\mathrm{e})$ is expressed as in (4.14)-(4.16) for a TPOC fault happening in sector 1, 2, and 3, respectively.

$$\mathbf{K}_{\alpha\beta,\mathrm{f1}}(\vartheta_\mathrm{e}) = \begin{bmatrix} \mathbf{0} & {}^{2}\mathbf{K}_{\alpha\beta}(\vartheta_\mathrm{e}) & {}^{3}\mathbf{K}_{\alpha\beta}(\vartheta_\mathrm{e}) \end{bmatrix} \tag{4.14}$$

$$\mathbf{K}_{\alpha\beta,\mathrm{f2}}(\vartheta_\mathrm{e}) = \begin{bmatrix} {}^1\mathbf{K}_{\alpha\beta}(\vartheta_\mathrm{e}) & \mathbf{0} & {}^3\mathbf{K}_{\alpha\beta}(\vartheta_\mathrm{e}) \end{bmatrix} \tag{4.15}$$

$$\mathbf{K}_{\alpha\beta,\mathrm{f3}}(\vartheta_\mathrm{e}) = \begin{bmatrix} {}^1\mathbf{K}_{\alpha\beta}(\vartheta_\mathrm{e}) & {}^2\mathbf{K}_{\alpha\beta}(\vartheta_\mathrm{e}) & \mathbf{0} \end{bmatrix} \tag{4.16}$$

Equation (4.14)-(4.16) can be substituted into (3.22). Then, the pseudo-inverse of wrench-current matrix can be transformed to direct-quadrature reference frame by the approach presented in section 4.2. Because the faulty sector does not contribute to any forces and torque, the force limits are imposed only to the healthy sectors during the TPOC operative conditions. The approach of obtaining the force limitation of heathy sectors is the same as the one presented in section 4.3.1. Once ${}^s\hat{\mathbf{F}}_r(\vartheta_f)$ of all healthy sectors are obtained, the achievable force boundary of the machine in a fixed rotor electrical position is determined. Equation (4.17) shows the calculation of $\hat{\mathbf{F}}_r(\vartheta_f)$ under sector 1 open circuit faulty condition.

$$\hat{\mathbf{F}}_r(\vartheta_f) = \min\left(\begin{bmatrix} {}^2\hat{\mathbf{F}}_r(\vartheta_f) \\ {}^3\hat{\mathbf{F}}_r(\vartheta_f) \end{bmatrix}\right) \tag{4.17}$$

Substituting (4.17) into (4.13), the achievable force boundaries in TPOC condition is obtained and depicted (the red line) in Figure 4.4.

When a SPOC fault occurs in a sector, the current of the faulty phase goes to zero, while currents in the two remaining healthy phases have the same amplitude but opposite directions due to the isolated star connection neutral point. The mathematical formulation of the SPOC fault has been presented in section 3.4.2, and the pseudo-inverse of the wrench-current coefficient matrix in the three-phase reference frame is reported in (4.18) considering a fault

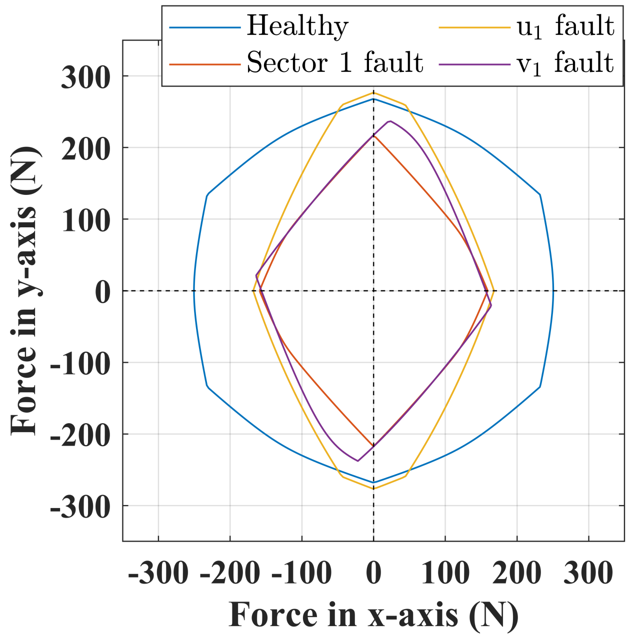

Figure 4.4: *Polygon force limitation in different faulty conditions. Blue is the healthy condition. Red is the sector* 1 *TPOC fault condition. Yellow is the phase* u *of sector* 1 *SPOC fault condition. Purple is the phase* v *of sector* 1 *SPOC fault.*

occurred in the $\varkappa$-phase of the s^{th} sector.

$$\mathbf{K}^{+}_{\mathrm{uvw,fs}}(\vartheta_{\mathrm{e}}) = \begin{bmatrix} {}^{1}k^{+}_{x\mathrm{u}}(\vartheta_{\mathrm{e}}) & {}^{1}k^{+}_{y\mathrm{u}}(\vartheta_{\mathrm{e}}) & {}^{1}k^{+}_{T\mathrm{u}}(\vartheta_{\mathrm{e}}) \\ {}^{1}k^{+}_{x\mathrm{v}}(\vartheta_{\mathrm{e}}) & {}^{1}k^{+}_{y\mathrm{v}}(\vartheta_{\mathrm{e}}) & {}^{1}k^{+}_{T\mathrm{v}}(\vartheta_{\mathrm{e}}) \\ {}^{1}k^{+}_{x\mathrm{w}}(\vartheta_{\mathrm{e}}) & {}^{1}k^{+}_{y\mathrm{w}}(\vartheta_{\mathrm{e}}) & {}^{1}k^{+}_{T\mathrm{w}}(\vartheta_{\mathrm{e}}) \\ \vdots & \vdots & \vdots \\ {}^{s}k^{+}_{x\mathrm{f}}(\vartheta_{\mathrm{e}}) & {}^{s}k^{+}_{y\mathrm{f}}(\vartheta_{\mathrm{e}}) & {}^{s}k^{+}_{T\mathrm{f}}(\vartheta_{\mathrm{e}}) \\ \vdots & \vdots & \vdots \\ {}^{n_s}k^{+}_{x\mathrm{u}}(\vartheta_{\mathrm{e}}) & {}^{n_s}k^{+}_{y\mathrm{u}}(\vartheta_{\mathrm{e}}) & {}^{n_s}k^{+}_{T\mathrm{u}}(\vartheta_{\mathrm{e}}) \\ {}^{n_s}k^{+}_{x\mathrm{v}}(\vartheta_{\mathrm{e}}) & {}^{n_s}k^{+}_{y\mathrm{v}}(\vartheta_{\mathrm{e}}) & {}^{n_s}k^{+}_{T\mathrm{v}}(\vartheta_{\mathrm{e}}) \\ {}^{n_s}k^{+}_{x\mathrm{w}}(\vartheta_{\mathrm{e}}) & {}^{n_s}k^{+}_{y\mathrm{w}}(\vartheta_{\mathrm{e}}) & {}^{n_s}k^{+}_{T\mathrm{w}}(\vartheta_{\mathrm{e}}) \end{bmatrix} \tag{4.18}$$

In (4.18) the subscript $s\varkappa$ means that the SPOC fault occurs in s^{th} sector phase $\varkappa$. The sub-matrix of the faulty sector, presented in (4.19), is described in detail in section 3.4.2.

$${}^{s}\mathbf{K}^{+}_{\mathrm{uvw,f}\varkappa} = \begin{bmatrix} {}^{s}k^{+}_{x\mathrm{f}}(\vartheta_{\mathrm{e}}) & {}^{s}k^{+}_{y\mathrm{f}}(\vartheta_{\mathrm{e}}) & {}^{s}k^{+}_{T\mathrm{f}}(\vartheta_{\mathrm{e}}) \end{bmatrix} \tag{4.19}$$

In SPOC fault conditions, the number of independent phase currents in the faulty sector is reduced from two to one. The magnitude of this current can be computed by ${}^{s}\mathbf{K}^{+}_{\mathrm{uvw,f}\varkappa}(\vartheta_{\mathrm{e}})\ \bar{W}$. For the faulty sector, it is convenient to perform the current limitation in the three-phase reference frame rather than in the direct-quadrature rotor reference frame. However, the inverted coefficients of healthy sectors can be converted to Park rotational coordinate by direct-quadrature transformation as section 4.2 described to achieve smooth force limitation. Therefore the inverted coefficients in SPOC fault conditions can be obtained by combining ${}^{s}\mathbf{K}^{+}_{\mathrm{uvw,f}\varkappa}(\vartheta_{\mathrm{e}})$ and healthy sector sub-matrices, as shown in (4.20).

$$\mathbf{K}^{+}_{\mathrm{dq,fs}\varkappa}(\vartheta_{\mathrm{e}}) = \begin{bmatrix} {}^{1}\mathbf{K}^{+}_{\mathrm{dq}}(\vartheta_{\mathrm{e}}) \\ \vdots \\ {}^{s}\mathbf{K}^{+}_{\mathrm{uvw,f}\varkappa}(\vartheta_{\mathrm{e}}) \\ \vdots \\ {}^{n_s}\mathbf{K}^{+}_{\mathrm{dq}}(\vartheta_{\mathrm{e}}) \end{bmatrix} \tag{4.20}$$

In (4.20), the sub-matrix of healthy sectors are in the direct-quadrature rotor reference frame, whereas the sub-matrix of the faulty sector ${}^{s}\mathbf{K}^{+}_{\mathrm{uvw,f}\varkappa}(\vartheta_{\vartheta_{\mathrm{e}}})$ is in the three-phase reference frame. The force limitations of healthy sectors are obtained by the technique presented in section 4.3.1, applying (4.8)-(4.11). Under an assumption of $0Nm$ torque, the force limitation of the SPOC faulty sector in a fixed electrical position is obtained by applying (4.21).

$${}^{s}\hat{F}_r(\vartheta_f) = \left| \frac{\hat{i}_{amp}}{{}^{s}k^{+}_{x\mathrm{f}}(\vartheta_{\mathrm{e}})\cos(\vartheta_f) + {}^{s}k^{+}_{y\mathrm{f}}(\vartheta_{\mathrm{e}})\sin(\vartheta_f)} \right| \tag{4.21}$$

where ${}^{s}k^{+}_{x\mathrm{f}}(\vartheta_{\mathrm{e}})$ and ${}^{s}k^{+}_{y\mathrm{f}}(\vartheta_{\mathrm{e}})$ are the elements of the sub-matrix ${}^{s}\mathbf{K}^{+}_{\mathrm{uvw,f}\varkappa}(\vartheta_{\mathrm{e}})$. Varying ϑ_f from 0 to 2π and then substituting the results of (4.21) into (4.12), the force limitation for a SPOC fault in one electrical position is obtained. The global force limits can be obtained by applying (4.13), varying the rotor position from 0 to 2π. The force limitation polygons of sector 1 phase u and phase v SPOC fault conditions are separately shown on Figure 4.4, where the force limitation boundaries for healthy condition and TPOC fault in sector 1 are also reported. The force limitation boundaries for TPOC faults in sector 2 and 3 can be obtained by rotating the boundary of TPOC fault in sector 1 by 120 degrees counter-clockwise and 240 degrees counter-clockwise, respectively.

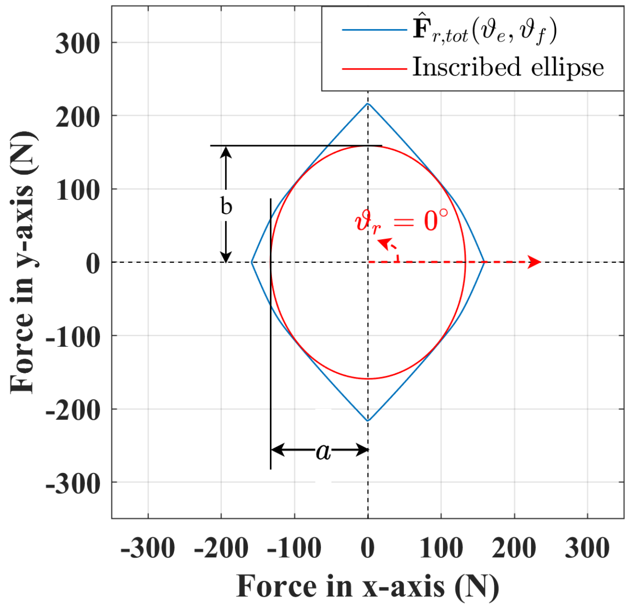

Figure 4.5: *Polygon force limitation of TPOC condition and its inscribed ellipse (sector 1 TPOC fault).*

The maximum $x - y$ axis force changing may cause force ripples. In order to achieve smooth force limitation and decrease the DSP effort, inscribed ellipses are computed and considered as the final force limitation, taking into account the balance of the force limits between x-axis and y-axis. The blue line of Figure 4.5 shows the polygon force boundary of sector 1 TPOC fault condition, and the inscribed red ellipse is set to limit the force. Equation (4.22) is the function describing the ellipses:

$$\begin{bmatrix} x(\vartheta_{ellipse}) \\ y(\vartheta_{ellipse}) \end{bmatrix} = \begin{bmatrix} a \cos(\vartheta_{ellipse}) \\ b \sin(\vartheta_{ellipse}) \end{bmatrix} \tag{4.22}$$

where a and b are semi-major and semi-minor axes of the ellipse, respectively, illustrated in Figure 4.5. $\begin{bmatrix} x(\vartheta_{ellipse}) & y(\vartheta_{ellipse}) \end{bmatrix}'$ is the function of $\vartheta_{ellipse}$, $\vartheta_{ellipse} \in [0 \ldots 2\pi]$. i.e., when $\vartheta_{ellipse} = 0$, the point $\begin{bmatrix} x(\vartheta_{ellipse}) & y(\vartheta_{ellipse}) \end{bmatrix}'$ is on the intersection of x-axis and ellipse.

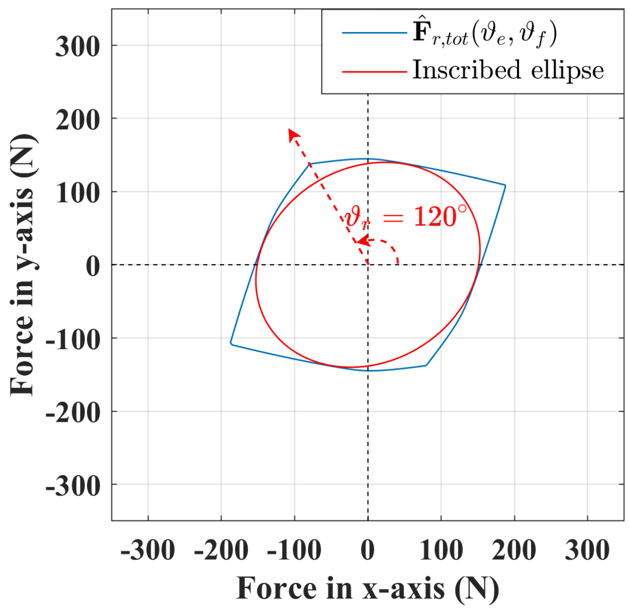

Figure 4.6: *Polygon force limitation of TPOC condition and its inscribed ellipse (sector 2 TPOC fault).*

For the TPOC fault in sector 2, the polygon force boundary is obtained by rotating the boundary of TPOC fault in sector 1 by 120 degrees counter-clockwise, resulting in the rotated ellipse, as shown in Figure 4.6. The parameters of the ellipse (a and b) are still valid, but a rotation matrix should be introduced to rotate the ellipse, as expressed in (4.23):

$$\begin{bmatrix} x(\vartheta_{ellipse}) \\ y(\vartheta_{ellipse}) \end{bmatrix} = \begin{bmatrix} \cos(\vartheta_r) & -\sin(\vartheta_r) \\ \sin(\vartheta_r) & \cos(\vartheta_r) \end{bmatrix} \begin{bmatrix} a\ \cos(\vartheta_{ellipse}) \\ b\ \sin(\vartheta_{ellipse}) \end{bmatrix} \tag{4.23}$$

where ϑ_r is rotational angle of the ellipses. It is 0 degrees for TPOC in sector 1 (see Figure 4.5), 120° in Figure 4.6, and 240° when the sector 3 TPOC fault.

For the considered machine, the data of force limits is obtained by maximum achievable phase current 18.5A and listed in the Table 4.1. Although the rated

Table 4.1: Ellipse parameters of different operating conditions

Operational conditions	**a (N)**	**b (N)**	$\vartheta_r(deg)$
Healthy	250	250	0
sector 1 TPOC	133	159	0
sector 2 TPOC	133	159	120
u_1 SPOC	151	189	0
u_2 SPOC	151	189	120
v_1 SPOC	136	158	-5
w_1 SPOC	136	158	5

phase current of the proposed machine is 13A, the machine can be overloaded for a short time (approximately 10 minutes; otherwise, thermal overload is achieved). Hence, the maximum achievable current can be chosen depending on the capability of the machine.

4.4 Torque limitation

4.4.1 Torque limitation in healthy operations

In the smart current limitation technique, the limited force references are used to calculate the torque limit with respect to the rotor angular position. The limited force references and electrical position ϑ_e are considered constant in a controller sampling interval. Hence, the force components of the current are also constant. Such components are here referred to as ${}^s\alpha_\mathrm{d}$ and ${}^s\alpha_\mathrm{q}$, respectively, and expressed in (4.24):

$$\begin{aligned}{}^s\alpha_\mathrm{d} &= {}^sk^+_{x\mathrm{d}}(\vartheta_\mathrm{e})\widetilde{F}^*_x + {}^sk^+_{y\mathrm{d}}(\vartheta_\mathrm{e})\widetilde{F}^*_y \\ {}^s\alpha_\mathrm{q} &= {}^sk^+_{x\mathrm{q}}(\vartheta_\mathrm{e})\widetilde{F}^*_x + {}^sk^+_{y\mathrm{q}}(\vartheta_\mathrm{e})\widetilde{F}^*_y\end{aligned} \tag{4.24}$$

where $\widetilde{F}_x^*$ and $\widetilde{F}_y^*$ are the limited force references detailed in Figure 4.1. Considering the torque T, the current i_{amp} can be rewritten as

$$\begin{aligned} i_{amp} =& \sqrt{{}^s i_{\mathrm{d}}{}^2 + {}^s i_{\mathrm{q}}{}^2} \\ =& \sqrt{\left({}^s\alpha_{\mathrm{d}} + {}^s k_{T\mathrm{d}}^{+}(\vartheta_{\mathrm{e}})T\right)^2 + \left({}^s\alpha_{\mathrm{q}} + {}^s k_{T\mathrm{q}}^{+}(\vartheta_{\mathrm{e}})T\right)^2} \\ =& \sqrt{\begin{aligned} &T^2\left({}^s k_{T\mathrm{d}}^{+}(\vartheta_{\mathrm{e}})^2 + {}^s k_{T\mathrm{q}}^{+}(\vartheta_{\mathrm{e}})^2\right) \\ &+ T\left(2\,{}^s\alpha_{\mathrm{d}}\,{}^s k_{T\mathrm{d}}^{+}(\vartheta_{\mathrm{e}}) + 2\,{}^s\alpha_{\mathrm{q}}\,{}^s k_{T\mathrm{q}}^{+}(\vartheta_{\mathrm{e}})\right) \\ &+ \left({}^s\alpha_{\mathrm{d}}^2 + {}^s\alpha_{\mathrm{q}}^2\right) \end{aligned}} \end{aligned} \quad . \tag{4.25}$$

As described in section 4.3.2, the peak value of phase current $\hat{i}_{amp}$ can be set to $18.5A$ for the machine under investigation. During a sampling interval, $\hat{i}_{amp}$, ${}^s\alpha_{\mathrm{d}}$, ${}^s\alpha_{\mathrm{q}}$, ${}^s k_{T\mathrm{d}}^{+}(\vartheta_{\mathrm{e}})$, and ${}^s k_{T\mathrm{q}}^{+}(\vartheta_{\mathrm{e}})$ are known and constant. The roots of (4.25), ${}^{-}\hat{T}_s$ and ${}^{+}\hat{T}_s$, represent the peak negative and positive achievable torques of the s^{th} sector, respectively. The torque limits of the machine, ${}^{-}T_{max}$ and ${}^{+}T_{max}$ expressed in (4.26), are the maximum value of the three ${}^{-}\hat{T}_s$ and the minimum value of the three ${}^{+}\hat{T}_s$, respectively.

$$\begin{aligned} {}^{-}T_{max} &= \max\left(\begin{bmatrix} {}^{-}\hat{T}_1 & {}^{-}\hat{T}_2 & {}^{-}\hat{T}_3 \end{bmatrix}'\right) \\ {}^{+}T_{max} &= \min\left(\begin{bmatrix} {}^{+}\hat{T}_1 & {}^{+}\hat{T}_2 & {}^{+}\hat{T}_3 \end{bmatrix}'\right) \end{aligned} \tag{4.26}$$

Therefore, the proposed algorithm is expected to compute (4.25) and (4.26) in every sampling interval. The results of (4.26) are applied to limit the output of the speed controller.

4.4.2 Torque limitation for TPOC and SPOC operations

The torque limitation technique applied to TPOC operative condition is similar to the approach implemented for the healthy condition. In TPOC faulty condition, the faulty sector does not produce torque and force. Therefore, only healthy sectors are accounted for torque limitation. Equations (4.27)-(4.29) represent torque limits when a TPOC fault occurs in sector 1, 2 and 3, respectively.

$$\begin{aligned} {}^{-}T_{max} &= \max\left(\begin{bmatrix} {}^{-}\hat{T}_2 & {}^{-}\hat{T}_3 \end{bmatrix}'\right) \\ {}^{+}T_{max} &= \min\left(\begin{bmatrix} {}^{+}\hat{T}_2 & {}^{+}\hat{T}_3 \end{bmatrix}'\right) \end{aligned} \tag{4.27}$$

$$\begin{aligned} {}^{-}T_{max} &= \max\left(\begin{bmatrix} {}^{-}\hat{T}_1 & {}^{-}\hat{T}_3 \end{bmatrix}'\right) \\ {}^{+}T_{max} &= \min\left(\begin{bmatrix} {}^{+}\hat{T}_1 & {}^{+}\hat{T}_3 \end{bmatrix}'\right) \end{aligned} \tag{4.28}$$

$$\begin{aligned} {}^{-}T_{max} &= \max\left(\begin{bmatrix} {}^{-}\hat{T}_1 & {}^{-}\hat{T}_2 \end{bmatrix}'\right) \\ {}^{+}T_{max} &= \min\left(\begin{bmatrix} {}^{+}\hat{T}_1 & {}^{+}\hat{T}_2 \end{bmatrix}'\right) \end{aligned} \tag{4.29}$$

In the SPOC fault condition, the pseudo-inverse matrix of the faulty sector contains only one row. α_f, the force component of the current of faulty sector is expressed as in (4.30).

$${}^{s}\alpha_f = {}^{s}k^{+}_{x\mathrm{f}}(\vartheta_{\mathrm{e}})\widetilde{F}^{*}_{x} + {}^{s}k^{+}_{y\mathrm{f}}(\vartheta_{\mathrm{e}})\widetilde{F}^{*}_{y} \tag{4.30}$$

In a sampling interval, α_f remains constant. Therefore, the torque limits ${}^{+}\hat{T}_s(\vartheta_{\mathrm{e}}, \alpha_f)$ and ${}^{-}\hat{T}_s(\vartheta_{\mathrm{e}}, \alpha_f)$ of the faulty sector can be calculated as in (4.31) and (4.32), respectively.

$${}^{+}\hat{T}_s(\vartheta_{\mathrm{e}}, \alpha_f) = \begin{cases} \frac{\hat{i}_{amp}-\alpha_f}{k^{+}_{T\mathrm{f}}(\vartheta_{\mathrm{e}})} & if\ k^{+}_{T\mathrm{f}}(\vartheta_{\mathrm{e}}) > 0 \\ \frac{-\hat{i}_{amp}-\alpha_f}{k^{+}_{T\mathrm{f}}(\vartheta_{\mathrm{e}})} & if\ k^{+}_{T\mathrm{f}}(\vartheta_{\mathrm{e}}) < 0 \end{cases} \tag{4.31}$$

$${}^{-}\hat{T}_s(\vartheta_{\mathrm{e}}, \alpha_f) = \begin{cases} \frac{-\hat{i}_{amp}-\alpha_f}{k^{+}_{T\mathrm{f}}(\vartheta_{\mathrm{e}})} & if\ k^{+}_{T\mathrm{f}}(\vartheta_{\mathrm{e}}) > 0 \\ \frac{\hat{i}_{amp}-\alpha_f}{k^{+}_{T\mathrm{f}}(\vartheta_{\mathrm{e}})} & if\ k^{+}_{T\mathrm{f}}(\vartheta_{\mathrm{e}}) < 0 \end{cases} \tag{4.32}$$

The graphical representation of (4.31) and (4.32) is reported in Figure 4.7 showing the relationship between the torque and $\hat{i}_{amp}$.

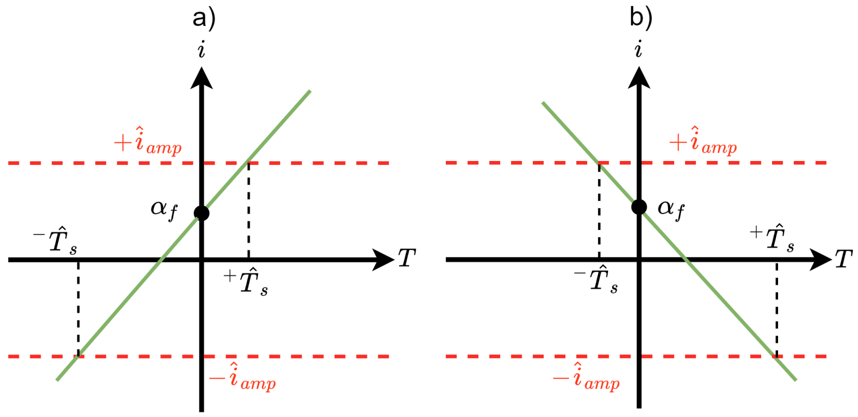

Figure 4.7: *Graphical representation of* (4.31) *and* (4.32)*. a)* $k^{+}_{T\mathrm{f}}(\vartheta_{\mathrm{e}}) > 0$*. b)* $k^{+}_{T\mathrm{f}}(\vartheta_{\mathrm{e}}) < 0$*.*

The torque limits of the healthy sector are obtained by the approach presented in section 4.4.1. Finally, the global torque limit of the machine can be obtained by (4.26). The results of (4.26) is applied to limit the speed controller output. Using the limited torque reference $\widetilde{T}^{*}$, phase current reference can be calculated.

4.5 Numerical simulation results

In this section, three different simulations are performed in the MATLAB Simulink environment. All simulations are implemented for a SPOC fault in phase u of sector 1. The first one shows a conservative current limitation technique that limits to constant values the $x-y$ axes suspension force and torque reference signals, respectively, as shown by the red blocks in Figure 4.8 a). The reference force magnitudes are limited to 120N, and the output torque of the speed controller is limited to 2.5Nm. These are the maximum force and torque that the machine can produce simultaneously without exceeding current limit during a SPOC fault in phase u_1. The second simulation shows the standard current limitation method that limits the current reference directly, as shown in Figure 4.8 b). In this case, the outputs of the position controllers and the speed controller are limited to 270N and 7.2Nm, respectively. The current references will exceed 18.5A if 270N force or 7.2Nm torque are required. Therefore, it is necessary to implement a saturation block before the current loop so that the current references are limited to 18.5A. Compared to the conservative limitation method, the standard limitation method mainly limits the current references instead of limiting the outputs of the position controllers and the speed controller. The saturation blocks linked to the position controllers and the speed controller, only stop the controllers generating references which significantly exceed the capability of the machine. The third simulation presents

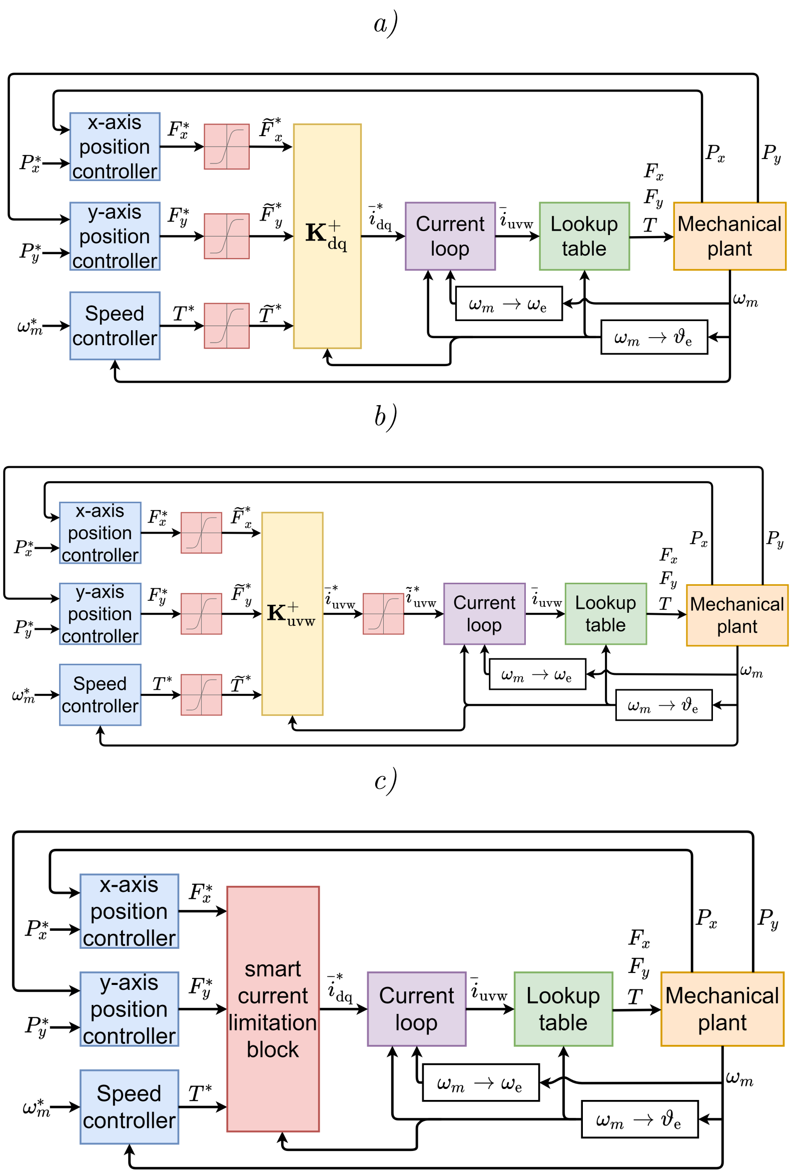

Figure 4.8: *Simulation diagram of the bearingless machine control system. a) Schematic diagram of the conservative current limitation. b) Schematic diagram of the standard current limitation method. c) Schematic diagram of the proposed smart current limitation. The detail of the smart current limitation block is shown in Figure 4.1.*

the implementation of the smart current limitation technique presented in this chapter. Its schematic diagram is reported in Figure 4.8 c) where the content of the red block is shown in Figure 4.1. The outputs of position controllers are limited by an ellipse as described in section 4.3. The limited force references are used in the torque limitation technique described in section 4.4 to obtain the torque limits. Finally, $\bar{i}_{\mathrm{dq}} = \mathbf{K}^{+}_{\mathrm{dq}}(\vartheta_{\mathrm{e}})[\widetilde{F}^{*}_{x}, \widetilde{F}^{*}_{y}, \widetilde{T}^{*}]'$ is used to calculate current references from limited forces and torque references.

In Figure 4.8 a), b), and c), the position controllers, the speed controllers, the current loops, and the mechanical plants are identical, as presented in section 3.6.1. The current loop block contains current controllers, the power electronic devices, and the machine current plant. The power modules switching frequency is 10kHz. The lookup table obtained from FE software reflects the forces and the torque generated by the machine phase currents. The rotor x-y coordinate position and rotational speed are the state variable of the mechanical plant.

These three simulations are implemented in the same operating conditions. The rotor is suspended in the stator center and accelerated to 300rpm rotational speed before 1s. At 1.1s, the speed reference changes from 300rpm to 1000rpm. The comparison between the conservative method and the smart current limitation technique is shown in Figure 4.9. The comparison between the standard method and the smart current limitation technique is shown in Figure 4.10.

From Figure 4.9 a), it is observed that the speed transient time of the conservative method is longer than the smart limitation technique because the latter calculates online the torque limit which ensures that the machine capability is fully exploited as it can be appreciated by observing the torque in Figure 4.9 b). However, the torque reference of the conservative method is limited to 2.5Nm to avoid the overload. The rotor $x - y$ axes positions of the two simulations remain stable in the centre of the stator during the speed transient.

a)

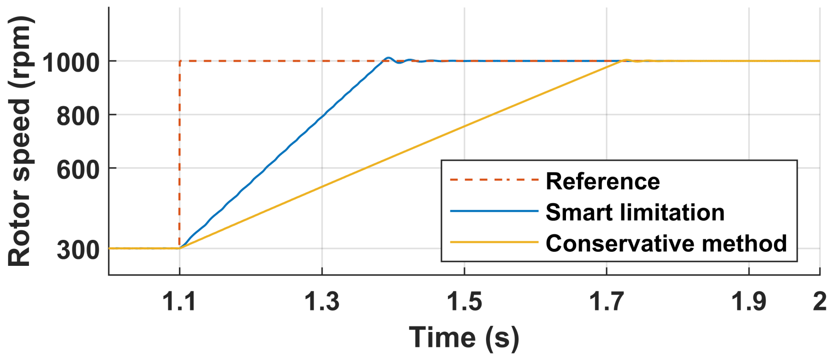

b)

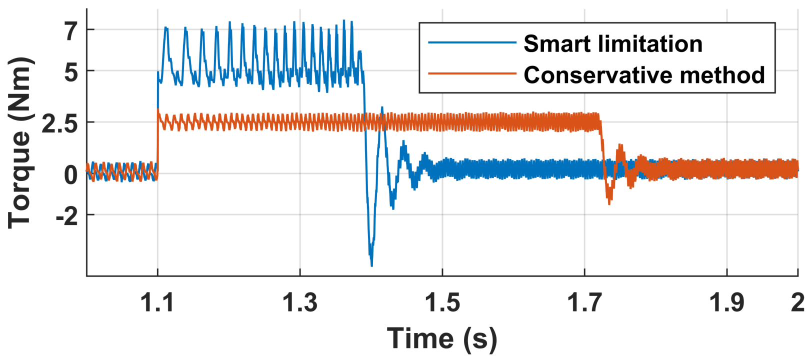

Figure 4.9: *Simulation results: the comparison between the conservative method and the smart current limitation technique. a) Speed transient. b) Torque outputs from the lookup tables.*

Figure 4.10 shows the comparison between the standard method and the smart current limitation technique. Both methods are equipped with identical speed controllers. Therefore, the performance limits caused by speed controllers are negligible. From Figure 4.10 a), it can be noted that the rotor $x - y$ axes position of the standard method is significantly affected by the speed transient because, in this interval, the force feedbacks do not perfectly follow the force references as shown in Figure 4.10 b). Indeed, the standard method limits the current references without considering the force direction. Therefore, the force generated deteriorates when a high torque or force value is required. Furthermore, the standard method may cause rotor touchdown with the backup bearing if a big force disturbance is added to the shaft. Therefore, the standard method is not suitable for the bearingless machine. The speed transients of two simulations displayed in Figure 4.10 c) are almost the same because the

a)

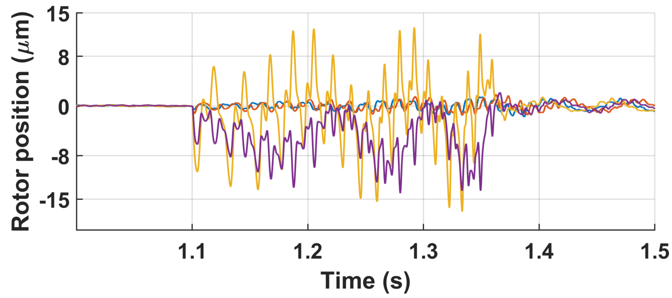

b)

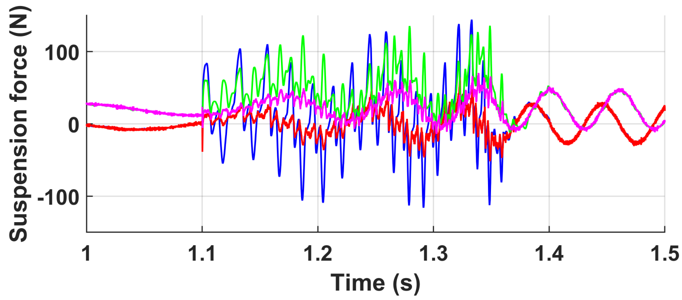

c)

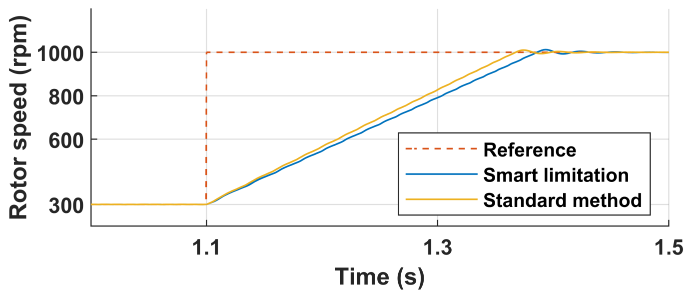

d)

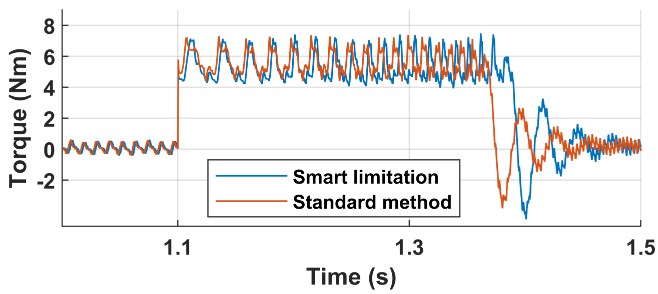

Figure 4.10: *Simulation results: the comparison between the standard method and the smart current limitation. a) The blue line and the red line are the rotor $x-y$ axes positions of smart limitation technique. The yellow line and the purple line are the rotor $x-y$ axes positions of the standard method. b) Suspension forces of the standard limitation method. The blue line and the red line are the reference and the feedback of the x-axis force, respectively. The green line and the pink line are the reference and the feedback of the y-axis force, respectively. c) Speed transients of two approaches. d) Torque outputs from the lookup table.*

achievable torques of the two approaches are similar as shown in Figure 4.10 d).

4.6 Experimental validations

The current limitation techniques validated in section 4.5 have been experimentally verified on the prototype bearingless MS-PMSM, presented in this section. The experimental rig used for the validation has been introduced in section 3.6.2. The experimental validation compares the performance of the conservative and standard approaches with the new smart current limitation technique under a SPOC fault in phase u_1. The power inverter rated current is 20A. Therefore, the maximum output current of the controller is limited to 18.5A. With this current constraint, the suspension force and the torque of the conservative saturation approach are limited to 120N and 2.5Nm, respectively.

The three approaches are verified in the same conditions. The BM operates at 300rpm with the rotor in [$0\mu m$, $0\mu m$] and with a SPOC fault in phase u_1 before 0.1s. Then, the speed reference changes from 300rpm to 1000rpm. Figure 4.11 displays the speed curves of the three approaches. It can be observed

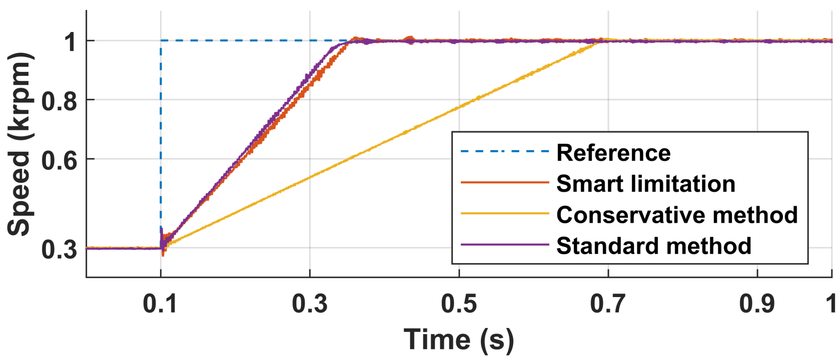

Figure 4.11: *Speed transients of experimental tests. The three tests are performed with the same speed reference.*

that the smart limitation technique and the standard method accelerate faster than the conservative method because the output torque of the conservative method is limited to 2.5Nm. In other words, the conservative method cannot exploit the full capabilities of the machine. Table 4.2 lists the average output torque during the speed transient and the percentage value related to the rated torque of the machine (5Nm).

Table 4.2: The average output torque during the speed transient and the torque exploitation

	conservative method	**smart limitation**	**standard method**
Average generated torque (Nm)	2.5	5	5
Machine torque exploitation (%)	50	100	100

The conservative method only employs 50% of the potential of the BM, whereas the smart limitation technique reaches 100%. This also can be verified by observing the phase currents. Figure 4.12, 4.13, and 4.14, displays the phase currents of the conservative method, the smart current limitation technique, and the standard approach, respectively. During the speed transient, the average peak value of the conservative method is 10A as displayed in Figure 4.12. Instead, the average peak values of the phase currents generated by the smart current limitation technique and standard method are around 19A, almost two times the one achieved by the conservative approach. The results clearly reflect the disadvantages of the conservative method.

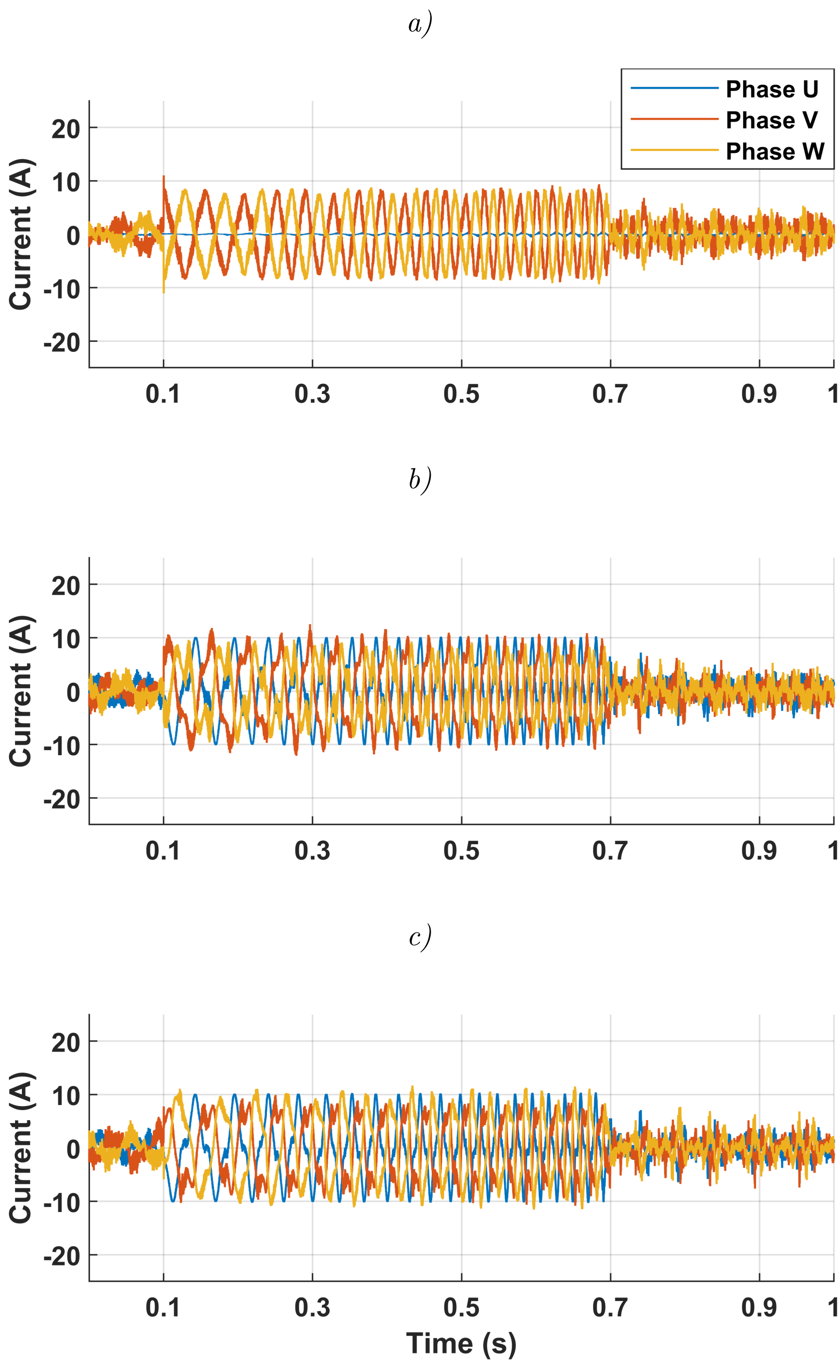

Figure 4.12: *Measured phase currents of experimental tests of conservative current limitation technique. a) Sector 1. b) Sector 2. c) Sector 3.*

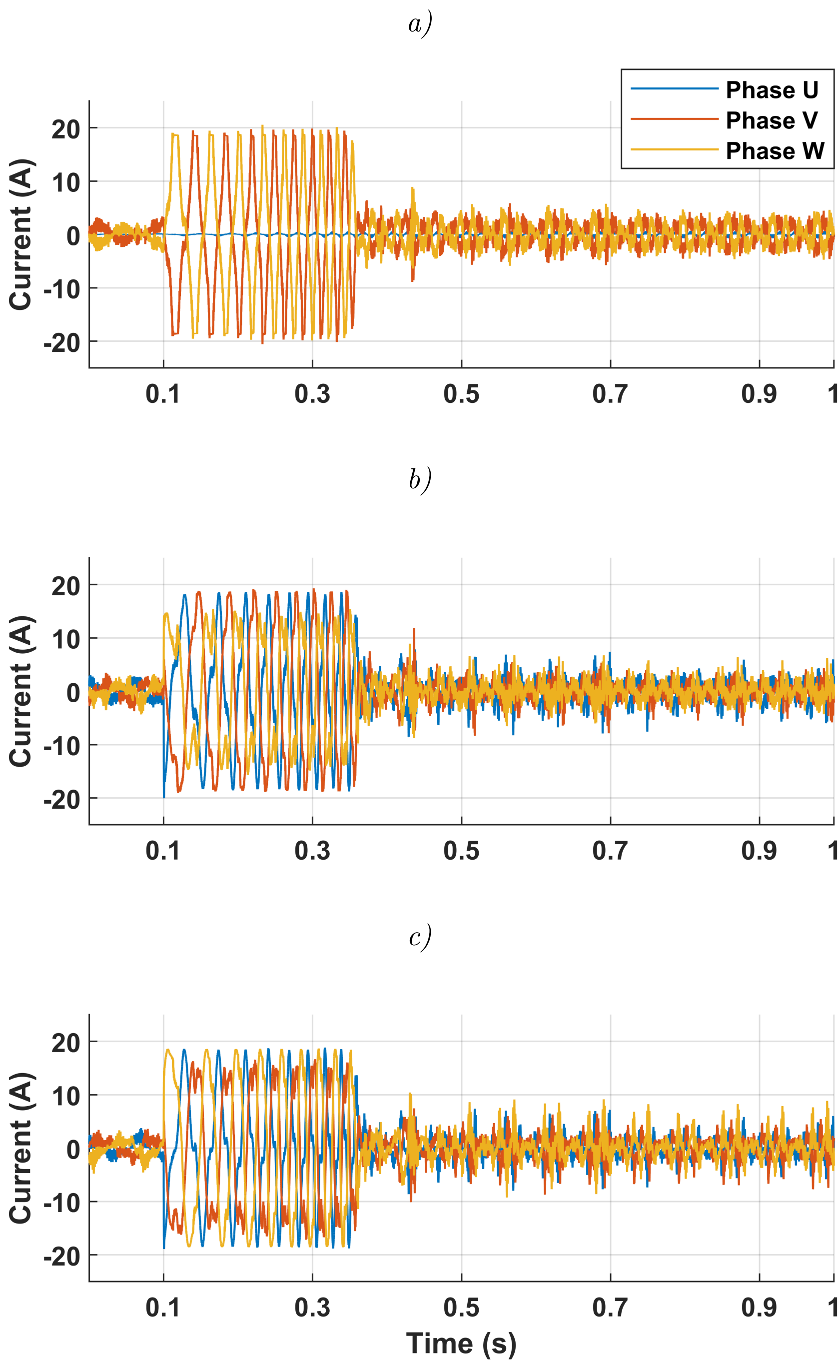

Figure 4.13: *Measured phase currents of experimental tests with smart current limitation technique. a) Sector 1. b) Sector 2. c) Sector 3.*

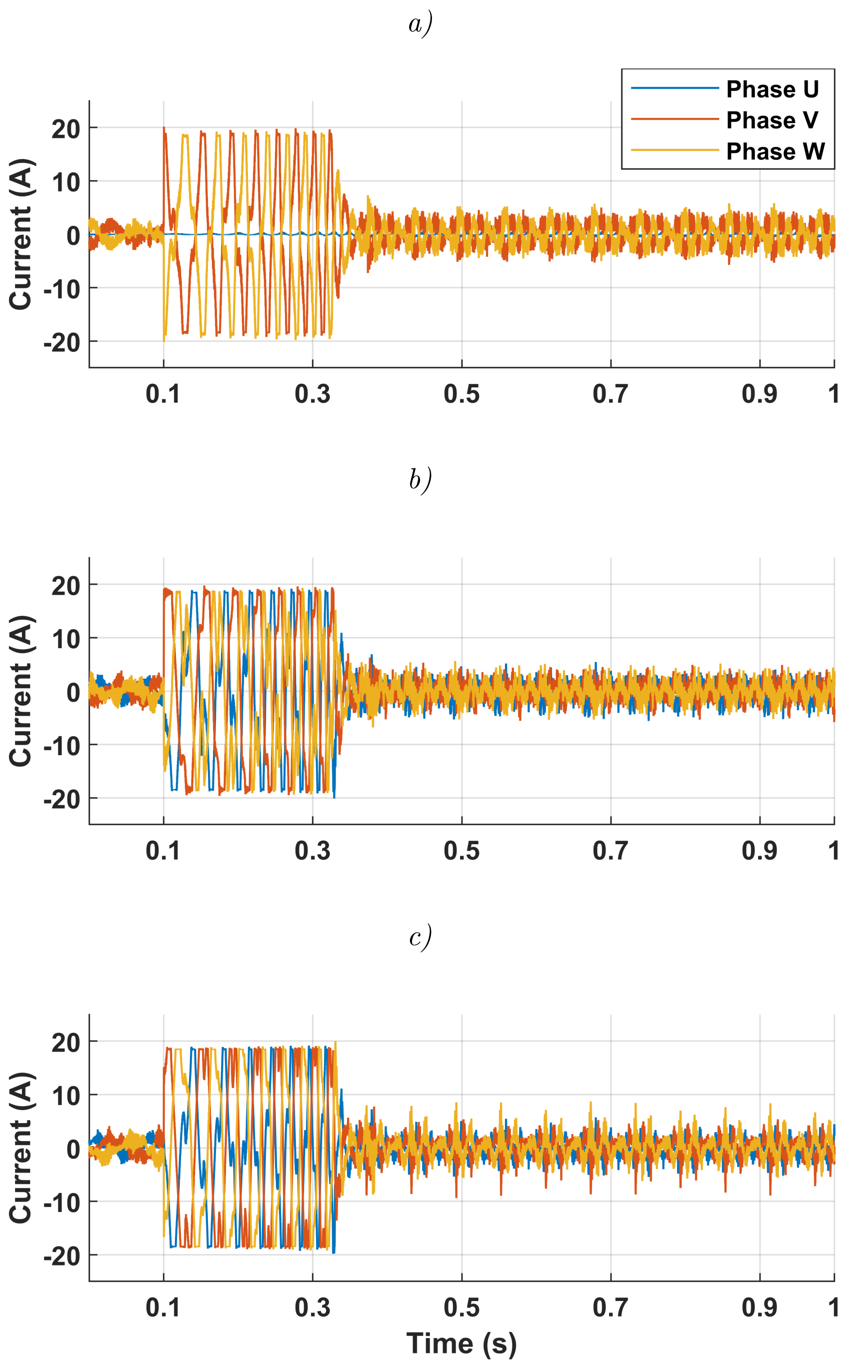

Figure 4.14: *Measured phase currents of experimental tests with standard current limitation technique. a) Sector 1. b) Sector 2. c) Sector 3.*

The comparison between the rotor positions of the standard method and the smart approach during the speed transient is displayed in Figure 4.15. The rotor radial positions, measured from the system equipped with the smart limitation technique, keep stable within a 15μm ripple during the experiment, as shown in Figure 4.15 a). However, it can be noticed that a large ripple

a)

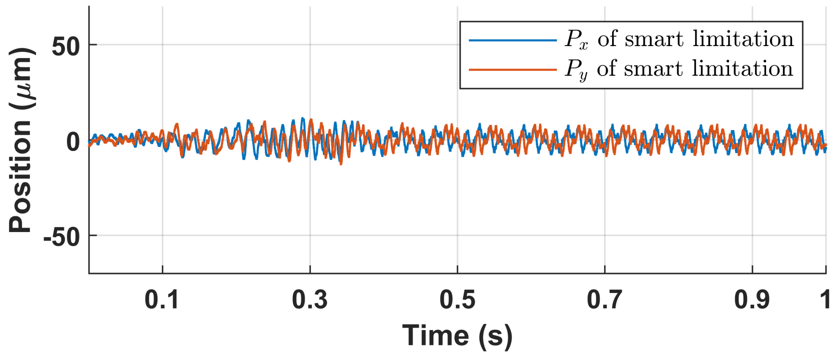

b)

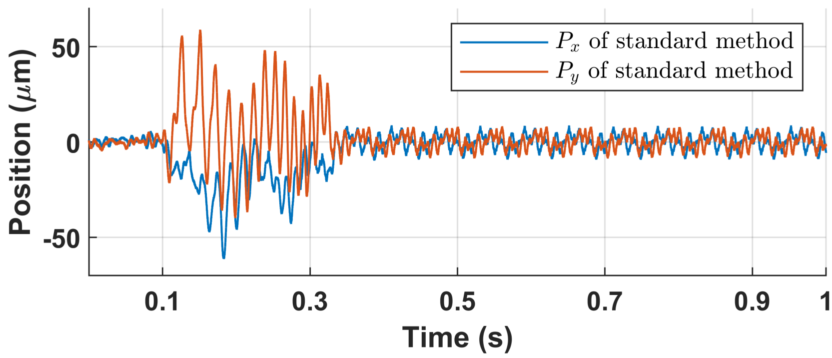

Figure 4.15: *Measured rotor $x - y$ axes positions of experimental tests. a) Smart limitation technique. b) Standard method.*

exists in the curves of the standard method (Figure 4.15 b)) because it directly limits the output current references, which results in a significant error of force direction.

In order to verify the improvement in the position loop, an additional test is implemented to compare the performance between the standard method, the conservative method, and the smart approach. To test each technique, the speed reference is set to change from 300rpm to 1000rpm at 0.1s and, at the same time, the rotor is pulled to the stator center [0μm, 0μm] starting

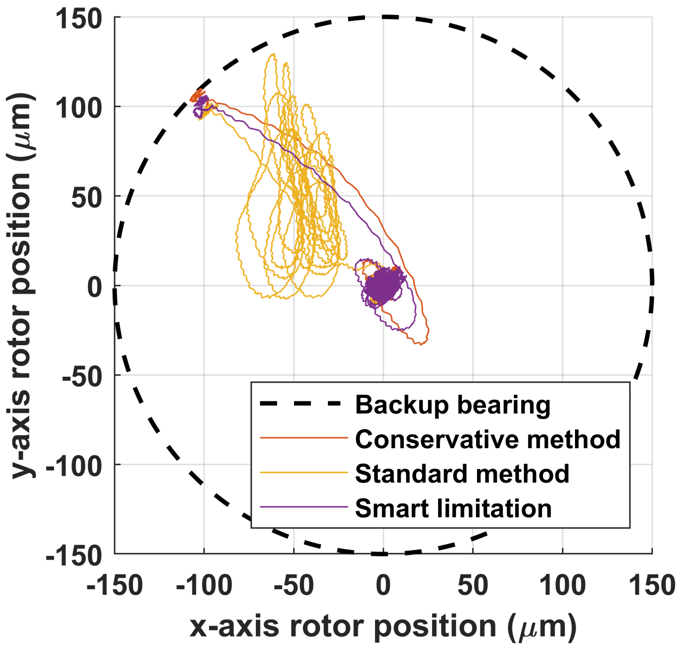

Figure 4.16: *Rotor $x - y$ axes position of the three approaches.*

from its initial position in $[-100\mu m, 100\mu m]$. This case studies results in the worst operating conditions for the BM as both torque and suspension force requirements are very large due to the speed and position transients, respectively.

Figure 4.16 shows the experimental results of the three tests. It is observed that the standard method generates a significant position ripple, whereas both smart technique and conservative method are able to pull the rotor to the stator centre with a similar transient.

This section shows how the proposed smart saturation technique outperforms the conservative method in term of speed transient avoiding, at the same time, forces distortion present in the standard method.

4.7 Conclusion

A smart current limitation technique that prioritises suspension force generation is presented and validated with numerical simulations and experimental tests. The algorithm is applied to a bearingless MS-PMSM featuring a combined winding structure. The technique is validated in faulty operation. The results show that the technique allows to maintain the rotor levitation and therefore avoids a potentially destructive touchdown during transient. Additionally, it shows how the proposed approach outperforms conservative current saturation techniques, always guaranteeing to exploit the maximum available torque during transients, limiting torque distortion and position ripple.

Chapter 5

Current-Sharing Control for the Bearingless Multi-Sector Permanent Magnet Synchronous Machine

5.1 Introduction

The control algorithm of open-circuit faults has been introduced in chapter 3. The proposed technique allows the sectored MS PMSM to operate in TPOC or SPOC fault conditions, but the output power is limited. Then, chapter 4 explores an approach to exploit the maximum capability of the proposed machine, in healthy and faulty operations. When an open-circuit occurs in a power inverter or power source, technical teams may not have an identical backup power source, resulting in the machine being supplied by power sources with different power rating. To operate the machine with the such condition, another interesting feature of the proposed MS machines is the possibility of independently managing the power flows among the different m-phase sub-windings, hence achieving the so-called current-sharing operation [31, 32]. The proposed BM has already been investigated in [53] with current-sharing capability among sectors. However, the presented control strategy was based on the vector space decomposition approach. Such approach treats the whole winding layout as a unique system, thus losing the modular approach and making the fault-tolerant control more complex and challenging.

This chapter presents a modular current-sharing control strategy of a MS bearingless PMSM. The proposed control is fully based on the modularity of the multi-three-phase drive, extending the conventional bearingless control to the management of current-sharing among the sub-windings and to the fault tolerant control acting in case of sector open-phase fault. A detailed modelling of the machine electro-mechanical behaviour is described in section 3.3.1 aided by a FEA of the considered machine. Then, the wrench-current matrix is converted to the DQ reference frame in section 5.2 to conveniently implement the current-sharing controller in section 5.3 that outlines the implemented control strategies to achieve current-sharing among stator sectors during bearingless operation in both healthy and faulty conditions. A brief overview of the control system diagram is presented in section 5.4 along with a detailed FEA aimed at assessing the effects of neglecting the mutual interaction among stator sectors. Finally, section 5.5 reports an extensive test campaign on a prototyped machine validating the bearingless current-sharing operation in healthy and faulty scenarios, both at steady state and transient conditions.

5.2 Wrench-current coefficient in current-sharing operations.

In (3.20), the wrench-current coefficient matrix, $\mathbf{K}_{\alpha\beta}(\vartheta_{\mathrm{e}})$, is obtained by FEA simulation. To achieve the current-sharing control, the matrix can be converted to DQ reference frame by the rotation matrix $\mathbf{T}_{\mathrm{dq}2\alpha\beta}(\vartheta_{\mathrm{e}})$, presented in the following equation:

$$\begin{aligned}\mathbf{K}_{\mathrm{dq}}(\vartheta_{\mathrm{e}}) &= \begin{bmatrix} {}^{1}\mathbf{K}_{\mathrm{dq}}(\vartheta_{\mathrm{e}}) & {}^{2}\mathbf{K}_{\mathrm{dq}}(\vartheta_{\mathrm{e}}) & {}^{3}\mathbf{K}_{\mathrm{dq}}(\vartheta_{\mathrm{e}}) \end{bmatrix} \\ &= \begin{bmatrix} {}^{1}\mathbf{K}_{\alpha\beta}(\vartheta_{\mathrm{e}})\mathbf{T}_{\mathrm{dq}2\alpha\beta}(\vartheta_{\mathrm{e}}) & {}^{2}\mathbf{K}_{\alpha\beta}(\vartheta_{\mathrm{e}})\mathbf{T}_{\mathrm{dq}2\alpha\beta}(\vartheta_{\mathrm{e}}) & {}^{3}\mathbf{K}_{\alpha\beta}(\vartheta_{\mathrm{e}})\mathbf{T}_{\mathrm{dq}2\alpha\beta}(\vartheta_{\mathrm{e}}) \end{bmatrix}\end{aligned} \tag{5.1}$$

where

$$\begin{aligned}\mathbf{T}_{\mathrm{dq}2\alpha\beta}(\vartheta_{\mathrm{e}}) &= \begin{bmatrix} \cos(\vartheta_{\mathrm{e}}) & -\sin(\vartheta_{\mathrm{e}}) \\ \sin(\vartheta_{\mathrm{e}}) & \cos(\vartheta_{\mathrm{e}}) \end{bmatrix} \\ {}^{s}\mathbf{K}_{\mathrm{dq}}(\vartheta_{\mathrm{e}}) &= \begin{bmatrix} {}^{s}k_{x\mathrm{d}}(\vartheta_{\mathrm{e}}) & {}^{s}k_{x\mathrm{q}}(\vartheta_{\mathrm{e}}) \\ {}^{s}k_{y\mathrm{d}}(\vartheta_{\mathrm{e}}) & {}^{s}k_{y\mathrm{q}}(\vartheta_{\mathrm{e}}) \\ {}^{s}k_{T\mathrm{d}} & {}^{s}k_{T\mathrm{q}} \end{bmatrix}.\end{aligned} \tag{5.2}$$

Particularly, since the d-axis currents do not contribute to any torque, ${}^{s}k_{T\mathrm{d}}$ is 0, and ${}^{s}k_{T\mathrm{q}}$, in fact, is the torque constant k_T reported in Table 3.1.

5.3 Current-sharing operation

5.3.1 Healthy condition current-sharing

The current-sharing operation can be defined by introducing the vector of the sharing coefficients $Z_{sh} = [{}^{1}z_{sh}, {}^{2}z_{sh}, ..., {}^{n_s}z_{sh}]'$ determining the reference q-axis currents $\bar{i}_{\mathrm{q}}^{*} = [{}^{1}i_{\mathrm{q}}^{*}, {}^{2}i_{\mathrm{q}}^{*}, ..., {}^{n_s}i_{\mathrm{q}}^{*}]'$ as follows:

$$\begin{aligned}&\bar{i}_{\mathrm{q}}^{*} = \tfrac{T^{*}}{k_T} Z_{sh} \\ &s.t. \textstyle\sum_{s=1}^{n_s} {}^{s}z_{sh} = 1\end{aligned} \tag{5.3}$$

where T^{*} is the reference torque. The imposition of the q$-$ axis currents via the sharing coefficients fully determine the torque produced by the machine. However, these current components also create a suspension force contribution ($\bar{F}_{\mathrm{q}}$) which can be evaluated via (5.1). More precisely, only the even columns of the $\mathbf{K}_{\mathrm{dq}}(\vartheta_{\mathrm{e}})$ matrix and the first two rows are needed to evaluate this force contribution. By building up this new sub-matrix $\mathbf{K}_{\mathrm{q}}(\vartheta_{\mathrm{e}})$, the force contributions $\bar{F}_{\mathrm{q}}$ are expressed as follows:

$$\bar{F}_{\mathrm{q}} = \begin{bmatrix} F_{x,\mathrm{q}} \\ F_{y,\mathrm{q}} \end{bmatrix} = \mathbf{K}_{\mathrm{q}}(\vartheta_{\mathrm{e}})\bar{i}_{\mathrm{q}} \tag{5.4}$$

The remaining degrees of freedom of the system, i.e. the d-axis currents, can be exploited for the production of the reference suspension force ($\bar{F}_r{}^*$). Indeed, the d$-$ axis current vector $\bar{i}_{\mathrm{d}}$ produces suspension force components which can be evaluated from (5.1):

$$\bar{F}_{\mathrm{d}} = \begin{bmatrix} F_{x,\mathrm{d}} \\ F_{y,\mathrm{d}} \end{bmatrix} = \mathbf{K}_{\mathrm{d}}(\vartheta_{\mathrm{e}})\bar{i}_{\mathrm{d}} \tag{5.5}$$

where $\mathbf{K}_{\mathrm{d}}(\vartheta_{\mathrm{e}})$ is the sub-matrix of $\mathbf{K}_{\mathrm{dq}}(\vartheta_{\mathrm{e}})$ built with its odd columns and the first two rows. In order to produce the desired force reference $\bar{F}_r{}^*$ equal to the sum of the d$-$ and q$-$ axis currents contributions ($\bar{F}_{\mathrm{d}}$ and $\bar{F}_{\mathrm{q}}$), the reference d-axis currents have to produce the force $\bar{F}_r{}^* - \bar{F}_{\mathrm{q}}$, therefore:

$$\bar{i}^*_{\mathrm{d}} = \mathbf{K}^+_{\mathrm{d}}(\vartheta_{\mathrm{e}})[\bar{F}_r{}^* - \bar{F}_{\mathrm{q}}] \tag{5.6}$$

where $\mathbf{K}^+_{\mathrm{d}}(\vartheta_{\mathrm{e}})$ is the Moore-Penrose inverse of the $3 \times n_s$ $\mathbf{K}_{\mathrm{d}}(\vartheta_{\mathrm{e}})$ matrix. It

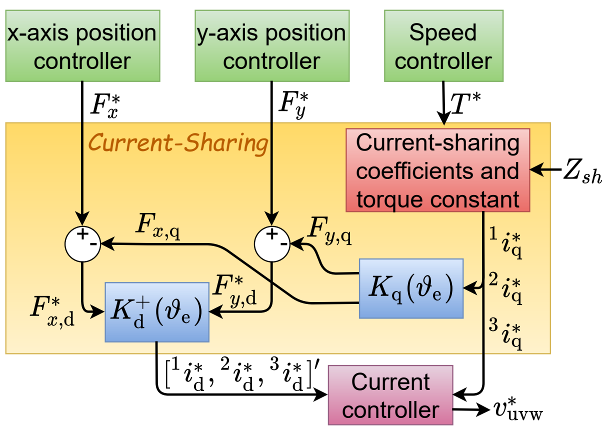

Figure 5.1: *Flow chart of the current-sharing technique.*

is worth underlining that the d-axis currents do not have any effect on the torque, being the reluctance torque null. Figure 5.1 summarises the proposed current-sharing control strategy for the triple three-phase permanent magnet machine considered in this study.

5.3.2 Sector open fault condition

Due to the modularity of the torque and force generation of this particular machine topology, it is possible to keep on fully controlling force and torque in current-sharing operations also when an entire sub-winding is opened. In fact, the control problem outlined in the previous sub-section can be easily solved by assuming a reduced number of three-phase subsystems. Indeed, while building the matrix of wrench coefficients $\mathbf{K}_{\mathrm{dq}}(\vartheta_{\mathrm{e}})$, the sub-matrix ${}^{s}\mathbf{K}_{\mathrm{dq}}(\vartheta_{\mathrm{e}})$ of the faulty module must not be considered, as mentioned in section 3.4.1.

In case of open fault of the first sector (but the same procedure can be extended to the other ones), the considered machine would feature two sharing coefficients ${}^{2}z_{sh}$ and ${}^{3}z_{sh}$, with ${}^{2}z_{sh} +^{3} z_{sh} = 1$ which determine the split of the torque among the sector 2 and 3 (i.e., ${}^{2}i_{\mathrm{q}}^{*}$ and ${}^{3}i_{\mathrm{q}}^{*}$) while the d-axis reference currents needed to produce the reference force would be:

$$\bar{i}_{\mathrm{d}}^{*} = \begin{bmatrix} {}^{2}i_{\mathrm{d}}^{*} \\ {}^{3}i_{\mathrm{d}}^{*} \end{bmatrix} = \begin{bmatrix} {}^{2}k_{x\mathrm{d}} & {}^{3}k_{x\mathrm{d}} \\ {}^{2}k_{y\mathrm{d}} & {}^{3}k_{y\mathrm{d}} \end{bmatrix}^{-1} \begin{bmatrix} F_{x,\mathrm{d}}^{*} \\ F_{y,\mathrm{d}}^{*} \end{bmatrix} \tag{5.7}$$

with:

$$\begin{bmatrix} F_{x,\mathrm{d}}^{*} \\ F_{y,\mathrm{d}}^{*} \end{bmatrix} = \begin{bmatrix} F_{x}^{*} \\ F_{y}^{*} \end{bmatrix} - \begin{bmatrix} {}^{2}k_{x\mathrm{q}} & {}^{3}k_{x\mathrm{q}} \\ {}^{2}k_{y\mathrm{q}} & {}^{3}k_{y\mathrm{q}} \end{bmatrix} \begin{bmatrix} {}^{2}i_{\mathrm{q}}^{*} \\ {}^{3}i_{\mathrm{q}}^{*} \end{bmatrix} \tag{5.8}$$

where all the wrench coefficients are still function of the rotor electrical position ϑ_{e}. It is worth noticing that for this particular case (i.e. 3 sectors) the pseudo-inverse of the matrix is not required because the system of equations is no more underdetermined. This control approach can be used to manage open faults of more than one sector, being aware that to continue the bearingless operation under current-sharing control the minimum number of healthy sector must be two.

5.4 Control system diagram and FEA validation

At first, this section gives an overview of the current-sharing control system architecture of the bearingless MS PMSM. Afterwards, a detailed FE based analysis is presented in order to verify if the proposed current-sharing technique is able to generate the desired radial force and torque.

5.4.1 Control system

A schematic of the bearingless control system with the current-sharing among the sectors is illustrated in Figure 5.2. The machine three-phase sub-windings

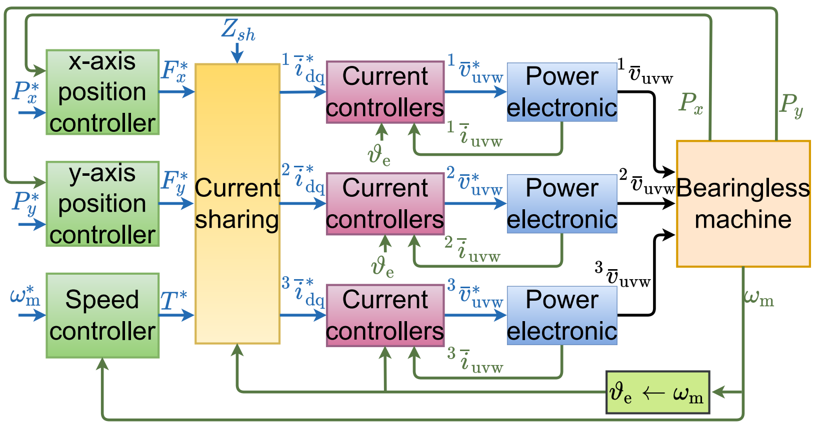

Figure 5.2: *Schematic diagram of the bearingless machine control system.*

are supplied by three independent three-phase inverters. The position controllers, i.e. two independent PID regulators and the speed loop PI controller, which are introduced in Appendix A, determine the reference wrench components from the measured radial shaft positions and angular speed errors. The reference currents are then calculated via the current-sharing logic detailed in Appendix A. The latter are then tracked via six conventional PI regulators, which together with the current loop are introduced in section 3.6.1.

5.4.2 Finite Element Analysis validation of the proposed current-sharing technique

The bearingless control of a MS PMSM requires the implementation of the control strategy summarised in (5.6) when including the current-sharing option on a real time control platform. In particular, the wrench coefficients matrices $\mathbf{K}^{+}_{\mathrm{dq}}(\vartheta_{\mathrm{e}})$, $\mathbf{K}_{\mathrm{q}}(\vartheta_{\mathrm{e}})$, and $\mathbf{K}^{+}_{\mathrm{d}}(\vartheta_{\mathrm{e}})$ can be calculated off-line once the full matrix $\mathbf{K}_{\mathrm{dq}}(\vartheta_{\mathrm{e}})$ has been characterised by FEA or experimental tests. Such matrices, function of the electrical position, can be then stored via Look Up Tables on the real time hardware in order to perform the bearingless current-sharing control. In fact, $\mathbf{K}_{\mathrm{dq}}(\vartheta_{\mathrm{e}})$ is converted from $\mathbf{K}_{\alpha\beta}(\vartheta_{\mathrm{e}})$ which is obtained from FEA; hence this section will focus on the validation of current-sharing operation.

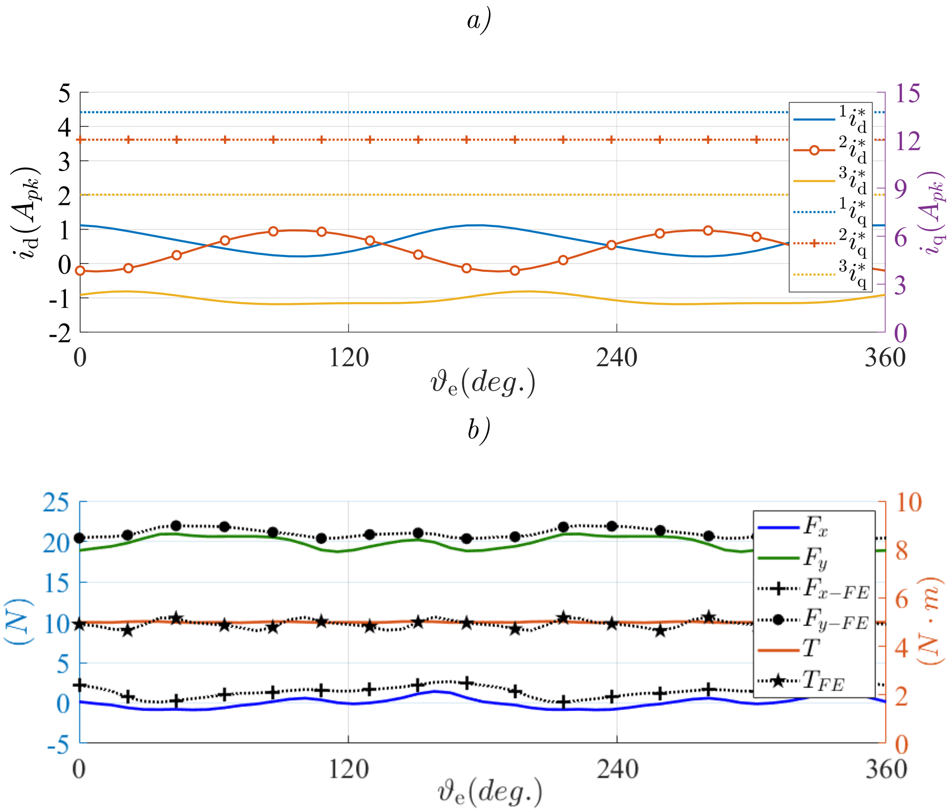

Figure 5.3: *Reference* $\mathrm{d}-\mathrm{q}$ *currents, expected and FE wrench components when generating the rated wrench* ($F^{*}_{x} = 0N$, $F^{*}_{y} = 20N$, $T^{*} = 5Nm$). *a) d-q axis current references computed from* $\mathbf{K}^{+}_{\mathrm{d}}(\vartheta_{\mathrm{e}})\bar{W}^{*}$ *considering only two harmonics in* $\mathbf{K}^{+}_{\mathrm{d}}(\vartheta_{\mathrm{e}})$. *b) The analytical result* $[F_x, F_y, T_x]$ *and the FEA result* $[F_{x-FE}, F_{y-FE}, T_{x-FE}]$.

Figure 5.3 a) and b) report the reference currents as well as the expected and FE wrench components when considering a non uniform current-sharing scenario ($Z_{sh} = [0.4\ 0.35\ 0.25]'$). The wrench reference is $\bar{W}^* = [0N,\ 20N,\ 5Nm]$, and the test is implemented in an electrical period. The non uniform current-sharing coefficient results in the non uniform q-axis currents, shown in Figure 5.3 a). The d axis current references are obtained from $\mathbf{K}_{\mathrm{d}}^{+}(\vartheta_{\mathrm{e}})\bar{W}^*$ considering only two harmonics in $\mathbf{K}_{\mathrm{d}}^{+}(\vartheta_{\mathrm{e}})$, which decreases the computational load and is also implemented in the control board in the experimental section. The d-q axis current references, shown in Figure 5.3 a), are injected to FEA software to obtain $[F_{x-FE},\ F_{y-FE},\ T_{x-FE}]$, shown in Figure 5.3 b). Meanwhile, $[F_x,\ F_y,\ T_x]$ is computed via $\mathbf{K}_{\mathrm{dq}}(\vartheta_{\mathrm{e}})\bar{i}^*_{\mathrm{dq}}$. The expected $[F_x,\ F_y,\ T_x]$ does not perfectly match the wrench reference because only two harmonics in $\mathbf{K}_{\mathrm{d}}^{+}(\vartheta_{\mathrm{e}})$ are considered. Furthermore, an error exists between the expected and FE wrench components. It is worth underlining that the wrench mismatch between expected and FE/real values, due to the assumption of negligible interaction among stator sectors, is compensated by the actions of the position and speed closed-loop controllers.

5.5 Experimental validation

The proposed current-sharing technique is validated on a 1.5kW-3000rpm prototype bearingless MS PMSM whose parameters are listed in Table 3.1. The system diagram is displayed in Figure 5.2, and each controller of the system is introduced in section 3.6.1 and Appendix A. The experimental hardware is already described in detail in section 3.6.2. In the next subsections, an extensive test campaign is reported to fully validate the proposed control strategy. In particular, three tests are implemented to verify the performance of the proposed bearingless current-sharing control technique in different healthy and faulty operating scenarios.

5.5.1 Current-sharing in healthy machine condition

In the first test, the speed controller is disabled and the angular shaft speed is controlled at 3000rpm by the load motor while the shaft radial position is regulated by the bearingless machine. The current-sharing coefficient is kept constant during the experiment to $Z_{sh} = [0.5\ 0.7\ \ -0.2]'$. The experimental results are shown in Figure 5.4.

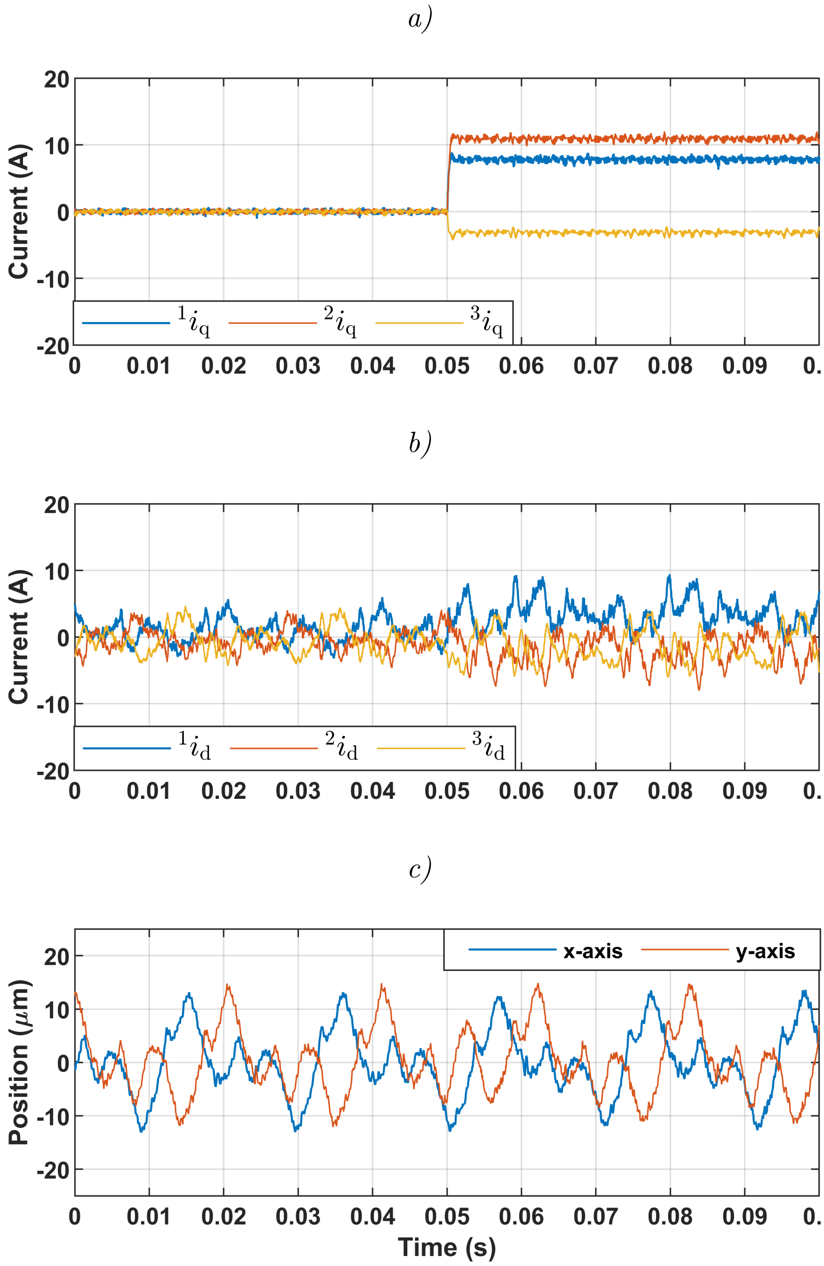

Figure 5.4: *Experimental results without the speed controller. a) q-axis currents of three sectors. b) d-axis currents of three sectors. c) Shaft x-y axes position.*

At 0.05s, the torque reference changes from 0 to $2Nm$, resulting in q-axis currents of three sectors increasing from 0 to 7.8A, 10.92A and -3.12A, respectively, as shown in Figure 5.4 a). As explained in section 5.3, the q-axis current of each sector is determined by the current-sharing coefficient and the torque reference. In the meantime, the d-axis currents increase to compensate for the radial force contribution generated by the q-axis currents, as shown in Figure 5.4 b). The shaft x-y axes position are displayed in Figure 5.4 c) showing a stable operation during the torque transient.

5.5.2 Current-sharing in the faulty machine condition

The second test, whose results are shown in Figure 5.5, verifies the performance of the current-sharing technique when an entire stator sector is in open fault. The speed is still set at 3000rpm by the load motor while the shaft x-y position is controlled by the BM. This test is constituted by four steps as clearly shown in Figure 5.5 a).

- Before 0.2s, the current-sharing is set to be uniform, with 5.2A q-axis currents in all the three sectors.
- Then, the q-axis currents of three sectors separately change to -6.24A, 9.36A, and 12.48A at 0.2s due to a request of current-sharing coefficients $Z_{sh} = [-0.4\ 0.6\ 0.8]'$.
- At 0.4s, the TPOC fault occurs in sector 1, dropping to zero the d-q axes currents of the first sector, as shown in Figure 5.5 a) and b), while the current-sharing coefficients update to $Z_{sh} = [0\ 0.2\ 0.8]'$ resulting in the decrease of the i_{q} current of the 2^{nd} sector.
- After 0.6s, the faulty sector recovers and goes back to its normal operation. Consequently, the $\mathrm{d} - \mathrm{q}$ axes currents increase to the same magnitude that they had between 0.2s and 0.4s.

Three small position oscillations can be appreciated from Figure 5.5 c) at 0.2s, 0.4s and 0.6s, respectively. These oscillations are caused by the sudden change

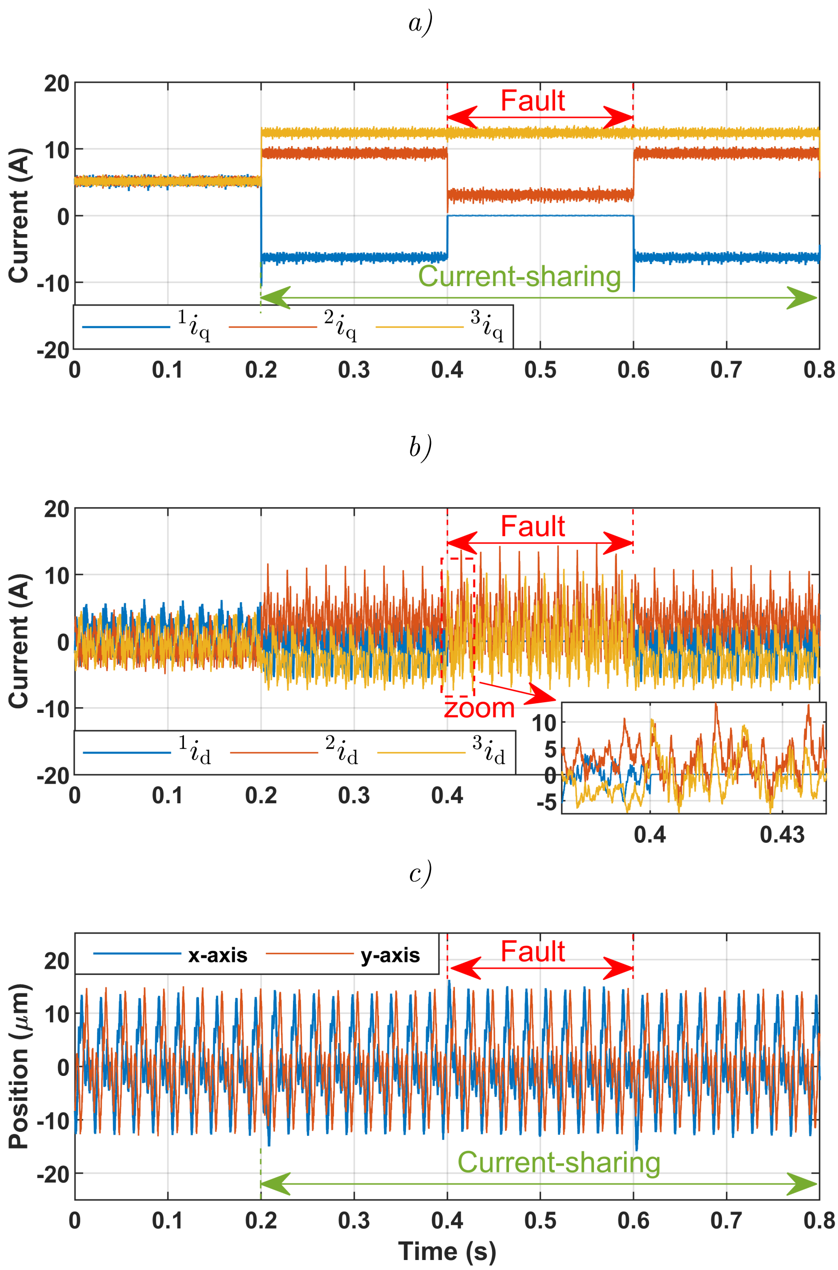

Figure 5.5: *Experimental results of the test without the speed controller under the three-phase open-circuit fault condition. a) q-axis currents of three sectors. b) d-axis currents of three sectors. c) Shaft x-y axes position.*

in the current-sharing coefficients and the open fault occurrence. However, the results clearly show that these fast current transients do not practically affect the performance of the bearingless operation.

5.5.3 Current-sharing in the speed and position transient

During the third test, both speed and radial positions are controlled by the bearingless drive in order to asses the system behaviour in both position and speed transient under simultaneous current-sharing and TPOC fault conditions. In particular, this test can be divided in five periods described in the following with reference to Figure 5.6 a-d) showing positions, speed, and $\mathrm{d}-\mathrm{q}$ axis currents, respectively.

- Before 0.1s, the drive is off.

- Then, at 0.1s, the drive is activated with the current-sharing coefficients equal to $Z_{sh} = [-0.4\ 0.6\ 0.8]'$. The shaft moves from its rest position to the airgap centre, as shown in Figure 5.6 a). The suspension force for levitating the rotor is totally generated by the d-axis currents being null the speed set point. Thus, three peaks occur in the d-axis currents at 0.1s, as shown in Figure 5.6 c).

- After the position transient, the machine accelerates from 0rpm to 3000rpm between 0.2s and 3.8s. During the speed transient the machine's output torque is $2Nm$. Correspondingly, the q-axis currents of the three sectors are -6.24A, 9.36A and 12.48A, respectively, and are defined by the torque reference and sharing coefficients.

- During the speed transient at 1.2s, an open fault occurs in the first sector, and the current-sharing coefficients are changed to $Z_{sh} = [0\ 0.6\ 0.4]'$ being null the contribution of the first sector.

- At 2.2s, the first module recovers from its faulty condition, and the current-sharing coefficients returns back to the previous healthy value, and consequentially also the currents.

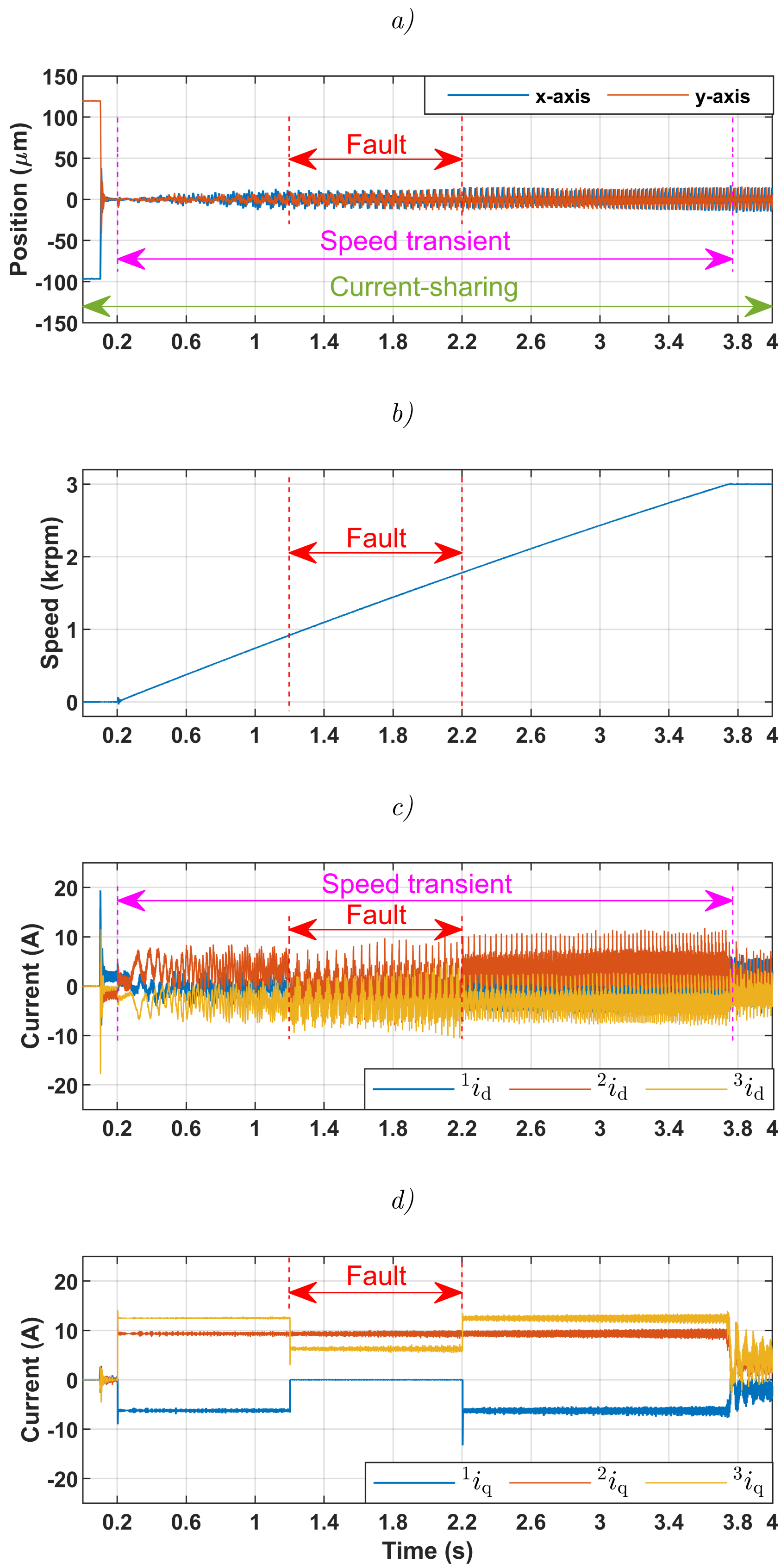

Figure 5.6: *Experimental results of the test with the speed controller. a) Shaft x-y axes position. b) Rotating speed. c) d-axis currents of three sectors. d) q-axis currents of three sectors.*

- At 3.8s, the speed transient ends, and the q-axis currents decrease following the torque reduction.

The results highlight the robustness of the proposed control strategy for the current-sharing operation of the bearingless drive also when a fault happens in a sector during the speed transient.

5.6 Conclusion

This chapter introduces a modular current-sharing control technique for bearingless MS PMSM and demonstrates its performance under healthy and one sector open phase faulty conditions. Firstly, the theoretical fundamentals of the proposed control strategy, allowing both bearingless and current-sharing operations in healthy and faulty conditions, have been outlined. Further FEAs replicating the real control scenario have also been carried out with the aim of assessing the current-sharing operation. The analysis also demonstrates the validity of the control hypothesis of negligible coupling among stator sectors. The proposed control strategy has been experimentally validated for a wide range of operating scenarios including the bearingless and current-sharing operation, in both healthy and faulty conditions as well as during speed transient. These outcomes represent a step forward with respect to the methods presented in section 5.1 and introduce novel elements to be applied in fault-tolerant drives for bearingless machines.

Chapter 6

Conclusion

6.1 Main contributions

This thesis firstly introduces the structure and the voltage equation of the modular bearingless machines. Then, it presents three contributions of the projects: fault-tolerant control, smart current limitation, and current-sharing, which are listed in the following.

Part I: firstly, a comprehensive description of the suspension force and torque generation principle is given, aided by a detailed FEA of the considered machine. This analysis aims to assess one of the hypotheses of the control technique, i.e. the linearity of the force-current relationship. Then, a control method for TPOC fault condition and a control strategy for SPOC fault in one or two sectors are proposed. The fault-tolerant control theory is verified by FEA simulation. The results show that the proposed fault-tolerant control algorithm can generate the desired suspension forces and torque. Furthermore, the FEA results highlight the importance of an accurate estimation of the force and torque coefficients to guarantee good performances during an open-circuit fault. The analysis also demonstrates the validity of the control hypothesis of negligible coupling among stator sectors in the generation of the overall wrench. Additionally, a fault detector is also designed in order to promptly recognise an open-circuit fault.

Part II: a smart current limitation technique that prioritises suspension force generation is presented, considering the health, TPOC, and SPOC faults conditions. The method allows the machine to deliver the maximum torque while the required suspension force is guaranteed to avoid the rotor touchdown.

Part III: the theoretical fundamentals of current-sharing operations in healthy and faulty conditions are outlined. The technique realises levitation operations and active power flowing among sectors, simultaneously. Further FEAs replicating the real control scenario is also carried out.

The work presented in the first and third chapter neglects the interactions between sectors, so the FEA is necessary to evaluate the performance when the algorithms are applied in the entire machine. The simulation results demonstrate that the neglected coupling among sectors does not strongly influence the generation of suspension force, and the suspension force error can be compensated by position controllers. The second part only contains the numeric algorithm. Therefore, the technique is only validated by numerical simulations. The results show that the technique can maintain the rotor levitation and therefore avoids a potentially destructive touchdown during the transient. Additionally, it has been shown how the proposed approach outperforms conservative current saturation techniques guaranteeing to always exploit the maximum available torque during transients as well as limiting torque distortion and position ripple. Due to the machine's modular design, these techniques can be applied to any modular machine if the coupling between stator sectors in the generation of the overall wrench is negligible.

The proposed control strategies are experimentally validated for a wide range of operating scenarios, including both healthy and faulty conditions, steady states and transients. These outcomes represent a step forward with respect to the methods presented in literature and introduce novel elements to be applied in bearingless machines.

6.2 Further improvements

The future works are listed in the following:

- The project proposes improved control strategies for the MS PMSM and verifies the algorithms in a partially levitating machine. Therefore, the first further work is to extend the machine to full levitation.

- The fault-tolerant technique only aims to implement the machine operating in open-circuit faults. The short-circuit fault control technique should be explored in the future.

- The smart current limitation technique assumes that the inverter voltage does not saturate. Thus, the issue of voltage saturation will be explored in the future.

- Future work would extend the smart current limitation technique to prioritise the torque production at the expense of the forces.

- The current-sharing technique does not consider the SPOC fault condition. Future work should develop the fault-tolerant control strategies for the SPOC fault.

- The suspension force control can decrease vibrations caused by unbalanced magnetic pulls, the unmatch of rotor mass centre and geometrical centre, and other natural forces. Hence, the control strategies can reduce the vibrations of machines installed with conventional mechanical bearings. For this case, the machine vibration model is needed.

- For large electrical devices, the mass of the rotor is very large. Control approaches can be investigated to use produced suspension forces to partially relieve bearings load.

Appendix A

Designs of controllers for the position, speed, and current loops

A.1 Position controller

Thanks to the decoupled x-, y- axes forces and torque control algorithm presented in section 3.3.1 and 3.4, the speed loop and the position loop controllers can be separately designed, decreasing the system's complexity. Hence, the shaft movement plant of the BM is decoupled in x- and y- axis, and its system diagram is shown in the blue block of Figure A.1. In the diagram, m is the

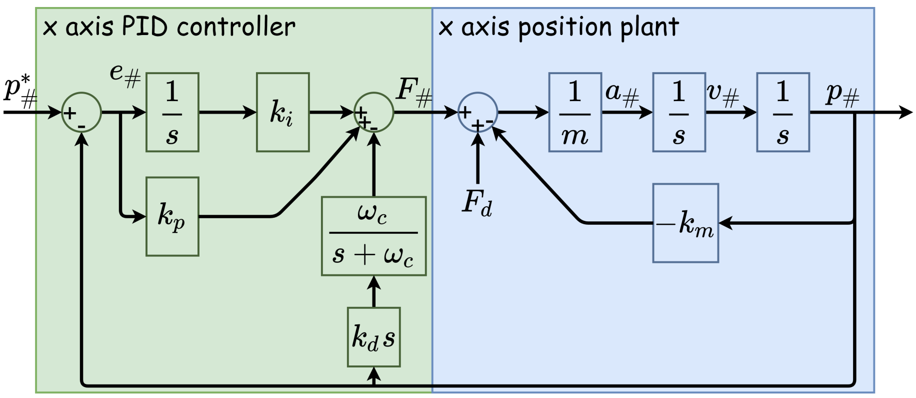

Figure A.1: *Shaft movement plant of the BM and system diagram of position controllers.*

mass of the rotor, $m = 2kg$. $p^*_\#$ and $p_\#$ represent the reference obtained from the upper computer and feedback measured from the machine, respectively. Meanwhile, the subscript # indicates the corresponding variable stands for x-axis or y-axis, $\# \in [x, y]$. $a_\#$, $v_\#$ and $F_\#$ represent the acceleration, the velocity, and the suspension force, respectively. Indeed, the velocity is not measured in the system, and then it is derived by differentiating the position. F_d is the force disturbance including unbalanced eccentric force, rotor gravity, and other distributions. Especially, the gravity of the rotor is considered in the y axis shaft position plant, but it does not influence the design of the controller so it is included in F_d. It is noted that the air friction is neglected in the plant, whereas the attraction between magnets and stator is considered and is represented by $-k_m$. Indeed, $k_m = 655$ $[kN/m]$, is the magnetic stiffness constant. Based on the system diagram, the transfer function of the plant is expressed in the following equation:

$$G_p(s) = \frac{1}{ms^2 - k_m}. \tag{A.1}$$

To control the position of the shaft, a PID controller with a low pass filter is designed for the position loop, as shown in the green block of Figure A.1. k_p, k_i, and k_d are the proportional, the integral, and the derivative gain, respectively. In the experiment, the position feedback contains a lot of noise which results in big numerical values of the differential solution, so the low pass filter is required. ω_c is the cut off frequency of the low pass filter. Since the position controller mainly rejects disturbances and keeps the shaft centred, the closed loop transfer function from $p^*_\#$ to $p_\#$ has been analysed. It is written as:

$$G(s) = \frac{1}{m} \frac{s^2 \cdot k_p + s \cdot (k_i + k_p\omega_c) + k_i\omega_c}{s^4 + s^3 \cdot \omega_c + s^2 \cdot \frac{(k_p - k_m + k_d\omega_c)}{m} + s \cdot \frac{(k_i - k_m\omega_c + k_p\omega_c)}{m} + \frac{k_i\omega_c}{m}}. \tag{A.2}$$

The roots of the denominator of (A.2) are close loop poles of the system shown in Figure A.1. Locations of poles determine the stability of the system.

Comparing the denominator of (A.2) with a reference polynomial expression, it can be seen that poles are placed at desired locations. In detail, the four poles are placed coincidentally at the pulsation ω_0 while the corresponding reference polynomial is:

$$(s+\omega_0)^4 = s^4 + s^3 \cdot 4\omega_0 + s^2 \cdot 6\omega_0^2 + s \cdot 4\omega_0^3 + \omega_0^4 \tag{A.3}$$

Equating the coefficients of the denominator of (A.2) with the coefficients of (A.3) the parameters of the system can be expressed in the following form.

$$\begin{cases} \omega_c = 4\omega_0 \\ \dfrac{k_p + k_d\omega_c - k_m}{m} = 6\omega_0^2 \\ \dfrac{k_i + k_p\omega_c - k_m\omega_c}{m} = 4\omega_0^3 \\ \dfrac{k_i\omega_c}{m} = \omega_0^4 \end{cases} \tag{A.4}$$

The solution of the above equation is a function of ω_0 and can be expressed in the follow.

$$\begin{cases} \omega_c = 4\omega_0 \\ k_i = \dfrac{\omega_0^4 m}{\omega_c} \\ k_p = \dfrac{4\omega_0^3 m - k_i + k_m\omega_c}{\omega_c} \\ k_d = \dfrac{6\omega_0^2 m - k_p + k_m}{\omega_c} \end{cases} \tag{A.5}$$

In the experimental test, ω_0 is set to 130Hz which is empirically chosen to ensure the robustness of the system. Indeed, due to the hardware limit, the switching frequency of IGBT is 10kHz. Consequently, the current close loop natural frequency is set to 1kHz. As mentioned at the start of sub-section 3.6.1 (assuming the current loop guarantees the feedback follow the reference with a minimal delay), the position close loop natural frequency should be much smaller than the one of the current loop.

A.2 Speed controller

The rotor rotary plant is displayed in the blue block of Figure A.2 and its state space is reported in (A.6)

$$\begin{bmatrix} \dot{\omega}_m \end{bmatrix} = \begin{bmatrix} -\frac{B}{J} \end{bmatrix} \omega_m + \begin{bmatrix} \frac{1}{J} \end{bmatrix} u \tag{A.6}$$

where ω_m is the rotating speed (rad/s). J and B are the moment of inertia and the friction factor, respectively. The input of the plant is torque. A conventional PI controller is installed to regulate the speed. k_p and k_i determine

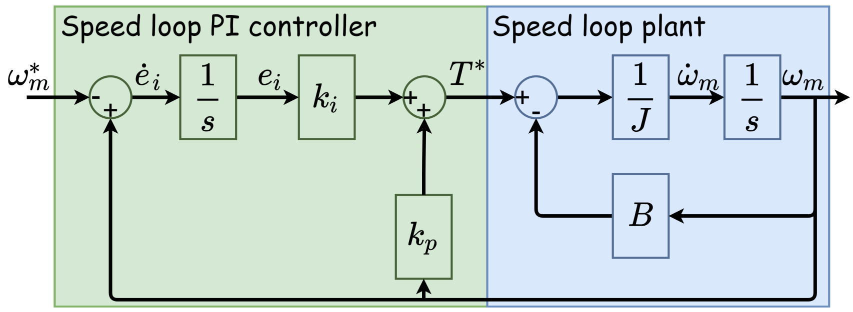

Figure A.2: *The rotor rotary plant and its control system diagram.*

locations of poles and they can be derived by the pole placement approach which is presented in [92] and obtained by the following steps:

- For the proposed system, at first the state space is extended so that the controller and the plant are involved, as expressed in (A.7)

$$\begin{bmatrix} \dot{e}_i \\ \dot{\omega}_m \end{bmatrix} = \begin{bmatrix} 0 & 1 \\ 0 & -\frac{B}{J} \end{bmatrix} \begin{bmatrix} e_i \\ \omega_m \end{bmatrix} + \begin{bmatrix} 0 \\ \frac{1}{J} \end{bmatrix} u \tag{A.7}$$

  where the coefficient matrix is defined as following variables:

$$\begin{aligned} A &= \begin{bmatrix} 0 & 1 \\ 0 & -\frac{B}{J} \end{bmatrix} \\ B &= \begin{bmatrix} 0 \\ \frac{1}{J} \end{bmatrix}. \end{aligned} \tag{A.8}$$

- The damping factor and natural frequency are set at 0.707 and $150 \cdot 2\pi\,(rad/s)$, respectively. Consequently, roots of the (A.9) is chosen as the poles of the close loop system, shown in the follow:

$$s^2 + 2\xi\omega_n + \omega_n^2 = 0 \tag{A.9}$$

where ξ is the damping factor and ω_n is the natural frequency. Additionally, roots $pole_1$ and $pole_2$ can be expressed by a matrix P as defined in the follow:

$$P = \begin{bmatrix} pole_1 \\ pole_2 \end{bmatrix}. \tag{A.10}$$

- Last, the gain k_p and k_i can be obtained by the Matlab command '$place(A, B, P)$'. The command can put the poles to the desired locations through appropriate values of k_p and k_i [92].

A.3 Current controller

Similar to the design of the speed loop, current loop uses the pole placement approach as well. The plant of current loop is reported in the blue block of Figure A.3, and the considered conventional PI controller is displayed in the green block. In the figure, the subscript $\varkappa \in [\mathrm{d}, \mathrm{q}]$. $i^*_\varkappa$ and $i_\varkappa$ are the reference and the feedback of the $\mathrm{d}-\mathrm{q}$ axis current, respectively. $v^*_\varkappa$ means the d-axis or q- axis voltage reference. $L_\varkappa$ stands for the d- or q- axis inductance. r_{ph} represents the resistance. The desired natural frequency and damping

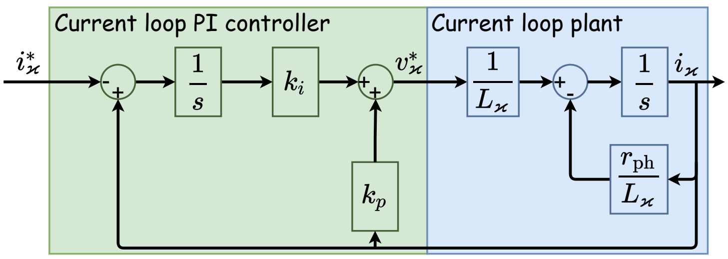

Figure A.3: *Plant of the current loop and its control system.*

factor are 1000Hz and 0.707, respectively. Redoing the procedure listed in section A.2, the integral and proportional gains of the current controller will be obtained.

Appendix B

List of Publications

1. Z. Wen, G. Valente, A. Formentini, L. Papini, C. Gerada and P. Zanchetta, "Open-Circuit Fault Control Techniques for Bearingless Multisector Permanent Magnet Synchronous Machines," in IEEE Transactions on Industry Applications, vol. 57, no. 3, pp. 2527-2536, May-June 2021, doi: 10.1109/TIA.2021.3060368. [93] [Chapter 3]

2. Z. Wen, G. Valente, A. Formentini, L. Papini, C. Gerada and P. Zanchetta, "A Novel Current Limitation Technique Exploiting the Maximum Capability of Power Electronic Inverter and Bearingless Machine," in IEEE Transactions on Industry Applications, vol. 57, no. 6, pp. 7012-7023, Nov.-Dec. 2021, doi: 10.1109/TIA.2021.3069149. [91] [Chapter 4]

3. Z. Wen et al., "Modular Power Sharing Control for Bearingless Multi-three Phase Permanent Magnet Synchronous Machine," in IEEE Transactions on Industrial Electronics, vol. 69, no. 7, pp. 6600-6610, July 2022, doi: 10.1109/TIE.2021.3097610. [94] [Chapter 5]

4. Z. Wen, G. Valente, A. Formentini, L. Papini, P. Zanchetta and C. Gerada, "Single-Phase Open-Circuit Fault Operation of Bearingless Multi-Sector PM Machines," 2019 IEEE International Electric Machines and Drives Conference (IEMDC), 2019, pp. 1087-1092,

   doi: 10.1109/IEMDC.2019.8785111. [95]

5. Z. Wen, G. Valente, A. Formentini, L. Papini, P. Zanchetta and C. Gerada, "Smart Current Limitation Technique for a Multiphase Bearingless Machine with Combined Winding System," 2019 IEEE Energy Conversion Congress and Exposition (ECCE), 2019, pp. 6099-6105, doi: 10.1109/ECCE.2019.8913291. [96]

6. Z. Wen, G. Valente, A. Formentini, L. Papini, P. Zanchetta and C. Gerada, "Mechanical Vibration Suppression on Multi-Sector PMSM with Optimal Active Vibration Control," The 10th International Conference on Power Electronics, Machines and Drives (PEMD 2020), 2020, pp. 314-319, doi: 10.1049/icp.2021.1123. [97]

Bibliography

[1] A. Chiba, T. Fukao, O. Ichikawa, M. Oshima, M. Takemoto, and D. G. Dorrell, *Magnetic bearings and bearingless drives.* Elsevier, 2005.

[2] J. Chen, J. Zhu, and E. L. Severson, "Review of bearingless motor technology for significant power applications," *IEEE Transactions on Industry Applications*, vol. 56, no. 2, pp. 1377–1388, 2020.

[3] K. Raggl, B. Warberger, T. Nussbaumer, S. Burger, and J. W. Kolar, "Robust angle-sensorless control of a pmsm bearingless pump," *IEEE Transactions on Industrial Electronics*, vol. 56, no. 6, pp. 2076–2085, June 2009.

[4] T. Zhang, X. Liu, L. Mo, X. Ye, W. Ni, W. Ding, J. Huang, and X. Wang, "Modeling and analysis of hybrid permanent magnet type bearingless motor," *IEEE Transactions on Magnetics*, vol. 54, no. 3, pp. 1–4, March 2018.

[5] E. Severson, S. Gandikota, and N. Mohan, "Practical implementation of dual-purpose no-voltage drives for bearingless motors," *IEEE Transactions on Industry Applications.*

[6] X. Sun, Z. Jin, Y. Cai, Z. Yang, and L. Chen, "Grey wolf optimization algorithm based state feedback control for a bearingless permanent magnet synchronous machine," *IEEE Transactions on Power Electronics*, vol. 35, no. 12, pp. 13 631–13 640, Dec 2020.

[7] Z. Liu, A. Chiba, Y. Irino, and Y. Nakazawa, "Optimum pole number combination of a buried permanent magnet bearingless motor and test results at an output of 60 kw with a speed of 37000 r/min," *IEEE Open Journal of Industry Applications*, vol. 1, pp. 33–41, Feb. 2020.

[8] Y. Okada, N. Yamashiro, K. Ohmori, T. Masuzawa, T. Yamane, Y. Konishi, and S. Ueno, "Mixed flow artificial heart pump with axial self-bearing motor," *IEEE/ASME Transactions on Mechatronics*, vol. 10, no. 6, pp. 658–665, Dec 2005.

[9] P. K. Hermann, "A radial active magnetic bearing," *London Patent, No. 1478868*, no. 1, p. 478, 1973.

[10] A. Chiba, M. A. Rahman, and T. Fukao, "Radial force in a bearingless reluctance motor," *IEEE Transactions on Magnetics*, vol. 27, no. 2, pp. 786–790, March 1991.

[11] A. O. Salazar and R. M. Stephan, "A bearingless method for induction machines," *IEEE Transactions on Magnetics*, vol. 29, no. 6, pp. 2965–2967, Nov 1993.

[12] G. Valente, L. Papini, A. Formentini, C. Gerada, and P. Zanchetta, "Radial force control of multi-sector permanent magnet machines," in *2016 XXII International Conference on Electrical Machines (ICEM)*, Sept 2016, pp. 2595–2601.

[13] ——, "Radial force control of multi-sector permanent magnet machines considering radial rotor displacement," in *2017 IEEE Workshop on Electrical Machines Design, Control and Diagnosis (WEMDCD)*, April 2017, pp. 140–145.

[14] G. Valente, A. Formentini, L. Papini, C. Gerada, and P. Zanchetta, "Performance improvement of bearingless multisector pmsm with optimal robust position control," *IEEE Transactions on Power Electronics*, vol. 34, no. 4, pp. 3575–3585, April 2019.

[15] G. Valente, L. Papini, A. Formentini, C. Gerada, and P. Zanchetta, "Radial force control of multisector permanent-magnet machines for vibration suppression," *IEEE Transactions on Industrial Electronics*, vol. 65, no. 7, pp. 5395–5405, July 2018.

[16] C. Lin, S. Wang, M. Moallem, B. Fahimi, and C. Tschida, "Analysis of vibration in permanent magnet synchronous machines due to variable speed drives," *IEEE Trans. on Energy Conv.*, vol. 32, no. 2, pp. 582–590, June 2017.

[17] J. L. Besnerais, "Vibroacoustic analysis of radial and tangential air-gap magnetic forces in permanent magnet synchronous machines," *IEEE Transactions on Magnetics*, vol. 51, no. 6, pp. 1–9, June 2015.

[18] M. Valavi, A. Nysveen, R. Nilssen, R. D. Lorenz, and T. Rølvåg, "Influence of pole and slot combinations on magnetic forces and vibration in low-speed pm wind generators," *IEEE Transactions on Magnetics*, vol. 50, no. 5, pp. 1–11, May 2014.

[19] H. Sugimoto and A. Chiba, "Parameter identification of current–force factor and torque constant in single-drive bearingless motors with back emf," *IEEE Transactions on Industry Applications*, vol. 55, no. 5, pp. 4754–4761, Sept.-Oct. 2019.

[20] H. Mitterhofer, W. Gruber, and W. Amrhein, "On the high speed capacity of bearingless drives," *IEEE Transactions on Industrial Electronics*, vol. 61, no. 6, pp. 3119–3126, 2014.

[21] T. Reichert, T. Nussbaumer, and J. W. Kolar, "Investigation of exterior rotor bearingless motor topologies for high-quality mixing applications," *IEEE Transactions on Industry Applications*, vol. 48, no. 6, pp. 2206–2216, Nov 2012.

[22] M. Ooshima, S. Kobayashi, and H. Tanaka, "Magnetic suspension performance of a bearingless motor/generator for flywheel energy storage systems," in *IEEE PES General Meeting*, July 2010, pp. 1–4.

[23] S. Yuxin, L. Xianxing, W. Weiran, and X. Peifeng, "Design and finite element analysis of high speed motorized spindle system based on bearingless induction motor," in *2010 International Conference on Mechanic Automation and Control Engineering*, June 2010, pp. 5483–5486.

[24] X. Sun, L. Chen, and Z. Yang, "Overview of bearingless permanent-magnet synchronous motors," *IEEE Transactions on Industrial Electronics*, vol. 60, no. 12, pp. 5528–5538, Dec 2013.

[25] H. Jia, J. Wang, M. Cheng, W. Hua, and S. Fei, "Mathematical model of radial suspending force for a new stator-permanent magnet bearingless machine," *IEEE Transactions on Magnetics*, vol. 51, no. 11, pp. 1–4, Nov 2015.

[26] F. Barrero and M. J. Duran, "Recent advances in the design, modeling, and control of multiphase machines—part i," *IEEE Transactions on Industrial Electronics*, vol. 63, no. 1, pp. 449–458, 2016.

[27] S. Kobayashi, M. Ooshima, and M. N. Uddin, "A radial position control method of bearingless motor based on d - q -axis current control," *IEEE Transactions on Industry Applications*, vol. 49, no. 4, pp. 1827–1835, 2013.

[28] G. Valente, A. Formentini, L. Papini, P. Zanchetta, and C. Gerada, "Position control study of a bearingless multi-sector permanent magnet machine," in *IECON 2017 - 43rd Annual Conference of the IEEE Industrial Electronics Society*, 2017, pp. 8808–8813.

[29] M. Ooshima, A. Kobayashi, and T. Narita, "Stabilized suspension control strategy at failure of a motor section in a d-q axis current control bearingless motor," in *2015 IEEE Industry Applications Society Annual Meeting*, 2015, pp. 1–7.

[30] G. Valente, L. Papini, A. Formentini, C. Gerada, and P. Zanchetta, "Open-circuit fault tolerant study of bearingless multi-sector permanent magnet machines," in *2018 International Power Electronics Conference (IPEC-Niigata 2018 -ECCE Asia)*, 2018, pp. 4034–4041.

[31] M. J. Duran, I. González-Prieto, A. González-Prieto, and F. Barrero, "Multiphase energy conversion systems connected to microgrids with unequal power-sharing capability," *IEEE Transactions on Energy Conversion*, vol. 32, no. 4, pp. 1386–1395, 2017.

[32] I. Zoric, M. Jones, and E. Levi, "Arbitrary power sharing among three-phase winding sets of multiphase machines," *IEEE Transactions on Industrial Electronics*, vol. 65, no. 2, pp. 1128–1139, 2018.

[33] G. Sala, M. Mengoni, G. Rizzoli, L. Zarri, and A. Tani, "Decoupled d–q axes current-sharing control of multi-three-phase induction machines,"

IEEE Transactions on Industrial Electronics, vol. 67, no. 9, pp. 7124–7134, 2020.

[34] P. K. Hermann, "A radial active magnetic bearing having a rotating drive," *London Patent 1 500 809*, February 1974.

[35] R. Bosch, "Development of a bearingless electric motor," *ICEM*, p. 373–375, 1988.

[36] A. Chiba and T. Fukao, "Electric rotating machinery with radial position control windings and its rotor radial position controller," *Japan Patent No. 2835522*, 1988.

[37] A. Chiba, T. Deido, T. Fukao, and M. A. Rahman, "An analysis of bearingless ac motors," *IEEE Transactions on Energy Conversion*, vol. 9, no. 1, pp. 61–68, Mar 1994.

[38] T. Higuchi, H. Kawakatsu, and T. Iwasawa, "A study on magnetic suspension of switched reluctance motor," 1989.

[39] K. Shimada, M. Takemoto, A. Chiba, and T. Fukao, "Radial forces in switched reluctance type bearingless motors," 1997.

[40] R. Schob, "Principle and application of a bearingless slice motor," in *5th International Symposium on Magnetic Bearings*, 1996.

[41] T. Takenaga, "A principle and a design of a consequent-pole bearingless motor," *Proc.of Int.sym.magnetic Bearings*, 2002.

[42] R. Oishi, S. Horima, H. Sugimoto, and A. Chiba, "A novel parallel motor winding structure for bearingless motors," *IEEE Transactions on Magnetics*, vol. 49, no. 5, pp. 2287–2290, 2013.

[43] E. L. Severson, R. Nilssen, T. Undeland, and N. Mohan, "Design of dual purpose no-voltage combined windings for bearingless motors," *IEEE Transactions on Industry Applications*, vol. 53, no. 5, pp. 4368–4379, 2017.

[44] W. K. S. Khoo, K. Kalita, and S. D. Garvey, "Practical implementation of the bridge configured winding for producing controllable transverse forces in electrical machines," *IEEE Transactions on Magnetics*, vol. 47, no. 6, pp. 1712–1718, 2011.

[45] W. Khoo, "Bridge configured winding for polyphase self-bearing machines," *IEEE Transactions on Magnetics*, vol. 41, no. 4, pp. 1289–1295, 2005.

[46] F. Ahmed, M. D. Choudhury, G. Kumar, and K. Kalita, "Modeling and analysis of bearingless switched reluctance motor equipped with specialized stator winding," in *2016 IEEE International Conference on Power Electronics, Drives and Energy Systems (PEDES)*, 2016, pp. 1–6.

[47] J. Huang, B. Li, H. Jiang, and M. Kang, "Analysis and control of multiphase permanent-magnet bearingless motor with a single set of half-coiled winding," *IEEE Transactions on Industrial Electronics*, vol. 61, no. 7, pp. 3137–3145, July 2014.

[48] M. Kang, J. Huang, J.-q. Yang, and H.-b. Jiang, "Analysis and experiment of a 6-phase bearingless induction motor," in *2008 International Conference on Electrical Machines and Systems*, 2008, pp. 990–994.

[49] B. Li, J. Huang, H. Liu, and Z. Hou, "Analysis and control of seven-phase permanent-magnet bearingless motor with single set of half-coiled winding," in *2014 IEEE 23rd International Symposium on Industrial Electronics (ISIE)*, June 2014, pp. 2080–2086.

[50] X. L. Wang, Q. C. Zhong, Z. Q. Deng, and S. Z. Yue, "Current-controlled multiphase slice permanent magnetic bearingless motors with open-circuited phases: Fault-tolerant controllability and its verification," *IEEE Transactions on Industrial Electronics*, vol. 59, no. 5, pp. 2059–2072, May 2012.

[51] M. Ooshima, T. Karasawa, and M. N. Uddin, "Stabilized control strategy under loaded conditions in a bearingless motor based on d-q axis current control," in *2013 IEEE Industry Applications Society Annual Meeting*, 2013, pp. 1–7.

[52] H. Mahmoud, G. Valente, M. Degano, M. D. Nardo, C. Gerada, and B. James, "Multi-sector windings for bearing relief e-machine: Saturation and cross coupling effects," in *2020 International Conference on Electrical Machines (ICEM)*, vol. 1, 2020, pp. 246–252.

[53] G. Sala, G. Valente, M. Di Nardo, M. Degano, P. Zanchetta, and C. Gerada, "Power-sharing control in bearingless multi-sector and multi-three-phase permanent magnet machines," *IEEE Transactions on Industrial Electronics*, pp. 1–1, 2020.

[54] X. Cao, H. Yang, L. Zhang, and Z. Deng, "Compensation strategy of levitation forces for single-winding bearingless switched reluctance motor with one winding total short circuited," *IEEE Transactions on Industrial Electronics*, vol. 63, no. 9, pp. 5534–5546, 2016.

[55] T. Sekine, K. Hijikata, and Y. Tanaka, "Investigation of torque and suspension force characteristic in a reluctance type bearingless vernier motor," in *2017 IEEE International Electric Machines and Drives Conference (IEMDC)*, 2017, pp. 1–6.

[56] L. Chen and W. Hofmann, "Analysis of radial forces based on rotor eccentricity of bearingless switched reluctance motors," in *The XIX International Conference on Electrical Machines - ICEM 2010*, 2010, pp. 1–6.

[57] H. Wang, J. Bao, B. Xue, and J. Liu, "Control of suspending force in novel permanent-magnet-biased bearingless switched reluctance motor," *IEEE Transactions on Industrial Electronics*, vol. 62, no. 7, pp. 4298–4306, 2015.

[58] W. Gruber, M. Rothböck, and R. T. Schöb, “Design of a novel homopolar bearingless slice motor with reluctance rotor,” *IEEE Transactions on Industry Applications*, vol. 51, no. 2, pp. 1456–1464, 2015.

[59] T. Baumgartner, R. M. Burkart, and J. W. Kolar, “Analysis and design of a 300-w 500000-r/min slotless self-bearing permanent-magnet motor,” *IEEE Transactions on Industrial Electronics*, vol. 61, no. 8, pp. 4326–4336, Aug 2014.

[60] H. Wang, J. Liu, J. Bao, and B. Xue, “A novel bearingless switched reluctance motor with a biased permanent magnet,” *IEEE Transactions on Industrial Electronics*, vol. 61, no. 12, pp. 6947–6955, 2014.

[61] A. Sinervo and A. Arkkio, “Rotor radial position control and its effect on the total efficiency of a bearingless induction motor with a cage rotor,” *IEEE Transactions on Magnetics*, vol. 50, no. 4, pp. 1–9, 2014.

[62] A. Chiba, R. Furuichi, Y. Aikawa, K. Shimada, Y. Takamoto, and T. Fukao, “Stable operation of induction-type bearingless motors under loaded conditions,” *IEEE Transactions on Industry Applications*, vol. 33, no. 4, pp. 919–924, 1997.

[63] A. Chiba and J. Asama, “Influence of rotor skew in induction type bearingless motor,” *IEEE Transactions on Magnetics*, vol. 48, pp. 4646–4649, 11 2012.

[64] T. Suzuki, A. Chiba, M. Azizur Rahman, and T. Fukao, “An airgap flux oriented vector controller for stable magnetic suspension during high torque acceleration in bearingless induction motors,” in *Conference Record of the 1999 IEEE Industry Applications Conference. Thirty-Forth IAS Annual Meeting (Cat. No.99CH36370)*, vol. 3, 1999, pp. 1543–1550 vol.3.

[65] R. De Doncker, F. Profumo, M. Pastorelli, and P. Ferraris, “Comparison of universal field oriented (ufo) controllers in different reference frames,” *IEEE Transactions on Power Electronics*, vol. 10, no. 2, pp. 205–213, 1995.

[66] C. J. O’Rourke, M. M. Qasim, M. R. Overlin, and J. L. Kirtley, “A geometric interpretation of reference frames and transformations: dq0, clarke, and park,” *IEEE Transactions on Energy Conversion*, vol. 34, no. 4, pp. 2070–2083, 2019.

[67] J. W. Bennett, G. J. Atkinson, B. C. Mecrow, and D. J. Atkinson, “Fault-tolerant design considerations and control strategies for aerospace drives,” *IEEE Transactions on Industrial Electronics*, vol. 59, no. 5, pp. 2049–2058, 2012.

[68] I. Subotic, O. Dordevic, J. B. Gomm, and E. Levi, “Active and reactive power sharing between three-phase winding sets of a multiphase induction machine,” *IEEE Transactions on Energy Conversion*, vol. 34, no. 3, pp. 1401–1410, 2019.

[69] A. Galassini, A. Costabeber, M. Degano, C. Gerada, A. Tessarolo, and R. Menis, "Enhanced power sharing transient with droop controllers for multithree-phase synchronous electrical machines," *IEEE Transactions on Industrial Electronics*, vol. 66, no. 7, pp. 5600–5610, 2019.

[70] Z. Q. Zhu, M. L. M. Jamil, and L. J. Wu, "Influence of slot and pole number combinations on unbalanced magnetic force in pm machines with diametrically asymmetric windings," *IEEE Transactions on Industry Applications*, vol. 49, no. 1, pp. 19–30, Jan 2013.

[71] Z. Q. Zhu, Z. P. Xia, L. J. Wu, and G. W. Jewell, "Analytical modeling and finite-element computation of radial vibration force in fractional-slot permanent-magnet brushless machines," *IEEE Transactions on Industry Applications*, vol. 46, no. 5, pp. 1908–1918, Sept 2010.

[72] Z. Zhu, D. Howe, and C. Chan, "Improved analytical model for predicting the magnetic field distribution in brushless permanent-magnet machines," *IEEE Transactions on Magnetics*, vol. 38, no. 1, pp. 229–238, 2002.

[73] Z. Zhu and D. Howe, "Instantaneous magnetic field distribution in brushless permanent magnet dc motors. iii. effect of stator slotting," *IEEE Transactions on Magnetics*, vol. 29, no. 1, pp. 143–151, 1993.

[74] Z. Q. Zhu and D. Howe, "Instantaneous magnetic field distribution in brushless permanent magnet dc motors. ii. armature-reaction field," *IEEE Transactions on Magnetics*, vol. 29, no. 1, pp. 136–142, Jan 1993.

[75] S. S. Kuruppu and N. A. Kulatunga, "D-q current signature-based faulted phase localization for sm-pmac machine drives," *IEEE Transactions on Industrial Electronics*, vol. 62, no. 1, pp. 113–121, 2015.

[76] O. Wallmark, L. Harnefors, and O. Carlson, "Control algorithms for a fault-tolerant pmsm drive," *IEEE Transactions on Industrial Electronics*, vol. 54, no. 4, pp. 1973–1980, 2007.

[77] F. Meinguet, E. Semail, and J. Gyselinck, "An on-line method for stator fault detection in multi-phase pmsm drives," in *2010 IEEE Vehicle Power and Propulsion Conference*, 2010, pp. 1–6.

[78] A. Khlaief, M. Boussak, and M. Gossa, "Open phase faults detection in pmsm drives based on current signature analysis," in *The XIX International Conference on Electrical Machines - ICEM 2010*, 2010, pp. 1–6.

[79] R. Ribeiro, C. Jacobina, E. da Silva, and A. Lima, "Fault detection in voltage-fed pwm motor drive systems," in *2000 IEEE 31st Annual Power Electronics Specialists Conference. Conference Proceedings (Cat. No.00CH37018)*, vol. 1, 2000, pp. 242–247 vol.1.

[80] L. Liu and D. Cartes, "On-line identification and robust fault diagnosis for nonlinear pmsm drives," in *Proceedings of the 2005, American Control Conference, 2005.*, 2005, pp. 2023–2027 vol. 3.

[81] C. J. Gajanayake, B. Bhangu, S. Nadarajan, and G. Jayasinghe, "Fault tolerant control method to improve the torque and speed response in pmsm drive with winding faults," in *2011 IEEE Ninth International Conference on Power Electronics and Drive Systems*, 2011, pp. 956–961.

[82] S. Bolognani, M. Zigliotto, and M. Zordan, "Experimental fault-tolerant control of a pmsm drive," in *IECON '98. Proceedings of the 24th Annual Conference of the IEEE Industrial Electronics Society (Cat. No.98CH36200)*, vol. 1, 1998, pp. 492–497 vol.1.

[83] S. Bolognani, M. Zordan, and M. Zigliotto, "Experimental fault-tolerant control of a pmsm drive," *IEEE Transactions on Industrial Electronics*, vol. 47, no. 5, pp. 1134–1141, 2000.

[84] G. Valente, "Radial force control of bearingless multi-sector permanent magnet machines [http://eprints.nottingham.ac.uk/id/eprint/52086] / giorgio valente." 2018.

[85] S. Serri, A. Tani, and G. Serra, "Analytical model of radial forces considering mutual effects between torque and levitation current space vectors in 5-phase pm bearingless motors," in *IECON 2013 - 39th Annual Conference of the IEEE Industrial Electronics Society*, Nov 2013, pp. 5142–5147.

[86] R. Peuget, S. Courtine, and J. . Rognon, "Fault detection and isolation on a pwm inverter by knowledge-based model," *IEEE Transactions on Industry Applications*, vol. 34, no. 6, pp. 1318–1326, Nov 1998.

[87] O. Poncelas, J. A. Rosero, J. Cusido, J. A. Ortega, and L. Romeral, "Motor fault detection using a rogowski sensor without an integrator," *IEEE Transactions on Industrial Electronics*, vol. 56, no. 10, pp. 4062–4070, Oct 2009.

[88] S. A. Arogeti, D. Wang, and C. B. Low, "Mode identification of hybrid systems in the presence of fault," *IEEE Transactions on Industrial Electronics*, vol. 57, no. 4, pp. 1452–1467, April 2010.

[89] S. Dwari and L. Parsa, "Fault-tolerant control of five-phase permanent-magnet motors with trapezoidal back emf," *IEEE Transactions on Industrial Electronics*, vol. 58, no. 2, pp. 476–485, Feb 2011.

[90] A. Galassini, G. L. Calzo, A. Formentini, C. Gerada, P. Zanchetta, and A. Costabeber, "ucube: Control platform for power electronics," in *2017 IEEE Workshop on Electrical Machines Design, Control and Diagnosis (WEMDCD)*, April 2017, pp. 216–221.

[91] Z. Wen, G. Valente, A. Formentini, L. Papini, C. Gerada, and P. Zanchetta, "A novel current limitation technique exploiting the maximum capability of power electronic inverter and bearingless machine," *IEEE Transactions on Industry Applications*, pp. 1–1, 2021.

[92] G. F. Franklin, J. D. Powell, and A. Emami-Naeini, *Feedback control of dynamic systems.* Pearson London, 2015.

[93] Z. Wen, G. Valente, A. Formentini, L. Papini, C. Gerada, and P. Zanchetta, "Open-circuit fault control techniques for bearingless multisector permanent magnet synchronous machines," *IEEE Transactions on Industry Applications*, vol. 57, no. 3, pp. 2527–2536, 2021.

[94] Z. Wen, M. Di Nardo, G. Sala, G. Valente, A. Marfoli, M. Degano, P. Zanchetta, and C. Gerada, "Modular power sharing control for bearingless multi-three phase permanent magnet synchronous machine," *IEEE Transactions on Industrial Electronics*, pp. 1–1, 2021.

[95] Z. Wen, G. Valente, A. Formentini, L. Papini, P. Zanchetta, and C. Gerada, "Single-phase open-circuit fault operation of bearingless multi-sector pm machines," in *2019 IEEE International Electric Machines Drives Conference (IEMDC)*, 2019, pp. 1087–1092.

[96] Z. Wen, G. Valente, A. Formentini, L. Papini, P. Zanchetta, and C. Gerada, "Smart current limitation technique for a multiphase bearingless machine with combined winding system," in *2019 IEEE Energy Conversion Congress and Exposition (ECCE)*, 2019, pp. 6099–6105.

[97] ——, "Mechanical vibration suppression on multi-sector pmsm with optimal active vibration control," in *The 10th International Conference on Power Electronics, Machines and Drives (PEMD 2020)*, vol. 2020, 2020, pp. 314–319.